TECHNISCHE UNIVERSITÄT WIEN
Vienna | Austria

DISSERTATION

Ply-Level Modeling Based on Shell Elements for Predicting Static and Cyclic Delamination

carried out for the purpose of obtaining the degree of Doctor technicae (Dr.techn.),

submitted at TU Wien, Faculty of Mechanical and Industrial Engineering, by

Khairul Anam, ST., MSc.

Mat.Nr.: 11933257

Perum. Bumi Mondoroko Raya BA 62, Singosari, Malang 65153, Indonesia

under the supervision of

Associate Prof. Dipl.-Ing. Dr.techn. Heinz Pettermann

Associate Prof. Dipl.-Ing. Dr.techn. Melanie Todt

Institute of Lightweight Design and Structural Biomechanics, E317

reviewed by

Univ.-Prof. Dipl.-Ing. Dr.techn. Clara Schuecker
Montanuniversität Leoben
Otto Glöckel-Straße 2/II
8700 Leoben, Austria

Prof. Dr. Chiara Bisagni
Politecnico di Milano
Via La Masa 34
20156 Milano, Italy

Affidavit

I declare in lieu of oath, that I wrote this thesis and performed the associated research myself, using only literature cited in this volume. If text passages from sources are used literally, they are marked as such.

I confirm that this work is original and has not been submitted elsewhere for any examination, nor is it currently under consideration for a thesis elsewhere.

I acknowledge that the submitted work will be checked electronically-technically using suitable and state-of-the-art means (plagiarism detection software). On the one hand, this ensures that the submitted work was prepared according to the high-quality standards within the applicable rules to ensure good scientific practice "Code of Conduct" at the TU Wien. On the other hand, a comparison with other student theses avoids violations of my personal copyright.

Vienna, _____

Khairul Anam

Abstract

Lightweight structures such as laminated composite are widely used for various fields due to their exceptional mechanical characteristics such as high stiffness to weight and strength to weight ratios. These materials also exhibit good environmental sustainability, and excellent fatigue resistance, and are easy to form during manufacturing. However, these materials possess complex damage mechanisms such as matrix cracking, fiber breakage, plasticity-like effects, and delamination because they have an anisotropic behavior due to fiber reinforced plies and the stacking of the laminates. This damage is potentially dangerous because it can significantly reduce the load-carrying capacity, which can lead to failure. Delamination is one of the most dominant defects that arise in laminated composites. Delamination occurs internally in laminated composites so that damage is barely visible to the naked eye on the composite surface and, consequently, is difficult to detect during service.

The aim of this dissertation is to investigate the performance of the ply-level based modeling strategies for predicting delamination behavior in laminated composites under various loading scenarios and simulation schemes, by means of advanced methods within the framework of the finite element method. A variety of loading scenarios that frequently occur in engineering applications will be applied to laminated composite, resulting in delamination. The loading scenarios include pure and mixed mode loading conditions, low velocity impact, compression after impact, and fatigue after impact.

A ply-level based modeling strategy for predicting the delamination behavior of laminated composites under pure and mixed mode loading conditions is proposed within the framework of the Finite Element Method. Each ply and each interface of the laminate is explicitly modeled, with the plies represented by various element types such as conventional shell, continuum shell, and continuum elements, and the interfaces are discretized using cohe-

sive zone elements. The comparison between all proposed models is examined in terms of delamination onset and growth including load-displacement curves, delamination area, computation time, and mode mixity. The results show that all ply-level based modeling strategies exhibit very good agreement with the analytical results. Moreover, ply-level approach based on shell elements in combination with finite thickness cohesive zone elements offers a numerically efficient simulation tool to predict delamination in laminates.

Moreover, a study of transverse shear behavior of homogeneous plane strain isotropic beam is done for different ply-level based modeling strategies. From numerical predictions, it can be concluded that the ply-level approach based on shell elements in combination with a finite thickness cohesive zone element model provides a very good agreement to the analytical solutions and two dimensional plane strain model in terms of deflection, transverse shear stress, and normal bending stress. The shear deformation has already been considered in continuum models. Consequently, the reduction of out-of-plane stiffness of cohesive zone elements will lead to a physically not correct model because they are more compliant than the reference results and seem to have double shear deformation. Finally, the modification of $G_{xz} = G_{yz}$ by implementing the orthotropic elasticity of continuum models can be used to mimic the reference solutions.

Low velocity impact can significantly reduce the structural integrity of the laminated composites, and it can be considerably worse if it occurs repeatedly. In this study, double low velocity impacts are numerically applied on the laminates by utilizing ply-level based modeling strategy. The impact results are then directly utilized to predict the residual compressive strength of the laminates by performing compression after impact simulation. Furthermore, the impact responses and the structural integrity of the laminated composites are compared for all configurations including single and double impact events for various distances. The results show that the distance between two impact positions provides different delamination interference mechanisms which are consistent with the previous experimental findings. These differences will lead to different energy dissipation and delamination area of the laminates. Moreover, the compressive strength of the laminates after impact loading reduces by approximately 50% for the present study configuration. Meanwhile, the implementation of a ply-level based modeling provides high computational efficiency

for predicting the impact response and the compressive strength of laminated composite structures.

Finally, fatigue after impact analysis of impacted L-shape composite laminates is performed. L-shape composite laminates are one of the geometrically complex parts of aircraft. Hence, it is essential to conduct a delamination behavior investigation of L-shape composite laminates when subjected to impact and cyclic loads, particularly on the sharply curved geometry. In this study, three different loading conditions are implemented sequentially including impact, static, and cyclic by means of the Finite Element Method. The low velocity impact is applied to obtain the delamination distribution by using an explicit simulation scheme. The delamination distribution due to impact is then utilized as the initial condition for static and cyclic loading conditions. By using an implicit simulation scheme, four different configurations are performed by combining positions and directions of the displacement to examine the maximum load bearing capacity of the laminates. Moreover, cyclic loading condition is performed to investigate the fatigue life of the L-shape laminates. It has to be noted that for cyclic loading, a user material (UMAT) is implemented into the FEM package ABAQUS to include a fatigue constitutive model for cohesive elements. The results showed that multilayered delamination is initiated due to the low velocity impact. The maximum load, the acceleration of the delamination propagation, and the mode mixity are mainly influenced by the delamination distributions as well as the loading configurations.

Kurzfassung

Leichtbaukonstruktionen wie laminierte Verbundwerkstoffe werden aufgrund ihrer außergewöhnlichen mechanischen Eigenschaften, wie z. B. hohe Steifigkeit im Verhältnis zum Gewicht und hohe Festigkeit im Verhältnis zum Gewicht, in verschiedenen Bereichen eingesetzt. Diese Werkstoffe zeichnen sich auch durch eine gute Umweltverträglichkeit und eine hervorragende Ermüdungsbeständigkeit aus und sind bei der Herstellung leicht zu formen. Allerdings weisen diese Werkstoffe komplexe Schädigungsmechanismen auf, wie z. B. Rissbildung in der Matrix, Faserbruch, plastizitätsähnliche Effekte und Delamination, da sie aufgrund der faserverstärkten Lagen und der Stapelung der Laminate ein anisotropes Verhalten aufweisen. Diese Schäden sind potenziell gefährlich, da sie die Tragfähigkeit erheblich verringern können, was zu einem Versagen führen kann. Delamination ist einer der häufigsten Defekte, die in laminierten Verbundwerkstoffen auftreten. Delaminationen treten in laminierten Verbundwerkstoffen von innen auf, so dass die Schäden mit bloßem Auge auf der Verbundwerkstoffoberfläche kaum sichtbar sind und folglich während des Betriebs nur schwer erkannt werden können.

Ziel dieser Dissertation ist es, die Leistungsfähigkeit der auf Lagenebene basierenden Modellierungsstrategien zur Vorhersage des Delaminationsverhaltens in laminierten Verbundwerkstoffen unter verschiedenen Belastungsszenarien und Simulationsschemata mit Hilfe fortschrittlicher Methoden im Rahmen der Finite-Elemente-Methode zu untersuchen. Eine Vielzahl von Belastungsszenarien, die häufig in technischen Anwendungen vorkommen, werden auf laminierte Verbundwerkstoffe angewandt und führen zu Delaminationen. Zu den Belastungsszenarien gehören reine und gemischte Belastungszustände, Stöße mit niedriger Geschwindigkeit, Druck nach dem Stoß und Ermüdung nach dem Stoß.

Im Rahmen der Finite-Elemente-Methode wird eine auf Lagenebene basierende Modellierungsstrategie zur Vorhersage des Delaminationsverhaltens von laminierten Verbundwerkstoffen unter reinen und gemischten Belastungsbedingungen vorgeschlagen. Jede Lage und jede Grenzfläche des Laminats wird explizit modelliert, wobei die Lagen durch verschiedene Elementtypen wie konventionelle Schalen-, Kontinuumsschalen- und Kontinuumselemente dargestellt werden und die Grenzflächen durch Kohäsionszonenelemente diskretisiert werden. Der Vergleich zwischen allen vorgeschlagenen Modellen wird hinsichtlich des Auftretens und des Wachstums von Delaminationen einschließlich der Last-Verschiebungskurven, der Delaminationsfläche, der Berechnungszeit und der Modenmischung untersucht. Die Ergebnisse zeigen, dass alle auf Lagenebene basierenden Modellierungsstrategien eine sehr gute Übereinstimmung mit den analytischen Ergebnissen aufweisen. Darüber hinaus bietet der auf Schalenelementen basierende Ply-Level-Ansatz in Kombination mit einem Kohäsivzonenelement mit endlicher Dicke ein numerisch effizientes Simulationswerkzeug zur Vorhersage von Delaminationen in Laminaten.

Darüber hinaus wird eine Studie über das transversale Scherverhalten eines homogenen isotropen Trägers mit ebener Dehnung für verschiedene Modellierungsstrategien auf Lagenebene durchgeführt. Aus den numerischen Vorhersagen lässt sich schließen, dass der auf Schalenelementen basierende Lagenansatz in Kombination mit dem Kohäsivzonen-Elementmodell mit endlicher Dicke eine sehr gute Übereinstimmung mit den analytischen Lösungen und dem zweidimensionalen ebenen Dehnungsmodell in Bezug auf Durchbiegung, Querschubspannung und normale Biegespannung bietet. Die Scherverformung wurde bereits in Kontinuumsmodellen berücksichtigt. Folglich führt die Verringerung der Steifigkeit der Kohäsionszonenelemente außerhalb der Ebene zu einem physikalisch nicht korrekten Modell, da sie nachgiebiger sind als die Referenzergebnisse und eine doppelte Scherverformung zu haben scheinen. Schließlich kann die Modifikation von $G_{xz} = G_{yz}$ durch Implementierung der orthotropen Elastizität von Kontinuumsmodellen verwendet werden, um die Referenzlösungen nachzuahmen.

Ein Aufprall mit niedriger Geschwindigkeit kann die strukturelle Integrität von Verbundwerkstoffen erheblich beeinträchtigen, was sich bei wiederholtem Auftreten noch verschlimmern kann. In dieser Studie werden doppelte Stöße mit niedriger Geschwindigkeit numerisch auf die Laminate angewendet, indem eine auf Lagenebene basierende Modellierungsstrategie

verwendet wird. Die Stoßergebnisse werden dann direkt zur Vorhersage der Restdruckfestigkeit der Laminate verwendet, indem die Kompression nach dem Stoß simuliert wird. Darüber hinaus werden die Aufprallreaktionen und die strukturelle Integrität der laminierten Verbundwerkstoffe für alle Konfigurationen, einschließlich Einzel- und Doppelaufprallereignisse für verschiedene Abstände, verglichen. Die Ergebnisse zeigen, dass der Abstand zwischen zwei Aufprallpositionen zu unterschiedlichen Delaminationsinterferenzmechanismen führt, was mit den früheren experimentellen Ergebnissen übereinstimmt. Diese Unterschiede führen zu einer unterschiedlichen Energiedissipation und Delaminationsfläche der Laminate. Darüber hinaus verringert sich die Druckfestigkeit der Laminate nach der Schlagbeanspruchung bei der vorliegenden Studienkonfiguration um ca. 50%. Die Implementierung einer auf Lagenebene basierenden Modellierung bietet eine hohe Berechnungseffizienz für die Vorhersage des Aufprallverhaltens und der Druckfestigkeit von laminierten Verbundstrukturen.

Schließlich wird eine Analyse der Ermüdung nach dem Aufprall von L-förmigen Verbundwerkstofflaminaten durchgeführt. L-förmige Verbundlaminate gehören zu den geometrisch komplexen Teilen von Flugzeugen. Daher ist es wichtig, das Delaminationsverhalten von L-förmigen Verbundlaminaten zu untersuchen, wenn sie Aufprall- und zyklischen Belastungen ausgesetzt sind, insbesondere bei stark gekrümmten Geometrien. In dieser Studie werden nacheinander drei verschiedene Belastungsbedingungen implementiert, darunter ein Aufprall, eine statische und eine zyklische Belastung mit Hilfe der Finite-Elemente-Methode. Der Aufprall mit niedriger Geschwindigkeit wird angewendet, um die Delaminationsverteilung mit Hilfe eines expliziten Simulationsschemas zu erhalten. Die Delaminationsverteilung infolge des Aufpralls wird dann als Anfangsbedingung für statische und zyklische Belastungsbedingungen verwendet. Unter Verwendung eines impliziten Simulationsschemas werden vier verschiedene Konfigurationen durch Kombination von Positionen und Richtungen der Verschiebung durchgeführt, um die maximale Tragfähigkeit der Laminate zu untersuchen. Außerdem wird eine zyklische Belastung durchgeführt, um die Ermüdungslebensdauer der L-förmigen Laminate zu untersuchen. Es ist anzumerken, dass für die zyklische Belastung ein Benutzermaterial (UMAT) in das FEM-Paket ABAQUS implementiert wurde, um ein Ermüdungskonstitutivmodell für kohäsive Elemente einzubeziehen. Die Ergebnisse zeigen, dass die mehrschichtige Delamination durch den Aufprall mit niedriger Geschwin-

digkeit ausgelöst wird. Die maximale Belastung, die Beschleunigung der Delaminationsausbreitung und die Modenmischung werden hauptsächlich von den Delaminationsverteilungen und den Belastungskonfigurationen beeinflusst.

Acknowledgement

This work was completed during my studies at the Institute of Lightweight Design and Structural Biomechanics (ILSB) at the Vienna University of Technology (TU Wien). The funding of my study by the Indonesian Ministry of Education, Culture, Research, and Technology (KEMDIKBUDRISTEK) and Österreichs Agentur für Bildung und Internationalisierung (OeAD-GmbH) in cooperation with ASEAN European Academic University Network (ASEA-UNINET) under Indonesia-Austria Scholarship Programme is gratefully acknowledged.

I want to express my deepest gratitude to my thesis advisor, Prof. Heinz E. Pettermann and Prof. Melanie Todt, for their valuable support, ideas, and suggestions throughout every stage of this work. Their positive attitude always encouraged me and the numerous discussions helped me to reflect scientifically and generate new ideas. Furthermore, I thank Prof. Clara Schuecker and Prof. Chiara Bisagni for acting as reviewers of my thesis.

I would like to thank all members of the ILSB for creating such a friendly and supportive work environment. My gratitude goes to the heads of the institute during my time at the ILSB, Prof. Philipp Thurner, Prof. Stefanie Elgeti, and Prof. Dieter Pahr. Special thanks go to my colleagues, Paul Hoffmann, Jan Kaul, Tilen Ceglar, Fabian Key, Pavan Kumar Asur Vijaya Kumar, Clemens David Fricke, Konstantin Key, and especially Marius Schasching, who all contributed numerous constructive as well as work distracting discussions and kept my spirits up. Additionally, I would like to thank Ms. Maria Grill for all of her administrative assistance and Mr. Gerhard Schneider for providing an excellent computational infrastructure.

Finally, I would like to thank my family and friends for their support and, especially my gorgeous wife Atin, my son Kai, and my daughter Ayca for being a part of my life and at my side throughout this work.

Contents

List of Figures

List of Tables

Nomenclature

Abbreviations

2D	Two–Dimensional
3D	Three–Dimensional
ASTM	American Standard Testing and Material
BK	Benzeggagh-Kenane
CAI	Compression After Impact
CBT	Corrected Beam Theory
CLS	Crack-Lap Shear
CPEZ	Continuum plane strain elements in combination with zero geometrical thickness cohesive zone element
CPLZ	Continuum elements in combination with zero geometrical thickness cohesive zone element
CPU	Central Processing Unit
CSPLZ	Continuum shell elements in combination with zero geometrical thickness cohesive zone element
CUS	Compression of Unimpacted Sample
CZE	Cohesive Zone Element
CZM	Cohesive Zone Model
DCB	Double Cantilever Beam
DOF	Degree of Freedom
EB	Euler-Bernoulli
ENF	End Notch Flexure
FAI	Fatigue After Impact
FEM	Finite Element Method
FRP	Fiber Reinforced Polymer
HVI	High Velocity Impact

LEFM	Linear Elastic Fracture Mechanics
LVI	Low Velocity Impact
MMB	Mixed-Mode Bending
SBT	Simple Beam Theory
SDEG	Stiffness Degradation
SLB	Single Leg Bending
SPLF	Shell elements in combination with finite geometrical thickness cohesive zone element
SPLZ	Shell elements in combination with zero geometrical thickness cohesive zone element
T	Timoshenko
TSL	Traction Separation Law
UD	Unidirectional
UMAT	User Material
VCCT	Virtual Crack Closure Technique

Symbols of recurring Latin Letters

A	mm^2	area
a	mm	delamination length
B	mm	width
b	mm	width of delamination front
C	-	Paris constant
c	-	speed of sound
D	N/mm^3	secant stiffness
d	-	damage
da/dN	mm/cycles	crack growth rate
E	N/mm^2	Young's modulus
F	-	correction factor
G	N/mm^2	shear modulus
$\mathcal{G}$	N/mm	strain energy release rate
h	mm	height
I	mm^4	second moment of area
K	N/mm^3	stiffness
L	mm	length

l	mm	element length
M	-	constant parameter
m	-	Paris constant
N	-	number of cycles
N'	-	correction factor
P	N	load
Q	-	constant parameter
q	N/mm	distributed load
r	mm	damage threshold
S	N/mm^2	shear strength
s	-	secant function
$\dot{\text{s}}$	-	tangent function
t	N/mm^2	traction or interfacial strength
u	mm	displacement
v	mm/s^2	velocity
X	N/mm^2	longitudinal strength
Y	N/mm^2	transverse strength

Symbols of recurring Greek Letters

β	-	mode-mixity in terms of separation
$\Delta\mathcal{G}$	N/mm	different of strain energy release rate
δ	mm	separation
$\bar{\delta}$	-	Kronecker delta
ε	-	normal strain
χ	-	correction factor
η	-	cohesive parameter
Γ	-	correction factor
γ	-	shear strain
λ	mm	effective separation
ν	-	Poisson's ratio
ΔN	-	number of cycles that is skipped to the next time step
∂	-	partial differentiation
ψ	-	mode-mixity in terms of strain energy release rate
σ	N/mm^2	normal stress

τ	N/mm^2	shear stress
θ	rad	rotation

Indices

+	tension
−	compression
0	initial value
C	critical value
cz	cohesive zone
cyc	cyclic
e	number of elements
f	final value or failure
i	represent each mode
ini	initial
j	represent each mode
J	integration point
I	mode I fracture
II	mode II fracture
III	mode III fracture
m	mixed mode I/II fracture
max	maximum
min	minimum
n	normal
s	shear
shear	Euclidean norm of shear and transverse
stat	static
t	current time step
$t+1$	next time step
tan	tangent
t	transverse
th	threshold
tot	total
x	x-direction
y	y-direction

z	z-direction
xy = yx	in-plane shear
xz = zx	out-of-plane shear 1
yz = zy	out-of-plane shear 2

Chapter 1

Introduction

1.1 Background

One significant technological development in the last few decades is the increasing use of high-performance lightweight materials by reducing the use of metal materials such as steel or aluminum. This development enables weight reductions in a variety of applications such as aircraft components. As a result, potential savings in production costs, fuel consumption, and the environmental impact of pollutant emissions can be obtained.

Nowadays, lightweight structures such as laminated composite are widely used not only in aerospace, but also in a variety of industries including automotive, maritime transportation, and sports [16]. This is mainly due to their exceptional mechanical characteristics such as high stiffness to weight and strength to weight ratios with reasonable prices. Furthermore, these materials also exhibit good environmental sustainability, excellent fatigue resistance, and are easy to form during manufacturing. Despite their superior performance, these materials are more complex than metal materials because they have an anisotropic behavior due to fiber reinforced plies and the stacking of the laminates. This leads laminated composites to possess complex damage mechanisms such as matrix cracking, fiber breakage, plasticity-like effects, and delamination [86]. Such damage in laminated composites is potentially dangerous because it can significantly reduce the load-carrying capacity,

which can lead to failure of the composite structure [25, 101]. In this respect, the damage tolerance of laminate composite structures subjected to various loading scenarios represent important design criteria.

Delamination, i.e. inter-laminar fracture, is one of the most dominant defects that arise in laminated composites. Mostly, delamination occurs internally in laminated composites so that damage is barely visible to the naked eye on the composite surface and, consequently, is difficult to detect during service. In engineering applications, delamination can be caused by a variety of factors. Firstly, delamination can occur due to manufacturing defects, such as voids, wrinkles, misaligned fibers, ply drop-offs, curved and tapered type corners, skin-stiffener interactions, bonded and bolted joints, access holes, and sandwich transitions that occur because of the inevitability of complex structural designs which cause interface tractions in the structure [11, 25]. Secondly, the delamination can be initiated by external load such as impact loading scenarios by creating damage in laminated composites, which can propagate and result in the separation of the layers. In addition, the delamination can also be introduced by tensile and shear loading scenarios that cause interface tractions originating in the loss of adhesion in curve sections, such as curved segments, tubular sections, cylinders and spheres, and pressurized containers [72]. Furthermore, delamination in laminated composites will propagate when loads of sufficient magnitude are applied to the structure. Thirdly, repeated loading and unloading of laminated composites can also lead to delamination over time. This is especially true when laminated composites are subjected to cyclic loading in a direction not parallel to the plane of the laminates. Fourthly, the difference in thermal expansion coefficients between the matrix and the reinforcement during the laminate's curing process will lead to different contractions between the plies which may lead to delamination [96]. Finally, the delamination in laminated composites can be caused by moisture absorption, which can weaken the bond between the layers over time [30]. In this regard, avoiding delamination, i.e. delamination initiation as well as propagation is the best option for maintaining the load-carrying capacity of laminated composites.

The delamination behavior of laminated composites has received significant attention in the last few decades treated by both experimental and numerical methods. Experimental schemes are usually employed for characterizing the delamination resistance of laminated composites, namely the critical strain energy release rate or the inter-laminar fracture toughness. Common experimental set-ups for observing the delamination behavior under mode I (opening mode), mode II (shear mode), and mode I/II (mixed-mode) loading scenarios. However, experimental methods are often less efficient, costly, and rarely used to test large scale and complex laminated composite structures. In this respect, numerical methods based on the Finite Element Method (FEM) provide a method for predicting the delamination behavior of laminated composites. Nevertheless, the investigation of local effects such as delamination in a composite structure is demanding in terms of computational resources. Consequently, the need for a computationally efficient modeling strategy, as well as high results reliability and wide application coverage, is indicated. This is where the motivation for this dissertation comes from. Furthermore, numerical methods are capable to estimate the nonlinear mechanical response at various length scales under various loading conditions [28].

A Cohesive Zone Model (CZM) is a common approach that has been applied to investigate the delamination behavior which has been first introduced by Dugdale [38] and Barenblatt [15]. The CZM has been implemented frequently in FEM analysis to simulate the delamination of laminated components [32, 59, 86, 103], as well as debonding [67], and crack propagation [51] for various loading conditions. Schwab et al. [85, 86] introduces a ply-level modeling based on shell element in combination with finite thickness cohesive zone elements (CZEs). They investigated the damage mechanism and failure behavior of fabric reinforced laminates as well as large composite components due to impact loading. In terms of computational performance, they found that the ply-level based model provides a very good compromise between numerical efficiency and accuracy of the results. However, the utilization of ply-level models based on shell elements combined with finite thickness CZE still does not cover various cases with different length scales and loading scenarios. There-

fore, it is necessary to conduct further research by utilizing the ply-level based modeling strategy that will be described in detail in this dissertation.

1.2 Aim and scope of the present work

The aim of this dissertation is to investigate the use of ply-level based modeling strategies in performing numerical analysis on laminated composites under various loading conditions and simulation schemes, by means of advanced methods within the framework of the FEM. A variety of loading scenarios that frequently occur in engineering applications will be applied to laminated composite, resulting in delamination. The loading scenarios include pure and mixed mode loading conditions, low velocity impact (LVI), compression after impact (CAI), and fatigue after impact (FAI). In general, the scope of the present work can be seen in Figure 1.1.

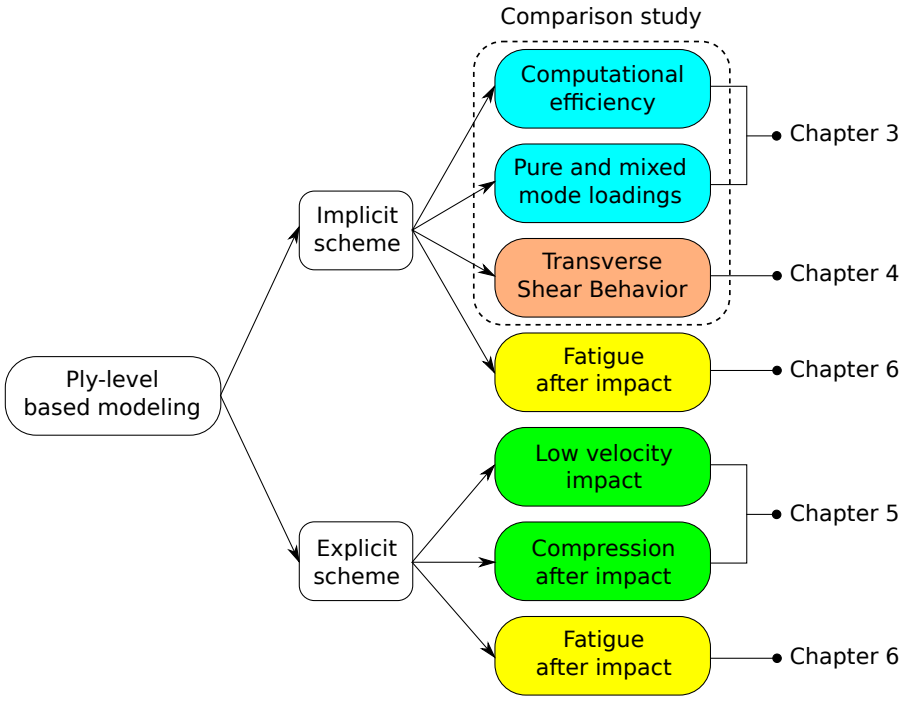

Figure 1.1: Scope of the present work.

In Chapter 2, a literature review on the topic of delamination on laminated composites is carried out. The first part focuses on the explanation of the delamination and its effect on the laminated composites. Three different methods for predicting delamination behavior in laminated composites is discussed including experimental, analytical, and numerical methods. The third part covers the analytical determination of delamination in laminated composite structures. The second part defines the cohesive damage model for predicting delamination behavior in laminated composites if subjected to cyclic loading conditions. The effect of low velocity impact towards delamination and the load bearing capacity of the laminates are described in the last part of Chapter 2.

In Chapter 3, a comparison study of the ply-level based modeling strategy is developed, which includes the two-dimensional (2D) and three-dimensional (3D) cases. The comparison is mainly focused on the computational efficiency and the reliability results of delamination behavior in laminated composites under pure and mixed mode loading conditions. The modeling approach is validated based on analytical examination by using corrected beam theory (CBT), where very good agreement between the simulations and analytical results is found. In addition, the predictions provide detailed insights into how efficient the modeling strategy is, which is beneficial for further applications, especially for complex laminated structures.

In Chapter 4, another comparison study of the transverse shear behavior of laminated composite is investigated. Three different ply-level based modeling strategies are compared in terms of deflection, transverse shear stress, and normal bending stress. The modeling approach is verified based on analytical calculations by using Euler-Bernoulli and Timoshenko's beam theories.

In Chapter 5, the failure and delamination behavior in laminated composites under single and double LVI and CAI is studied by performing a ply-level modeling strategy based on conventional shell elements in combination with finite geometrical thickness of cohesive zone element (CZE). Three different impact distances between two impact positions are compared in the contexts of impact response, energy dissipation, and delamination area

of the laminates. In addition, different delamination interference mechanisms are provided and prove to be consistent with the previous experimental findings. Moreover, the CAI simulation is applied for all impacted laminated composite plates, along with the unimpacted laminated composite plate to investigate the failure behavior and residual compressive strength of the laminated composites. Meanwhile, the implementation of a ply-level based modeling provides high computational efficiency for predicting the impact response and the compressive strength of laminated composite structures.

In Chapter 6, a delamination behavior investigation of L-shaped composite laminates when subjected to impact and cyclic loads, particularly on the sharply curved geometry is presented. In this Chapter, three different loading conditions are implemented sequentially including impact, static, and cyclic loads. The low velocity impact is applied to obtain the delamination distribution by using an explicit simulation scheme. The delamination distribution due to impact is then utilized as the initial condition for static and cyclic loading conditions. By using an implicit simulation scheme, four different configurations are performed by combining positions and directions of the displacement to examine the maximum load bearing capacity of the laminates. Moreover, cyclic loading conditions are performed to investigate the fatigue life of the L-shaped laminates. It has to be noted that for cyclic loading, a user material (UMAT) is implemented into the FEM package Abaqus/Standard 2020 (*Dassault Systèmes Simulia Corp., Providence, RI, USA*) to include a fatigue constitutive model for cohesive elements. The results showed that multilayered delamination is initiated due to the low velocity impact. The maximum load, the acceleration of the delamination propagation, and the mode-mixity are mainly influenced by the delamination distributions as well as the loading configurations.

Finally, Chapter 7 presents the summary of the results of delamination behavior in laminated composites.

Chapter 2

Literature review and theory

2.1 Delamination in Laminated Composites

Delamination is a failure mode where a material fractures into layers. A variety of materials including laminated composites can fail by delamination due to their relatively weak inter-laminar strengths. Depending on the position of the delamination in laminated composites, delamination can be categorized into three types including internal delamination, near-surface delamination, and multiple delamination as illustrated in Figure 2.1 [20, 21]. Internal delamination typically occurs in the inner ply interfaces of the laminates and is frequently generated by transverse matrix cracks in plies orthogonal to the tensile force. Consequently, this type of delamination is difficult to observe by the naked eye and is potentially dangerous because it can significantly reduce the load-carrying capacity, which

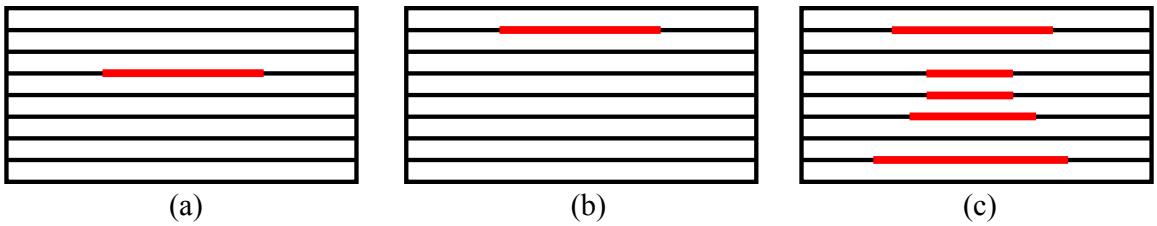

Figure 2.1: Delamination types including (a) internal delamination (b) near-surface delamination, and (c) multiple delamination.

can lead to failure of the composite structure [25, 103]. Additionally, the total flexure behavior of the laminates will change significantly when compressive loads are applied to the laminate[103].

Near-surface delaminations are originated near the surface of the laminates. Bolotin [20, 21] categorized several types of near-surface delamination which can be introduced in laminated composites under various loading conditions as shown in Figure 2.2. Even though near-surface delamination is not too difficult to observe by the naked eye, it represents a more complex scenario than internal delamination since its behavior under compressive load, under surface heating, and sometimes under tension (due to Poisson's effect) is often accompanied by buckling [20]. In addition, the deformation of the delaminated part is independent of the deformation of the laminate. Therefore, the local stability of the laminate must be considered as well as the propagation of near-surface delamination and inter-laminar damage. It has to be noted that the local instability and near-surface delamination propa-

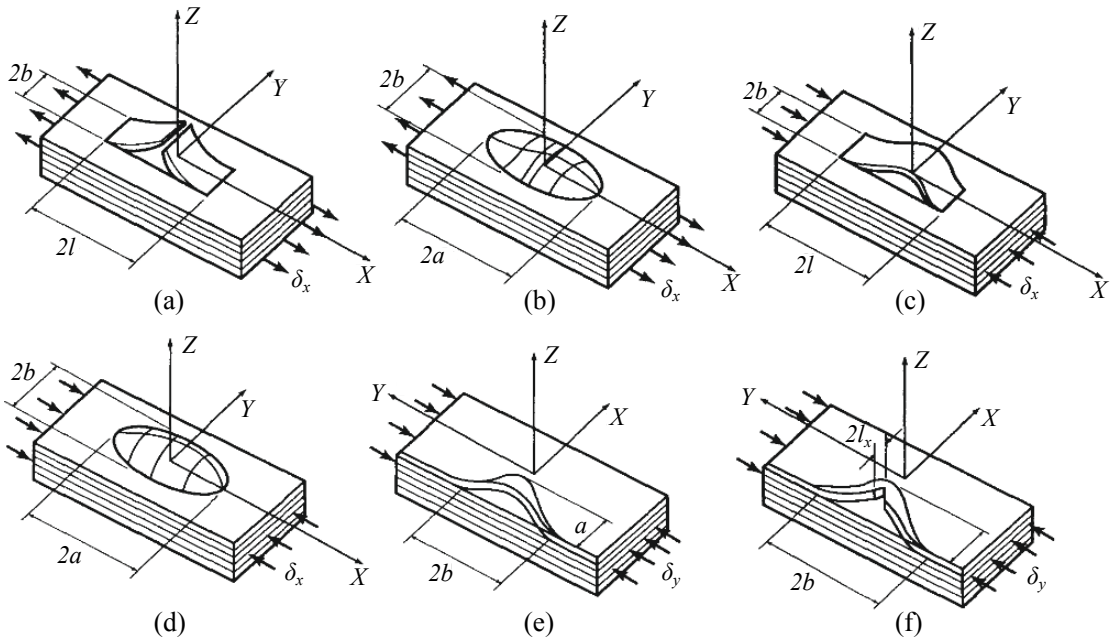

Figure 2.2: Near-surface delamination classifications. (a) open delamination in tension; (b) closed delamination in tension; (c) open buckled delamination; (d) closed buckled delamination; (e) edge buckled delamination; and (f) edge buckled delamination with a secondary crack (Figure adapted from Bolotin [20]).

gation of structural components such as columns, plates, and shells under compression may result in global instability. As a result, predicting the load-carrying capacity of composite structures with delaminations is typically required a simultaneous consideration of damage, fracture, local buckling, and global stability. Multiple delaminations with no fiber breakage and matrix cracking are a combination of internal and near-surface delaminations. This type of delamination is mainly caused by external mechanical loads such as low velocity impact and thermal load as well as environmental effects such as moisture.

Depending on the loading conditions, the delamination can be considered as three different modes of fracture proposed by Irwin [52] as shown in Figure 2.3. In mode I (opening mode), the structure is loaded with tensile forces in such a way that the crack faces separate in a direction normal to the plane of the delamination. Mode II (sliding shear mode), corresponds to the shear forces being loaded parallel to the crack surfaces, resulting in the sliding of the crack faces over each other in the direction perpendicular to the crack front. In mode III (tearing shear mode), the structure is loaded by shear forces parallel to the crack front, and the crack surfaces slide over each other in the direction parallel to the crack front. However, mixed mode loading conditions also occur frequently in engineering applications.

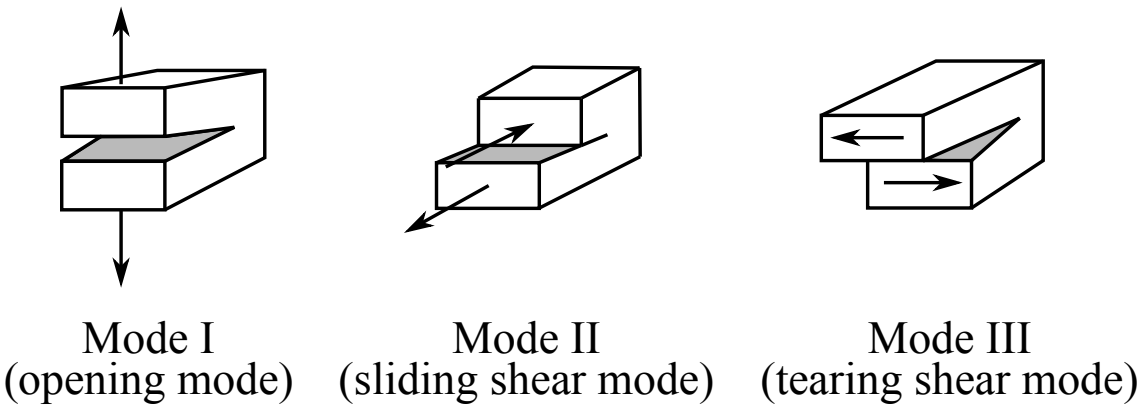

Figure 2.3: Fracture modes for different loading conditions [76].

The delamination behavior of laminated composites due to different loading conditions had been previously studied experimentally, analytically, and numerically. The details of these three methods are discussed in the following Sections.

2.1.1 Experimental methods

Several experimental methods have been developed in order to characterize the delamination resistance of laminates, namely the inter-laminar fracture toughness or critical strain energy release rate. The inter-laminar fracture toughness can be obtained by employing the Double Cantilever Beam (DCB) [11, 103] and End Notch Flexure (ENF) [11, 103] test set-ups to examine the delamination behavior under mode I and mode II, respectively. For mixed mode (I/II) delamination, the inter-laminar fracture toughness can be observed by implementing Mixed-Mode Bending (MMB) [103], Single Leg Bending (SLB) [11], and Crack-Lap Shear (CLS)[2] test set-ups. The emphasis in this dissertation is only on the DCB, ENF, and SLB test set-ups which represent the mode I, mode II, and mode I/II delamination characterizations, respectively. The experimental set-ups of DCB, ENF, and SLB are presented in Figures 2.4(a), 2.4(b), and 2.4(c), respectively.

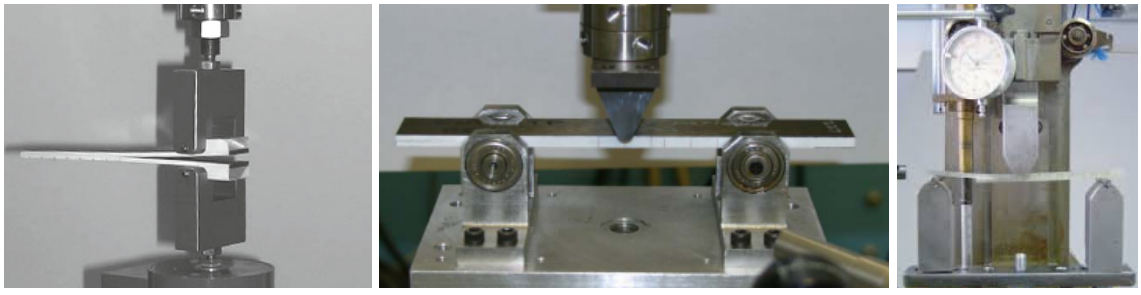

Figure 2.4: Experimental setup for (a) mode I Double Cantilever Beam test [66], (b) mode II End Notch Flexure test [69], and (c) mixed mode I/II Single Leg Bending test [95].

2.1.2 Analytical methods

The analytical calculation of the load-displacement curve, delamination length, and the strain energy release rate of the DCB, ENF, and SLB test set-ups can be defined based on the corrected beam theory (CBT) equations. The CBT equations are described as follows.

DCB (Mode I delamination)

Figure 2.5(a) illustrates a cantilever beam that has a length of $2L$, thickness of h, and width of B. Initial delamination, a, is applied. A displacement is introduced at $x = 0$ at the top and bottom edges of the cantilever beam applying only one translational degree of freedom in z-direction is applied. Figure 2.5(b) presents the deformed shape of the specimen when positive and negative z-direction displacements are applied to the corresponding edges.

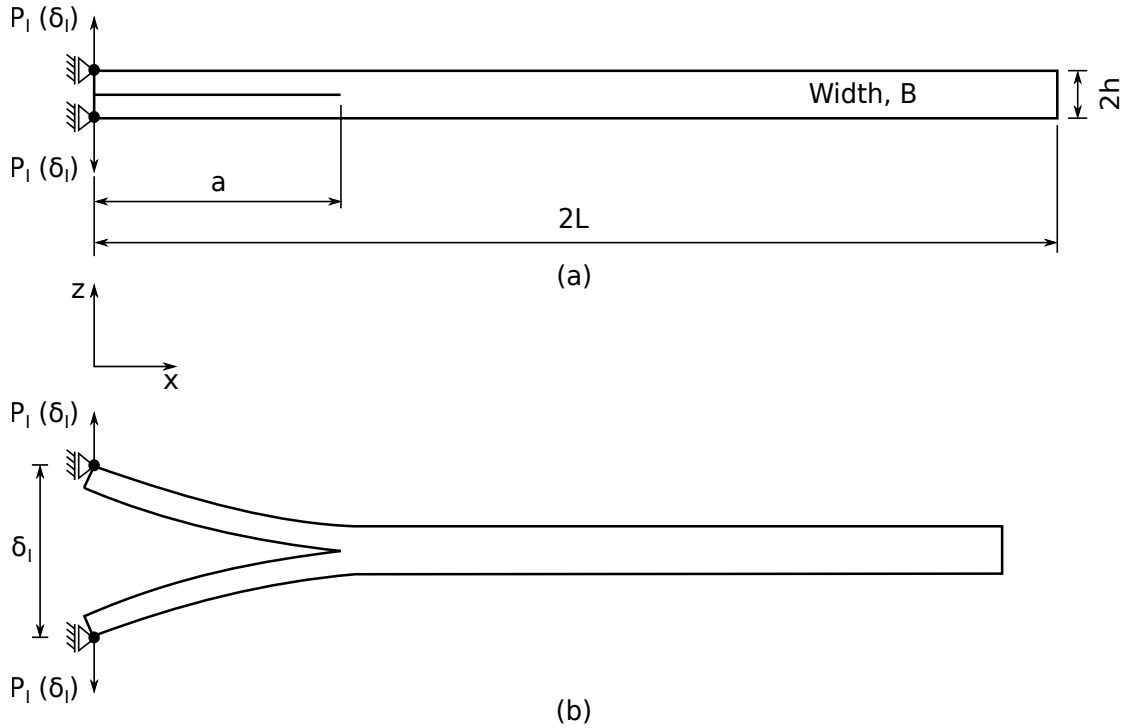

Figure 2.5: Double cantilever Beam test set-up.

Analytically, a Simple Beam Theory (SBT) can be used to calculate the distance between cantilever beam tips, δ_{I} [47]. The δ_{I} can be obtained by

$$\delta_{\mathrm{I}} = \frac{2P_{\mathrm{I}}a^3}{3E_{\mathrm{x}}I} \tag{2.1}$$

$$I = \frac{Bh^3}{12} \tag{2.2}$$

where P_{I} is the applied load for mode I loading condition, I is the second moment of area along the beam length, and E_{x} is Young's modulus of the beam. However, deflections and rotations at the crack tip have to be considered in the real application. Thus, Corrected Beam Theory (CBT) is applied by adding the artificial length of χh to the crack length a [48]. Therefore, Equation (2.1) can be written as

$$\delta_{\mathrm{I}} = \frac{2P_{\mathrm{I}}(a+\chi h)^3}{3E_{\mathrm{x}}I} \tag{2.3}$$

where χ is the correction factor and h is the beam thickness. An analytical value of χ is defined as

$$\chi = \sqrt{\frac{E_{\mathrm{x}}}{11G_{\mathrm{xz}}}\left[3 - 2\left(\frac{\Gamma}{1+\Gamma}\right)^2\right]} \tag{2.4}$$

and

$$\Gamma = 1.18\frac{\sqrt{E_{\mathrm{x}}E_{\mathrm{z}}}}{G_{\mathrm{xz}}} \tag{2.5}$$

where E_{z} and G_{xz} are transverse Young's and transverse shear modulus, respectively. Moreover, the mode I strain energy release rate is given by [77]

$$\mathcal{G}_{\mathrm{I}} = \frac{P_{\mathrm{I}}^2(a+\chi h)^2}{BE_{\mathrm{x}}I} \tag{2.6}$$

Equations (2.3) and (2.6) can only be implemented until the critical mode I strain energy release rate, $\mathcal{G}_{\mathrm{IC}}$, is reached. In other words, there is no delamination propagation. If the delamination is propagated, the load-displacement response and the delamination extension can be obtained by combining Equations 2.3 and 2.6 and set the $\mathcal{G}_{\mathrm{IC}}$ instead of $\mathcal{G}_{\mathrm{I}}$ which is defined as

$$P_{\mathrm{I}} = \sqrt{\frac{2}{3}}\left(\frac{B^3\mathcal{G}_{\mathrm{IC}}^3 E_{\mathrm{x}} I}{\delta_{\mathrm{I}}^2}\right)^{\frac{1}{4}} \tag{2.7}$$

Furthermore, the delamination length is not an initial value anymore and has to be evaluated. The delamination length during propagation can be calculated by

$$a = \sqrt[3]{\frac{3\delta_{\mathrm{I}} E_{\mathrm{x}} I}{2P_{\mathrm{I}}}} - \chi h \tag{2.8}$$

ENF (Mode II delamination)

Having a similar geometry as the DCB test, the ENF test set up is illustrated in Figure 2.6. Generally, three point ENF test of the laminated composites is conducted, where the initial delamination length a should be at least 0.7 times the length L in order to improve the stability of the delamination propagation [27, 37]. By using the same principles as for the DCB test, the correction factor of 0.42 χh is added to the delamination length [77]. Therefore, CBT can be defined as

$$\delta_{\mathrm{II}} = \frac{3P_{\mathrm{II}}(a + 0.42\chi h)^3 + 2P_{\mathrm{II}}L^3}{96E_{\mathrm{x}} I} \tag{2.9}$$

where P_{II} is the applied load for mode II loading condition, δ_{II} is the central displacement for ENF test set up. Moreover, the mode II strain energy release rate can be defined as

$$\mathcal{G}_{\mathrm{II}} = \frac{3(a + 0.42\chi h)^2 P_{\mathrm{II}}^2}{64BE_{\mathrm{x}} I} \tag{2.10}$$

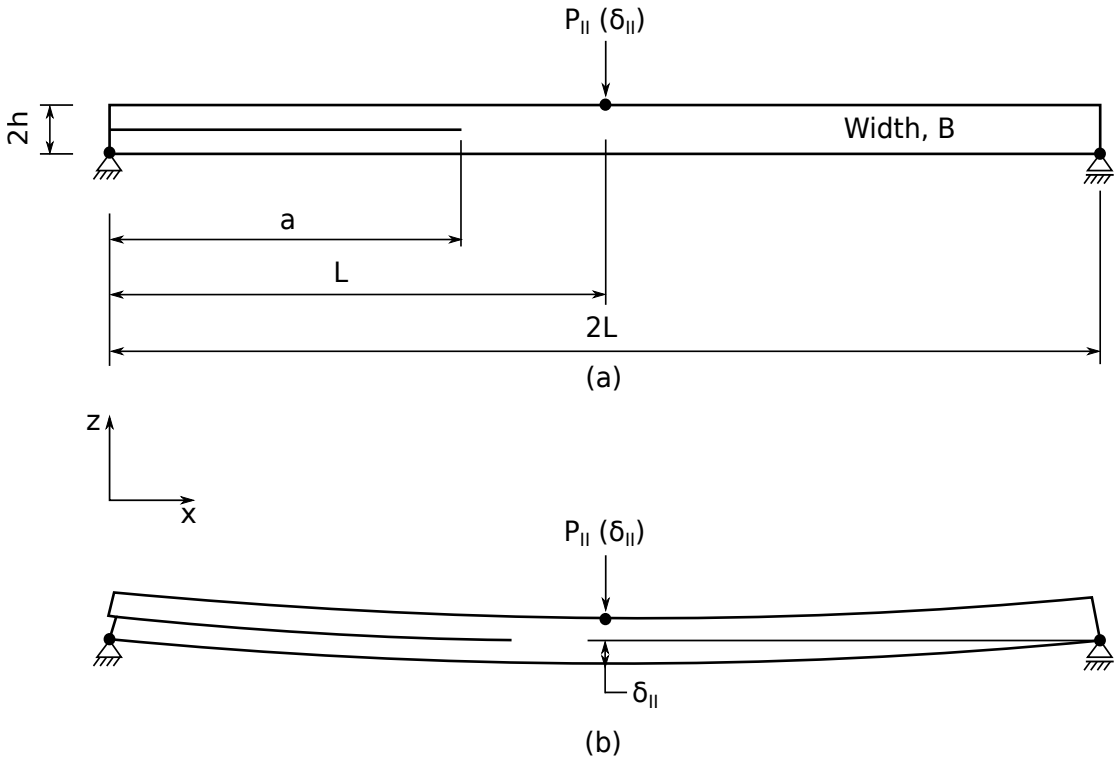

Figure 2.6: End Notch Flexure test set-up.

Again, Equations (2.9) and (2.10) can only be implemented until the critical mode II strain energy release rate, $\mathcal{G}_{\mathrm{IIC}}$, is reached which the delamination is not propagated. Furthermore, the delamination extension can be obtained by combining Equations (2.9) and (2.10) and set the $\mathcal{G}_{\mathrm{IIC}}$ instead of $\mathcal{G}_{\mathrm{II}}$ as defined in Equation (2.10). In addition, the length of delamination during propagation can be calculated by modifying Equation (2.10) into

$$a = \frac{1}{P_{\mathrm{II}}}\sqrt{\frac{64\mathcal{G}_{\mathrm{IIC}}BE_{\mathrm{x}}I}{3}} - 0.42\chi h \tag{2.11}$$

Finally, the load-displacement response during delamination propagation can be obtained by inserting a in Equation (2.11) into Equation (2.9). Therefore, this load-displacement response can be expressed as

$$\delta_{\mathrm{II}} = \frac{1}{96E_{\mathrm{x}}I}\left[\frac{3}{P_{\mathrm{II}}^2}\left(\frac{64\mathcal{G}_{\mathrm{IIC}}BE_{\mathrm{x}}I}{3}\right)^{\frac{3}{2}} + 2L^2P_{\mathrm{II}}\right], \qquad \delta_{\mathrm{II}} \geq \delta_{\mathrm{IIC}} \tag{2.12}$$

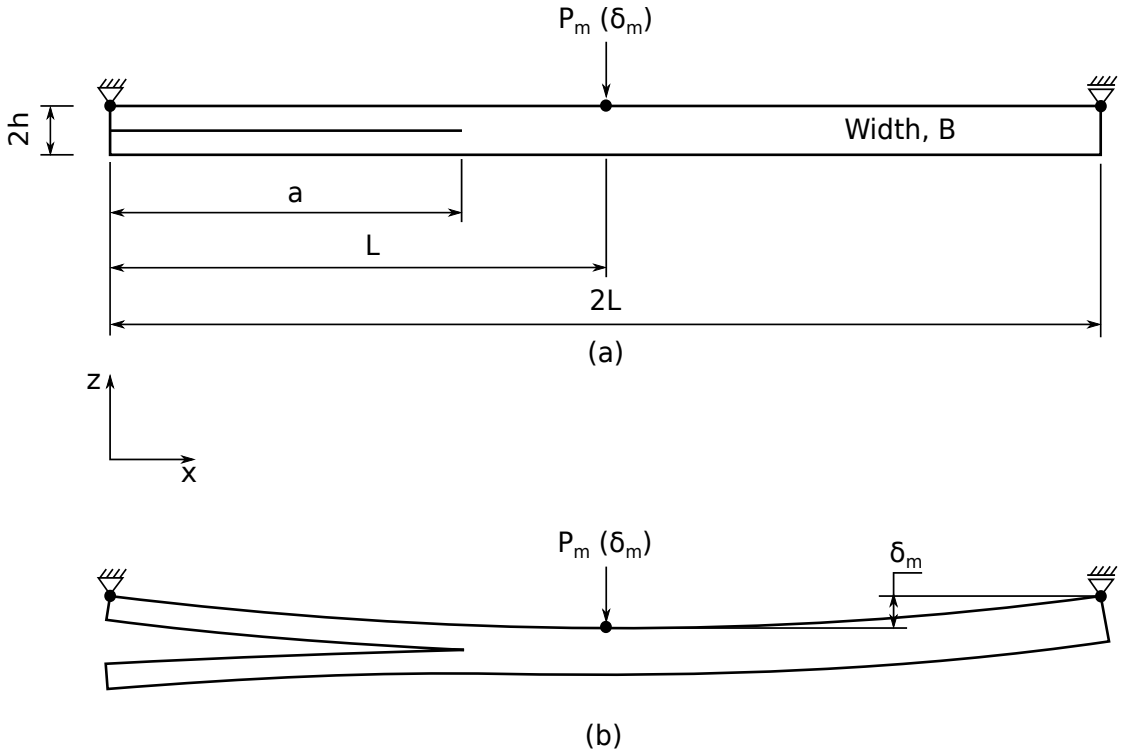

Figure 2.7: Single Leg Bending test set-up.

SLB (Mixed-mode I/II delamination)

Following the same principle as the ENF test set up, the SLB test set up is illustrated in Figure 2.7. It can be seen that the central displacement is given by [54] as

$$\delta_{\mathrm{m}} = \frac{P_{\mathrm{m}} N' [7(a + 0.42\chi h)^3 + (L + 2\chi h)^3]}{2Bh^3 E_{\mathrm{x}}} \tag{2.13}$$

where P_{m} is the applied load for mixed mode loading condition, δ_{m} is the central displacement for SLB test set up, and N' is a correction factor for large displacements (refer to the work of [54]). Moreover, the mode I and mode II strain energy release rates are also given by [54] as

$$\mathcal{G}_{\mathrm{I}} = \frac{3FP_{\mathrm{m}}^2 (a + \chi h)^2}{B^2 h^3 E_{\mathrm{x}}} \tag{2.14}$$

$$\mathcal{G}_{\mathrm{II}} = \frac{9FP_{\mathrm{m}}^2(a+0.42\chi h)^2}{4B^2h^3E_{\mathrm{x}}} \tag{2.15}$$

where F is also a correction factor for large displacements (refer to the work of [54]). The analytical load, P_{m}, at which mixed-mode delamination propagation begins is calculated using the Benzeggagh-Kenane (BK) criterion [17, 76] given by

$$\frac{\mathcal{G}_{\mathrm{tot}}}{\mathcal{G}_{\mathrm{IC}} + (\mathcal{G}_{\mathrm{IIC}} - \mathcal{G}_{\mathrm{IC}})(\psi)^{\eta}} \geq 1 \tag{2.16}$$

where η is a mixed mode parameter obtained from experiments and ψ is the mode-mixity that can be obtained by using

$$\psi = \frac{\mathcal{G}_{\mathrm{II}}}{\mathcal{G}_{\mathrm{tot}}} \tag{2.17}$$

and

$$\mathcal{G}_{\mathrm{tot}} = \mathcal{G}_{\mathrm{I}} + \mathcal{G}_{\mathrm{II}} \tag{2.18}$$

2.1.3 Numerical methods

Numerical methods provide further development in the delamination behavior of laminated composites. Not only for experimental standard cases but the numerical method by means of Finite Element Method (FEM) can also be performed to investigate the delamination behavior of complex and large scale laminate structures. A common approach that has been widely utilized to predict delamination within the framework of damage mechanics is Cohesive Zone Modeling (CZM) which offers an efficient way of simulating delamination initiation and propagation of laminate structures [101]. The CZM is implemented by generating a cohesive damage zone in front of the delamination tip. The model was first introduced in the work of Dugdale [38]. He originated the concept that stresses in the material are controlled by yield stress and that a thin plastic zone is formed in front of the

notch. Furthermore, Barenblatt [15] has presented cohesive forces to solve the problem of equilibrium in elastic structures with cracks on a molecular scale. Since then, the CZM is widely implemented to simulate the crack and delamination propagation [59, 86, 103] as well as debonding [67], and crack propagation [51]. Importantly, Hillerborg's concept also allowed new cracks to initiate.

For practical reasons, the CZM approach needs less computational effort compared to other fracture mechanics based approaches like e.g. the Virtual Crack Closure Technique (VCCT) because of its simplicity and capability to make predictions without pre-existing cracks [11]. The CZM also allows the unification of crack initiation and growth within one model, thus, damage tolerance and strength evaluations can be done with the same design tool [101]. Schwab et al. [86] have proved that the CZM approach can be used for investigating a variety of fracture problems with high computational efficiency. The flexibility of the mesh size is also offered by employing the CZM even though it is computationally more expensive [19] and the reliability of the results needs to be validated by performing mesh sensitivity analysis. Finally, not only suitable for static analysis, the CZM can be used to simulate the fatigue damage initiation and the propagation by accounting for the number of load cycles into the static CZM.

The damage of the cohesive zone model is defined by the traction-separation law (TSL), which describes the relationship between cohesive traction and displacement separation acting across the interface where delamination may occur. The TSL is represented by three parameters including the traction separation law shape, the inter-laminar strength, and the critical energy release rate. The traction separation law may have various shapes that have been implemented in previous studies as shown in Figure 2.8. A comparison study of the TSL shape effect law on the application of CZM has been done by Alfano [3]. Alfano compared four different TSLs including bi-linear, trapezoidal, exponential, and linear-parabolic under static loading conditions. He discovered that for the DCB test, the solutions were practically independent of the shape of the TSL. The effect of the TSL was found on the numerical performance and the level of accuracy achieved. Particularly, the trapezoidal TSL gave the worst results in terms of numerical stability and convergence of

the finite element solution to the exact solution. The exponential TSL was found to be optimal in terms of accuracy, while the bi-linear TSL was the best compromise between computational efficiency and accuracy.

The bi-linear form is widely used to simulate interface damage in laminated composites. For a bi-linear TSL, the inter-laminar strength, $t_{\mathrm{i}}^{\mathrm{o}}$ is used to define the maximum traction where the damage initiation occurs as illustrated in Figure 2.9. The critical energy release rate or fracture toughness, $\mathcal{G}_{\mathrm{C}}$ is the property that expresses the interface resistance to delamination propagation. When the energy release rate which shows as the area under the traction-separation curve is equal to the critical energy release rate, the traction is reduced to zero, and a new delamination area is formed.

2.2 Constitutive Model of Cohesive Damage Mechanism

The constitutive model of the interface damage mechanism is required for modeling the cohesive zone element degradation based on bi-linear TSL as shown in Figure 2.10. Turon et al. [13, 94, 101] have proposed a constitutive model of quasi-static and cyclic cohesive damage mechanism under pure and mixed mode loading conditions that will be implemented in this dissertation. A Paris law like approach based on the non–local measurement of the energy release rate [13] and the measurement of the cohesive area [101] is implemented to account for the delamination propagation for cyclic loads in which the envelope displacement is utilized.

2.2.1 Quasi static model

The constitutive model for the quasi static case includes the delamination onset and propagation. The main parameter of the constitutive model is the effective separation which is used to compare different stages of the separation so that it is possible to define such concepts as loading, unloading, and reloading. Effective separation is defined as

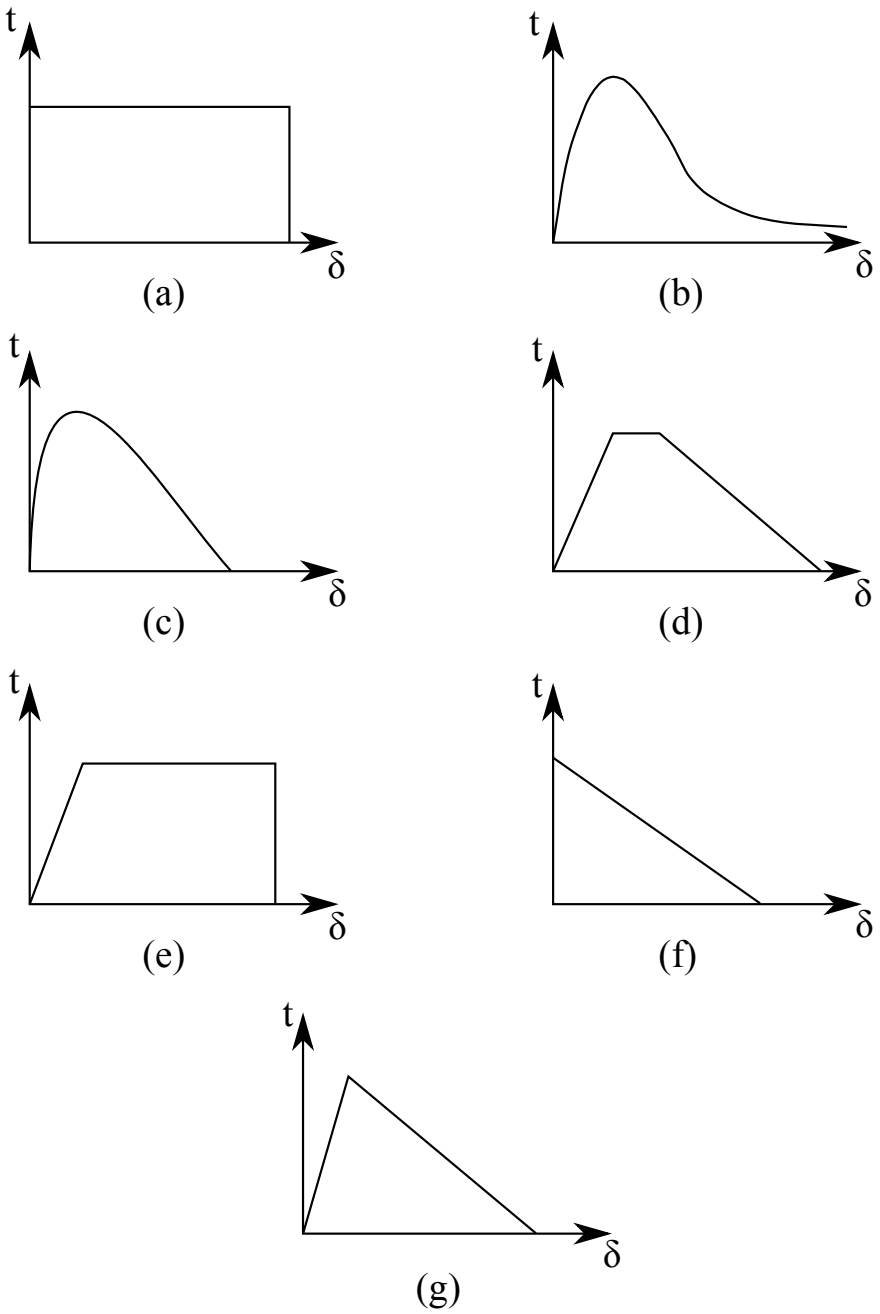

Figure 2.8: Various cohesive traction separation law shapes: (a) constant [38], (b) exponential [15], (c) polynomial [67], (d) tri-linear [105], (e) tri-linear [31], (f) linear [24], and (g) bi-linear [44].

$$\lambda = \sqrt{\langle \delta_{\mathrm{n}} \rangle^2 + \left(\delta_{\mathrm{shear}}\right)^2} \tag{2.19}$$

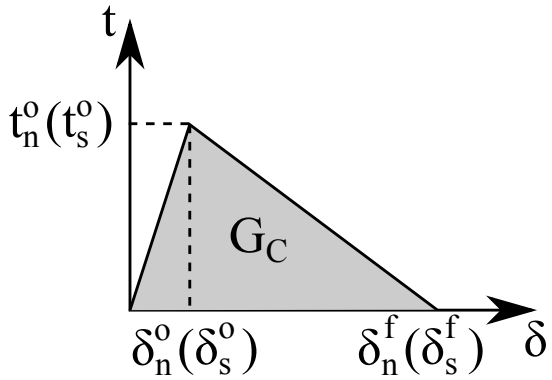

Figure 2.9: Traction-separation curve in the cohesive zone in front of delamination tip.

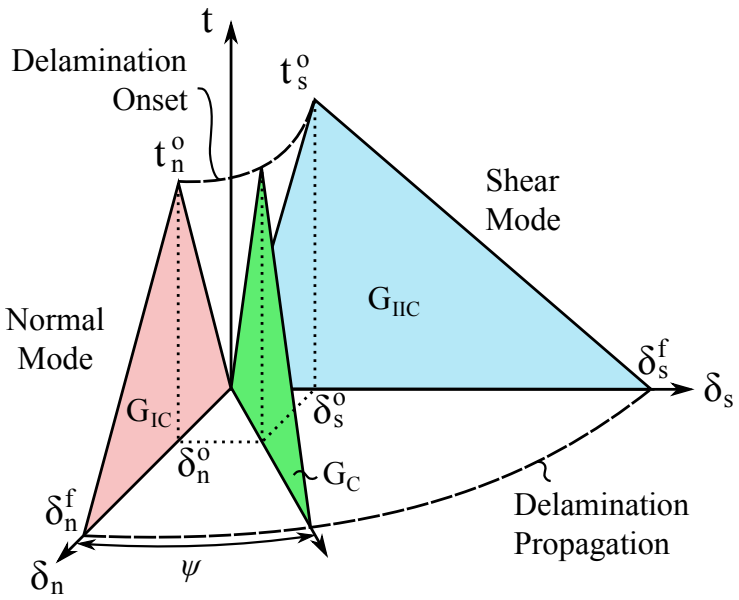

Figure 2.10: A bi-linear traction–separation law (modified from [64])

$$\delta_{\text{shear}} = \sqrt{\left(\delta_{\text{s}}\right)^2 + \left(\delta_{\text{t}}\right)^2} \tag{2.20}$$

where δ_{n} is the separation in opening mode (mode I) and δ_{shear} is the Euclidean norm of the separation in sliding shear mode, δ_{s} (mode II) and in tearing shear mode, δ_{t} (mode III). The Macaulay bracket is used for δ_{n} to omit negative values. Therefore, if δ_{n} is smaller than zero, it represents a compressive mode I loading and assumes that there is no damage at the interface. Since the model uses a bi-linear traction separation law, so, the onset

separation, δ^0, and the final separation, δ^{f} have to be calculated. The onset separation is calculated for each mode by

$$\delta_i^0 = \frac{t_i^0}{K} \qquad i = \mathrm{n}, \mathrm{shear} \tag{2.21}$$

where t_i^0 are the traction or interfacial strengths for normal and shear modes and K is the interface stiffness. For mixed-mode loading case, the β and ψ constants should be defined to characterize the mixed-mode ratios, where β is shear and total separations ratio and ψ is the shear and total strain energy release rates ratio. These constants are given by Turon [99] as

$$\beta = \frac{\delta_{\mathrm{shear}}}{\langle \delta_{\mathrm{n}} \rangle + (\delta_{\mathrm{shear}})} \tag{2.22}$$

$$\psi = \frac{\beta^2}{1 + 2\beta^2 - 2\beta} \tag{2.23}$$

After these constants are known, the initial and final separation for mixed-mode condition can be determined by

$$\delta^0 = \sqrt{\langle \delta_{\mathrm{n}}^0 \rangle^2 + \left[\left(\delta_{\mathrm{shear}}^0 \right)^2 - \langle \delta_{\mathrm{n}}^0 \rangle^2 \right] (\psi)^\eta} \tag{2.24}$$

$$\delta^{\mathrm{f}} = \frac{2}{K\delta^0} \left[\mathcal{G}_{\mathrm{IC}} + (\mathcal{G}_{\mathrm{IIC}} - \mathcal{G}_{\mathrm{IC}})(\psi)^\eta \right] \tag{2.25}$$

if the δ^{f} is sufficiently large to cause damage to the model, the damage threshold needs to be defined. The damage threshold is determined by onset and final separations which can be calculated by

$$r = \frac{\delta^0 \delta^{\mathrm{f}}}{\delta^f - \mathrm{d}[\delta^{\mathrm{f}} - \delta^0]} \tag{2.26}$$

where d is damage. Furthermore, the constitutive tangent tensor needs to be defined for the numerical implementation. The constitutive tangent tensor can be obtained from the secant equation differentiation. Turon et al. [99] defined the secant equation as

$$\mathrm{s_i} = (1-\mathrm{d})D^0_{\mathrm{ij}}\delta_{\mathrm{j}} - \mathrm{d}D^0_{\mathrm{ij}}\bar{\delta}_{\mathrm{nj}}\langle -\delta_{\mathrm{n}}\rangle \tag{2.27}$$

where D^0_{ij} is the undamaged stiffness tensor which defined as

$$D^0_{\mathrm{ij}} = \bar{\delta}_{\mathrm{ij}}K \tag{2.28}$$

By differentiating Equation (2.27), the constitutive tangent tensor can be expressed as

$$\dot{\mathrm{s}}_{\mathrm{i}} = D_{\mathrm{ij}}\dot{\delta}_{\mathrm{j}} - \bar{\delta}_{\mathrm{ij}}K\left[1+\bar{\delta}_{\mathrm{nj}}\frac{\langle -\delta_{\mathrm{j}}\rangle}{\delta_{\mathrm{j}}}\right]\delta_{\mathrm{j}}\dot{\mathrm{d}} \tag{2.29}$$

where D_{ij} is secant stiffness and $\bar{\delta}_{\mathrm{ij}}$ is Kronecker delta. The secant stiffness can be defined as

$$D_{\mathrm{ij}} = \bar{\delta}_{\mathrm{ij}}K\left[1-\mathrm{d}\left(1+\bar{\delta}_{\mathrm{nj}}\frac{\langle -\delta_{\mathrm{j}}\rangle}{\delta_{\mathrm{j}}}\right)\right] \tag{2.30}$$

Moreover, the tangent stiffness $D^{\mathrm{tan}}_{\mathrm{ij}}$ is required to define the strain increments for the next time step. This is obtained by

$$D^{\mathrm{tan}}_{\mathrm{ij}} = \begin{cases} \left(D_{\mathrm{ij}} - K\left[1+\bar{\delta}_{\mathrm{nj}}\frac{\langle -\delta_{\mathrm{j}}\rangle}{\delta_{\mathrm{j}}}\right]\left[1+\bar{\delta}_{\mathrm{nj}}\frac{\langle -\delta_{\mathrm{j}}\rangle}{\delta_{\mathrm{j}}}\right]\frac{\delta^{\mathrm{f}}\delta^0}{\delta^{\mathrm{f}}-\delta^0}\frac{1}{\lambda^3}\delta_{\mathrm{i}}\delta_{\mathrm{j}}\right) & r<\lambda<\delta^{\mathrm{f}} \\ D_{\mathrm{ij}} & r>\lambda \text{ or } \delta^{\mathrm{f}}<\lambda \end{cases} \tag{2.31}$$

The transverse shear stiffness decreases by a multiple of the stiffness of interface if the effective separation is between the damage threshold and the final separation. However,

the transverse shear stiffness does not decrease if the effective separation is not within this interval.

2.2.2 Cyclic model

The cyclic model is predicted on the assumption that quasi static and cyclic damages can be calculated independently. The damage due to quasi static load is calculated with the equations from Section 2.2.1. The damage due to cyclic load is calculated using the procedure described in this section as developed in [100]. This model is based on a relationship between the damage evolution and the crack growth rate which can be expressed as

$$\frac{\partial \mathrm{d}}{\partial N} = \frac{\partial \mathrm{d}}{\partial A_\mathrm{d}} \frac{\partial A_\mathrm{d}}{\partial N} \tag{2.32}$$

where A_d is the damaged area and $\frac{\partial A_\mathrm{d}}{\partial N}$ is the growth rate of the damaged area. The last term is a material property that can be related to the Paris relation with:

$$\frac{\partial A_d}{\partial N} = \frac{A^\mathrm{e}}{A_\mathrm{CZ}} \frac{da}{dN} \Leftrightarrow \frac{da}{dN} = \frac{A_\mathrm{CZ}}{A^\mathrm{e}} \frac{\partial A_d}{\partial N} \tag{2.33}$$

$\frac{A_\mathrm{CZ}}{A^\mathrm{e}}$ is the ratio that shows how many elements are in the cohesive zone. Considering that the damaged area with respect to the element size ratio is equal to the dissipated energy over the critical strain energy release rate ratio, Turon et al. [102] provide an equation for calculating the damaged area with respect to the element size ratio i.e.

$$\frac{A_\mathrm{d}}{A^\mathrm{e}} = \frac{\mathrm{d}\delta^0}{\delta^\mathrm{f}(1-\mathrm{d}) + \mathrm{d}\delta^0} \tag{2.34}$$

By combining Equations (2.32), (2.33) and (2.34), the following equation is obtained.

$$\frac{\partial \mathrm{d}}{\partial N} = \frac{1}{A_\mathrm{CZ}} \frac{(\delta^f(1-\mathrm{d}) + \mathrm{d}\delta^0)^2}{\delta^\mathrm{f}\delta^0} \frac{da}{dN} \tag{2.35}$$

Here, A_CZ is the area of the cohesive zone. For mode I, this value can be obtained by

$$A_{\mathrm{CZ}} = B\frac{9\pi}{32}\frac{E_{\mathrm{n}}\mathcal{G}_{\max}}{(t_{\mathrm{n}}^{0})^{2}} \tag{2.36}$$

where E_{n} is Young's modulus in the normal direction, t_{n}^{0} is the traction in opening mode, and $\mathcal{G}_{\max}$ is the maximum strain energy release rate during the loading cycle, and The parameter B is the width of the delamination front. The parameter $\frac{9\pi}{32}$ is a fitting parameter. From Equation (2.35) it can be seen that the damage evolution variables depend on the cohesive zone area, the shape of TSL, the damage in the previous loading cycle, and the crack growth rate. The crack growth rate depend on the loading and material properties that have been defined by Paris [74] as

$$da/dN = \begin{cases} C\Delta\mathcal{G}^{m} & \text{if} \quad \mathcal{G}_{\mathrm{th}} < \Delta\mathcal{G} < \mathcal{G}_{\mathrm{C}} \\ 0 & \text{otherwise} \end{cases} \tag{2.37}$$

where $\Delta\mathcal{G} = \mathcal{G}_{\max}$ - $\mathcal{G}_{\min}$ and the coefficients C and m of the Paris' law for the mixed–mode loading conditions are calculated by the following formulae [18]

$$log(C) = log(C_{\mathrm{I}}) + log(C_{\mathrm{m}})\psi + log(\frac{C_{\mathrm{II}}}{C_{\mathrm{m}}C_{\mathrm{I}}})\psi^{2} \tag{2.38}$$

$$m = m_{\mathrm{I}} + m_{\mathrm{m}}\psi + (m_{\mathrm{II}} - m_{\mathrm{I}} - m_{\mathrm{m}})\psi^{2} \tag{2.39}$$

where C_{I}, C_{II}, m_{I}, and m_{II} are the pure mode parameters and C_{m}, m_{m} are mixed–mode parameters. If $\Delta\mathcal{G}$ is lower than $\mathcal{G}_{\mathrm{th}}$, the loading is not sufficiently high to lead crack propagation. Whereas, if $\Delta\mathcal{G}$ is higher than $\mathcal{G}_{\mathrm{C}}$, the crack growth rate is unstable and triggers catastrophic failure. In this condition, the crack growth rate is no longer follows Equation (2.37). The $\mathcal{G}_{\max}$ and $\Delta\mathcal{G}$ used in the Paris's Law can be computed using the area under the TSL of the cohesive zone model as can be seen in Figure 2.11. So, $\mathcal{G}_{\max}$ can be calculated by

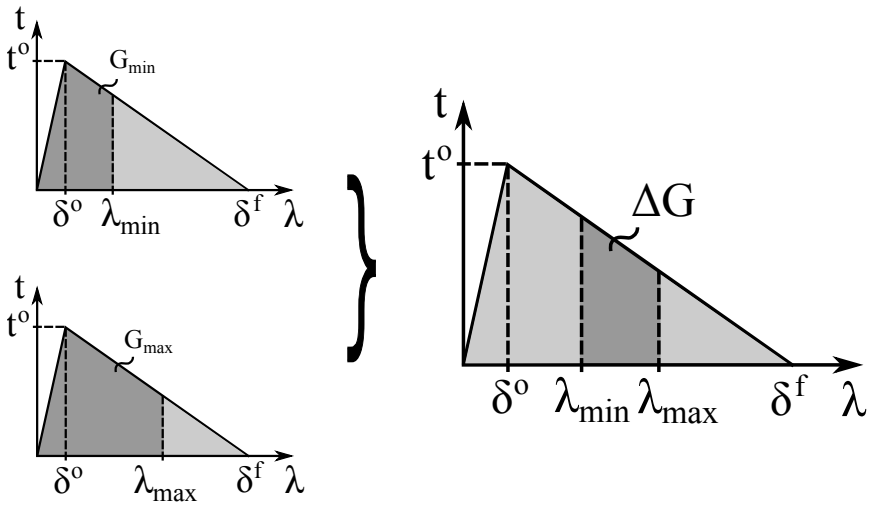

Figure 2.11: Variation of the energy release rate (adopted from [101])

$$\mathcal{G}_{\max} = \frac{t^0}{2}\left[\delta^{\mathrm{f}} - \frac{(\delta^{\mathrm{f}} - \lambda_{\max})^2}{\delta^{\mathrm{f}} - \delta^0}\right] \tag{2.40}$$

where $\lambda_{\max}$ is the maximum separation during the cyclic loads. For mixed-mode loading condition, the $\mathcal{G}_{\mathrm{th}}$ and $\mathcal{G}_{\mathrm{C}}$ should be defined using the BK criterion [17]. Moreover, the implementation of the cycle jump strategy is preferable when the process involves high-cycle fatigue compared to cycle by cycle strategy [99]. This cycle jump strategy used in this study is based on the strategy described by Van Paepegem and Degrieck [71]. They describe that the damage variable at time step $i + \Delta N_i$, at integration point J is calculated by

$$\mathrm{d}^J_{i+\Delta N_i} = \mathrm{d}^J_i + \frac{\partial \mathrm{d}^J_i}{\partial N}\Delta N_i \tag{2.41}$$

where d^J_i and $\frac{\partial \mathrm{d}^J_i}{\partial N}$ are the damage variable and the damage growth rate at time step i, respectively. ΔN_i is the number of cycles skipped to the next time step. It should be noted that the accuracy of the results will depend on the number of cycles skipped . To determine this number, the maximum damage increment is selected from which the number of jumped cycles is calculated by

$$\Delta N_i = \frac{\Delta \mathrm{d}_{\max}}{\max\left\{\frac{\partial \mathrm{d}_i^J}{\partial N}\right\}} \tag{2.42}$$

The results will be less accurate when $\Delta \mathrm{d}_{\max}$ is increased, but the analysis will proceed more quickly, vice versa. Finally, the total damage can be determined by adding the damage caused by the quasi-static loads and the damage caused by the cyclic loads i.e.

$$\mathrm{d}_{\mathrm{tot}} = \mathrm{d}_{\mathrm{stat}} + \mathrm{d}_{\mathrm{cyc}} = \mathrm{d}_{\mathrm{stat}} + \mathrm{d}_{i+\Delta N_i}^J \tag{2.43}$$

If the total damage is known, Equations (2.30) and (2.31) can be determined.

If multiple opening modes are present during the analysis, a formulation for a mode-dependent cohesive zone area and a mode-dependent penalty stiffness must be included with certain adjustments. The first adjustment is the addition of a mode-dependent penalty stiffness as proposed by Turon et al. [104]. It is developed in order to address variations in the local mixed-mode ratio. The formulation for obtaining the shear mode penalty stiffness is

$$\frac{K_{\mathrm{shear}}}{K_{\mathrm{n}}} = \frac{\mathcal{G}_{\mathrm{IC}}}{\mathcal{G}_{\mathrm{IIC}}}\left(\frac{t^0_{\mathrm{shear}}}{t^0_{\mathrm{n}}}\right)^2 \tag{2.44}$$

where t^0_{shear} and t^0_{n} are the inter-laminar strengths for the shear and normal modes, $\mathcal{G}_{\mathrm{IC}}$ and $\mathcal{G}_{\mathrm{IIC}}$ are the pure mode strain energy release rate and K_{n} is the penalty stiffness for normal mode. If K_{shear} is known, the mode dependent penalty stiffness can be determined by

$$K_\psi = K_{\mathrm{n}}(1-\psi) + \psi K_{\mathrm{shear}} \tag{2.45}$$

where ψ is the local mixed-mode ratio, calculated using the formula

$$\psi = \frac{K_{\mathrm{shear}}\delta^2_{\mathrm{shear}}}{K_{\mathrm{shear}}\delta^2_{\mathrm{shear}} + K_{\mathrm{n}}\langle\delta_{\mathrm{n}}\rangle^2} \tag{2.46}$$

δ_{shear} stands for shear separation which is computed according to the same equation as in the original model. The effective separation for mixed-mode case is then calculated by

$$\lambda = \frac{K_{\text{shear}}\delta_{\text{shear}}^2 + K_{\text{n}}\langle\delta_{\text{n}}\rangle^2}{\sqrt{K_{\text{shear}}^2\delta_{\text{shear}}^2 + K_{\text{n}}^2\langle\delta_{\text{n}}\rangle^2}} \tag{2.47}$$

Moreover, the mixed-mode onset and critical separation are obtained from the following equation.

$$\lambda^0 = \sqrt{\frac{K_{\text{n}}\langle\delta_{\text{n}}\rangle^2 + [K_{\text{shear}}(\delta_{\text{shear}}^0)^2 - K_{\text{n}}(\delta_{\text{n}}^0)^2]\psi^\eta}{K_\psi}} \tag{2.48}$$

$$\lambda^{\text{c}} = \frac{K_{\text{n}}\delta_{\text{n}}^0\delta_{\text{n}}^c + [K_{\text{shear}}\delta_{\text{shear}}^0\delta_{\text{shear}}^c - K_{\text{n}}\delta_{\text{n}}^0\delta_{\text{n}}^c]\psi^\eta}{K_\psi\lambda^0} \tag{2.49}$$

The formulae for the penalty stiffness and the different separations in the original model are replaced with these new estimation.

Additional adjustments are required to include the mode-dependent cohesive zone area formulation as proposed by Turon et al. [102]. The determination of the cohesive zone area in the original model is based on material parameters for mode I. For mixed-mode case, this is adapted by including parameters for mode II for more accurate calculation of the cohesive zone area. First, the mixed-mode Young's modulus is defined as

$$E_{\text{m}} = E_{\text{I}}(1-\psi) + E_{\text{II}}\psi \tag{2.50}$$

where ψ is the local mixed-mode ratio and E_{I} and E_{II} are the equivalent Young's modulus for the separate modes which can be obtained by

$$E_{\text{I}} = \frac{E_{\text{y}}}{\mathcal{Q}} \tag{2.51}$$

$$E_{\mathrm{II}} = \frac{E_{\mathrm{y}}}{\mathcal{Q}} \sqrt{\frac{E_{\mathrm{x}}}{E_{\mathrm{y}}}} \tag{2.52}$$

where

$$\mathcal{Q} = \frac{1}{2} \sqrt{2 \left[\sqrt{\frac{E_{\mathrm{x}}}{E_{\mathrm{y}}}} - \nu_{\mathrm{xy}} \right] + \frac{E_{\mathrm{y}}}{G_{\mathrm{xy}}}} \tag{2.53}$$

If E_{m} is known, a new cohesive zone area can be obtained by

$$A_{\mathrm{CZ}} = B \frac{9\pi}{32} \frac{E_{\mathrm{m}} \mathcal{G}_{\mathrm{C}}}{(t_{\mathrm{m}}^0)^2} \tag{2.54}$$

where $\mathcal{G}_{\mathrm{C}}$ is the critical strain energy release rate for mixed-mode case and t_{m}^0 is the mixed-mode inter-laminar strength which is calculated by

$$(t_{\mathrm{m}}^0)^2 = (t_{\mathrm{n}}^0)^2 + [(t_{\mathrm{shear}}^0)^2 - (t_{\mathrm{n}}^0)^2] \psi^{\eta} \tag{2.55}$$

With these two adjustments, the behavior under mixed-mode loading conditions can be represented more precisely when mode-dependent penalty stiffness and cohesive zone area are added to the original model.

2.3 Delamination due to Low Velocity Impact

Laminated composites are susceptible to impact damage due to the weak transverse load-carrying capacity [83]. Impact loading conditions on laminated composites can cause complex damage such as matrix cracking, fiber breakage, plasticity-like effects, penetration, and delamination [10, 40, 53, 61, 85, 86]. These damages have to be considered during design and maintenance of composite aircraft structures [84, 91, 106]. There, investigating the damage mechanisms especially delamination of laminated composites under impact loading

conditions is an important consideration in order to increase the impact resistance and the residual strength after impact of laminated composite structures.

Impact loading of laminated composites is generally classified into low, intermediate, high/ ballistic, and hyper velocity regimes, as they will lead to different damage mechanisms and failure behavior [1, 107]. Abrate [1], Sjöblom et al. [90] and Cantwell [26] explain that low-velocity impacts can occur due to high impactor mass with impact velocity lower than 10 m/s such as drop tools. Abrate [1] also explains that the intermediate velocity impacts can be caused by whirlwinds, hurricanes, or tornadoes on runways with velocities between 10 and 50 m/s. Moreover, high velocity/ballistic impacts are usually triggered by projectiles being fired or weapons exploding at 50-1000 m/s. Meanwhile, hyper velocity impacts have velocities higher than 2.5 km/s, such as micrometeorites in low earth orbit. The different impact velocities, material properties, the mass of the impactor, and the stiffness of the laminates will cause different structural responses as illustrated in Figure 2.12. In most cases, responses to very short impact durations are dominated by stress wave propagation in the thickness direction. These scenarios are commonly denoted as high velocity impacts (HVI), cf. Figure 2.12(a). On the contrary, quasi static like responses are observed for very long impact durations, where these situations are often denoted as LVI, cf. Figure 2.12(c). In the transition between these two scenarios, the response is dominated by flexural waves, cf. Figure 2.12(b). Additionally, several criteria have been proposed to identify the occurring response type, for example, the one presented in Refs. [14, 35],

$$v_0 = c\varepsilon_\mathrm{f} \tag{2.56}$$

which gives an estimate of the transition impact velocity, v_0 , based on the through thickness speed of sound of the considered material, c, and the failure strain of the material, ε_f. Impact velocities that are significantly lower than the transition velocity are supposed to lead to LVI like responses whereas impact velocities which are significantly higher than the transition velocity are supposed to lead to HVI like responses. Assuming a failure strain of $\varepsilon_\mathrm{f} = 1\%$ this criterion gives the transition to stress wave dominated responses at impact

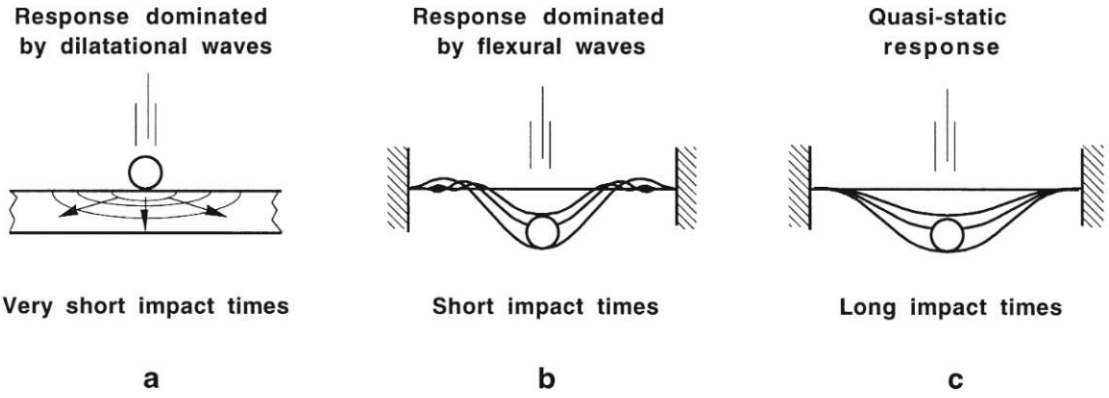

Figure 2.12: Response types of plates during impact loading. Taken from Ref. [68]

velocities above 20 m/s for common epoxy composites. Another criterion presented by Olsson [68], states that the impact response is governed by the ratio of impactor and target mass. Moreover, Olsson [68] also states limiting mass ratios for distinguishing between large (quasi static like), intermediate, and small mass (wave controlled) impact situations. Davies and Robinson [36, 80] define an LVI as a stressing process in which the stress wave in the thickness direction of the laminate has no particular influence on the damage behavior and present a simple model for delimiting high-velocity impacts. Furthermore, Liu and Malvern [61] as well as Joshi and Sun [53] classify the impact process according to the respective damage mechanisms. For example, LVI mainly shows delamination and matrix cracking, whereas HVI penetration and fiber breakage is the main failure criteria. Low velocity impact (LVI) testing is frequently performed to investigate the composite damage tolerance in order to improve the lightweight design of laminated composite structures.

In the case of delamination occurrences, there are three phases of low velocity impact event as can be seen in Figure 2.13. Firstly, before the collision, laminates have no delamination at each interface. Secondly, during the collision, delamination occurs at the interface until the velocity of the impactor is reduced to zero when the impactor has reached its maximum displacement. When this stage is attained, cone-shaped delamination occurs. Furthermore, the impactor bounces because the internal energy of the laminates is transferred back to the impactor. Finally, multiple delaminations are deployed when the impactor bounces back

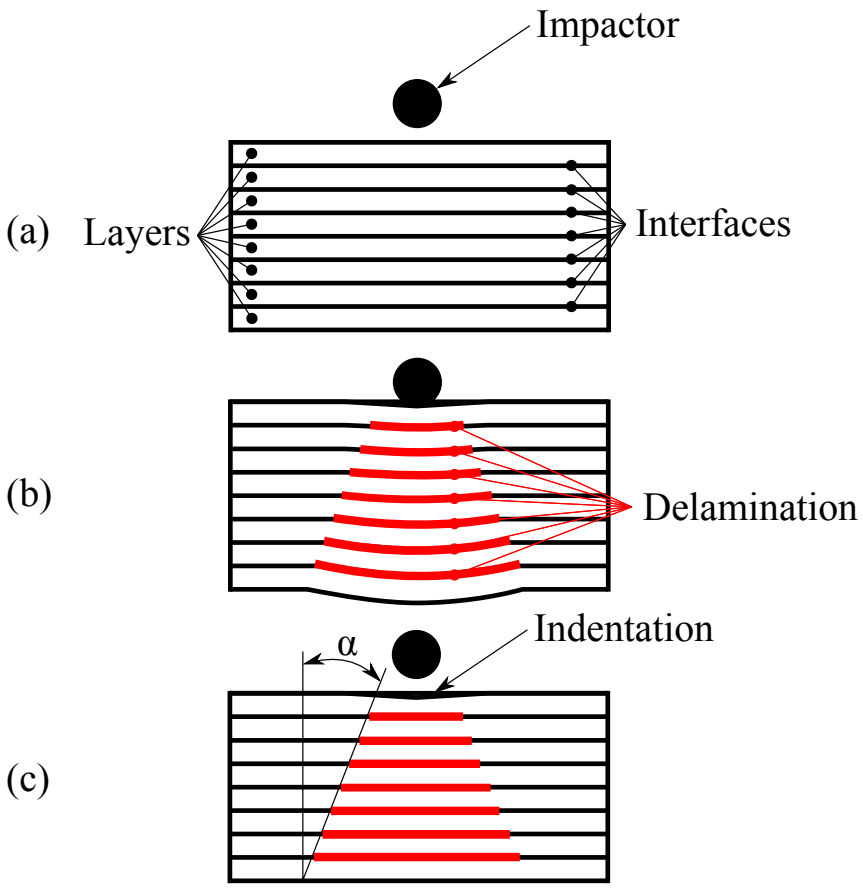

Figure 2.13: Illustration of laminated composites under low velocity impact. (a) before collision; (b) at impact velocity of 0 m/s or at maximum displacement of the impactor; and (c) after the impactor bounce back completely.

entirely. The angle, α presents the shape of the delamination at the last stage. This angle is influenced by several factors such as impact energy, laminate thickness, and the impactor geometry. As in the case of internal delamination, the multiple delaminations also have an effect on the load-carrying capability and lifetime of laminated composite structures.

A review of the LVI behavior of laminated composites is given in Ref. [79]. In aircraft applications, LVI damage is not only caused by operational activities such as hailstone strikes and runway debris but also by maintenance and service activities including part movement and incidental tool drops. Consequently, laminated composite structures are usually exposed to complex multiple impact environments [57, 60, 88]. Thus, understanding the damage

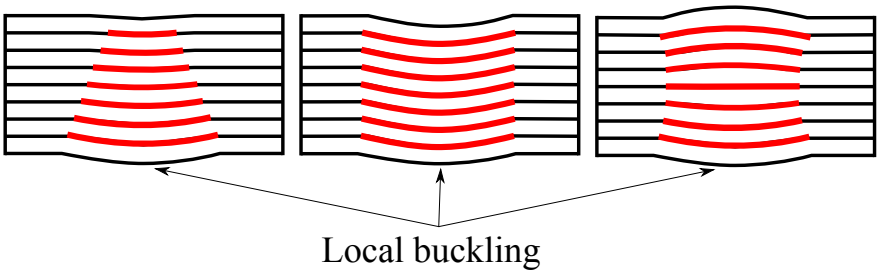

Figure 2.14: Local buckling of the impacted laminates under compression.

mechanisms and failure behavior of laminated composites under multiple LVIs is important. Furthermore, impact resistance and damage tolerance as two standard indicators have been created to measure the performance of composite materials under out-of-plane stresses [19, 82, 89]. The amount of absorbed energy and induced damage generated by a certain impact energy characterize the impact resistance of the composite material. The damage tolerance is defined as the ability to retain undamaged or original strength, which is assessed by evaluating residual strength after impact [89], particularly in compression. The residual compressive strength of impacted laminated composites is commonly obtained by performing compression after impact (CAI) experiments which are usually conducted with quasi static uni-axial compressive load. During the CAI test, complex local buckling might also occur and has to be considered, since near-surface delamination also occurs in multiple delamination. Figure 2.14 illustrates the local buckling that possibly occurs in impact laminated composites under compression or cyclic compression. These possibilities can be developed by combining unbuckled delamination, closed delamination in tension, and closed buckled delamination. The combinations are mainly influenced by several factors such as the delamination area at each interface, material properties, fiber orientation, and the compression load itself. It has to be noted that global buckling may occur in laminates if the delamination area is large.

Multiple LVIs and CAI tests on laminated composites have been extensively done both experimentally and numerically over the last few decades. Andrew et al. [5] used an acoustic emission monitoring technique to evaluate the compressive damage process for repaired and

unrepaired laminated glass fiber reinforced composites after repeated impacts at the same position. Liao et al. [57] investigated experimentally the effect of double LVI positions on impact response and damage interference mechanism for laminated composites. They revealed that the interference status for mechanical curves directly corresponded to the impact-induced damage modes at different impact energy. Moreover, for a double impact event at the same position, the maximum indentation of the second impactor is higher than the first one due to the decreasing bending stiffness caused by the first impact. Saleh et al. [82] investigated the residual compressive strength of laminated composites with different fabric architectures after repeated LVIs. They found that the residual strength of 3D woven composites is significantly higher than that of 2D plain woven specimens resulting in sudden catastrophic damage. Anuse et al. [6] have analyzed the residual compressive strength of carbon fiber reinforced composite laminates with different ply orientation sequences by using experimental and numerical methods. Three different energy levels have been studied to explore the LVI of laminated composites. They discovered that even with barely visible impact damages, the residual compressive strength of the laminated composites has been significantly decreased.

Generally, the experimental procedure provides insight into the general impact behavior of the specimens under certain loading conditions. However, studying a variety of different loading scenarios is time consuming and costly. It is even more difficult to investigate the impact behavior and structural integrity of large-scale and complex structures. Meanwhile, numerical procedures provide capabilities to predict the nonlinear mechanical behavior including damage mechanisms and failure behavior of laminated composites under impact loading conditions at various length scales [28]. Still, for highly nonlinear mechanical responses due to impact loading, numerical methods need high computational time. Therefore, an efficient modeling strategy must be used to accelerate the computational analyses while still predicting reliable results.

Chapter 3

Ply-level based modeling approach

3.1 Introduction

The delamination behavior of laminated composites has received a significant attention in the last few decades conducted by both experimental and numerical methods. Numerical methods are more efficient and can be used to test large-scale and complex laminated composite structures than experimental methods. Nevertheless, the investigation of local effects such as delamination in a composites structure is demanding in terms of computation resources. Consequently, the need for computationally efficient methodologies is required. A Cohesive Zone Model (CZM) is a common approach that has been applied to investigate the delamination behavior which has been demonstrated to have considerable computational efficiency [86].

Typically, laminated composites are geometrically modeled as a stack of homogeneous orthotropic layers representing the individual plies. At mesoscale level, ply-level models are used where every ply and every interface of the laminate is modeled explicitly. Ply-level models have been widely used by employing various element types for the plies in combination with different cohesive zone modeling techniques [4]. Schwab and Pettermann [85] have combined shell elements with finite thickness cohesive zone elements (CZE) to simulate the failure mechanisms due to impact events on fabric reinforced laminated composites. The

modeling approaches based on shell elements show accurate results and present an excellent performance in terms of computational efficiency compared to models based on continuum elements. Shell elements connected by zero thickness CZEs have been applied in the work of Gager and Pettermann [41] and also the work of Borg et al. [22]. The formulation allows for surface based coupling and takes into account the thickness and kinematics of the involved shell elements [41]. Even though this technique offers more flexibility regarding the mesh size of the CZEs and adjacent plies, it is computationally more expensive [19]. Continuum shell elements are an option to represent the plies [63]. Then, the cohesive zone is modeled with zero thickness and coupled to adjacent plies. Bae et al. [11] have used plane strain continuum elements and three-dimensional (3D) continuum solid elements together with zero thickness CZEs to examine the delamination behavior of composites. In terms of elastic response, critical loads, and load–displacement curves, the numerically predicted results have matched those obtained by experiments.

The focus of this paper is on the comparison between different ply-level models in terms of the validity of delamination prediction in laminated composites and computational efficiency by means of the Finite Element Method. The laminates are subjected to pure and mixed mode loading conditions. Five different ply-level models including two-dimensional continuum plane strain, shell, continuum shell, and three-dimensional continuum solid elements with zero-thickness CZEs, and shell elements with finite-thickness CZEs are used. DCB and ENF test set ups according to DIN EN 6033 and 6034 standards are utilized for investigating the pure mode cases, respectively, by using the commercial FEM package Abaqus/Standard 2020 (*Dassault Systèmes Simulia Corp., Providence, RI, USA*). For, mixed-mode cases, a Single Leg Bending (SLB) test set ups is used. Analytical results based on Corrected Beam Theory (CBT) (see Sections 2.1.2 to 2.1.2) serve as the reference result. The comparison between all proposed models is examined in terms of delamination response including load-displacement curves, delamination area, computation time, and mode-mixity during delamination propagation. Finally, the computational efficiency is evaluated in terms of the computation time.

3.2 Modelling approach

Ply-level modeling approaches with various choices of element types are studied. For all test set-ups considered in the following, the delamination front is straight and well inside the laminate, thus the plane strain assumption applies. In this context, the plies could be represented by beam elements coupled by 2D CZEs. However, as ply-level models are of special interest for predicting the behavior of large and complex components under tri-axial loading conditions, the approach is exemplified by recourse to shell elements. The study includes conventional shell elements, continuum shell elements, continuum solid elements, and continuum plane strain elements.

The various modeling strategies are illustrated in Figure 3.1 where only one interface with its adjacent plies is shown. Figure 3.1(a) presents a ply-level model that is composed of shell elements for the plies, together with CZEs of finite geometrical thickness, denoted as SPLF. The constitutive thickness of the CZEs is set to be equal to the geometrical thickness. The nodes at the midplanes of the shell elements are shared with the nodes of the CZE. In this modeling strategy, the CZE thickness is equal to the adjacent ply thicknesses, i.e. half of the

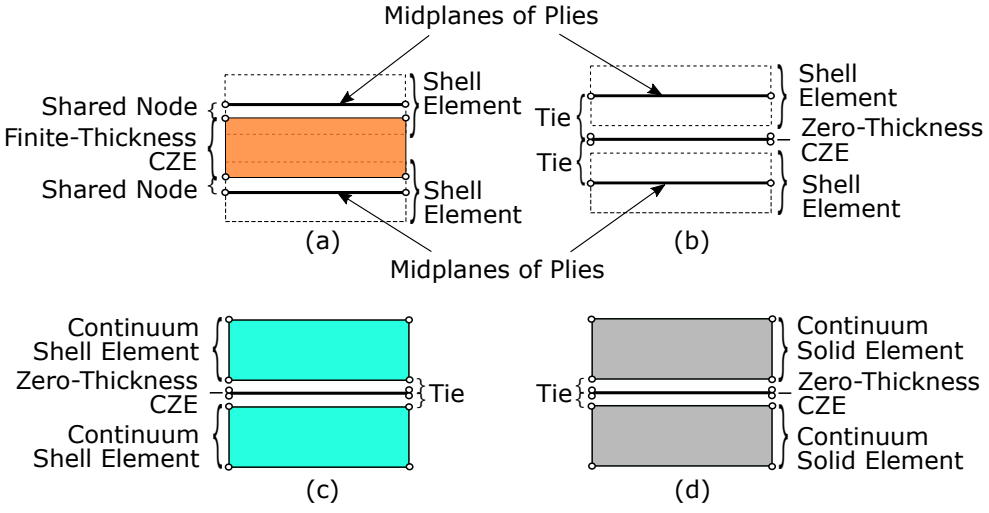

Figure 3.1: Exploded view of the sketch of coupling technique between one interface and the adjacent plies; finite thickness CZE with (a) shell elements, and zero thickness CZE with (b) shell, (c) continuum shell, and (d) continuum solid and continuum plane strain elements.

top and bottom ply thickness. The nodes at the midplanes of the shell elements are shared with the nodes of the CZE. In this modeling strategy, the CZE thickness is equal to the adjacent ply thicknesses, i.e. half of the top and bottom ply thickness. Figure 3.1(b), Figure 3.1(c), and Figure 3.1(d) present the ply-level model based on shell, continuum shell, and continuum solid elements connected to zero geometrical thickness CZE by using surface-to-surface based tie constraints. They are denoted as SPLZ, CSPLZ, and CPLZ modeling strategies, respectively. Moreover, Figure 3.1(d) also represents the ply-level model based on two-dimensional continuum plane strain elements which are coupled to zero geometrical thickness of the CZE, denoted as CPEZ.

3.3 Aplication examples

DCB, ENF, and SLB simulations are performed to investigate the mode I, mode II, and mixed mode delaminations, respectively. The modeled laminates comprise eight plies where the CZEs connect all adjacent plies. Four different ply-level models as mentioned in section 3.2 are realized. All FEM computations are conducted using Abaqus/Standard 2020 [33] where an implicit solution scheme is applied to account for geometrically nonlinear behavior and progressive damage and failure of the interfaces. All considerations are limited to the elastic response of the plies.

3.3.1 Geometrical modeling

The geometrical modeling of the double cantilever beam (DCB), end-notch flexure (ENF), and single-leg bending (SLB) set-ups is shown in Figure 3.2. The laminated composites are made up of eight plies, with CZEs connecting all adjacent plies. They are modeled with a total thickness, $h = 2.53$ mm for all test set-ups. Every ply has 949 elements where each element has a length of l_x, l_y, and l_z are 0.158125 mm, 1.0 mm, and 0.31625 mm, respectively. Furthermore, fully integrated and linearly interpolated elements are employed for the SPLF, SPLZ, CPLZ, and CPEZ configurations whereas reduced integrated linear elements are used for CSPLZ configuration. The mesh around the initial delamination

is visualized in Figure 3.3. The normal direction of the orientation of the plies is in the positive z-direction for all 3D configurations and in the positive y-direction for CPEZ. As shown in Figure 3.2, the initial delamination, a, for the ENF and SLB are set to be greater than for the DCB and should be at least 0.7 times the length L to maintain the stability of the delamination growth [27, 37]. Plane strain boundary conditions in y-direction, i.e. $\varepsilon_y = \gamma_{xy} = \gamma_{yz} = 0$, are imposed to mimic the situation in a structure sufficiently apart from free edges. Additionally, as large deformations are being considered in the simulation, geometric nonlinear analyses are carried out. For all setups, a total displacement of 20 mm is used at a rate of 0.005 mm/s.

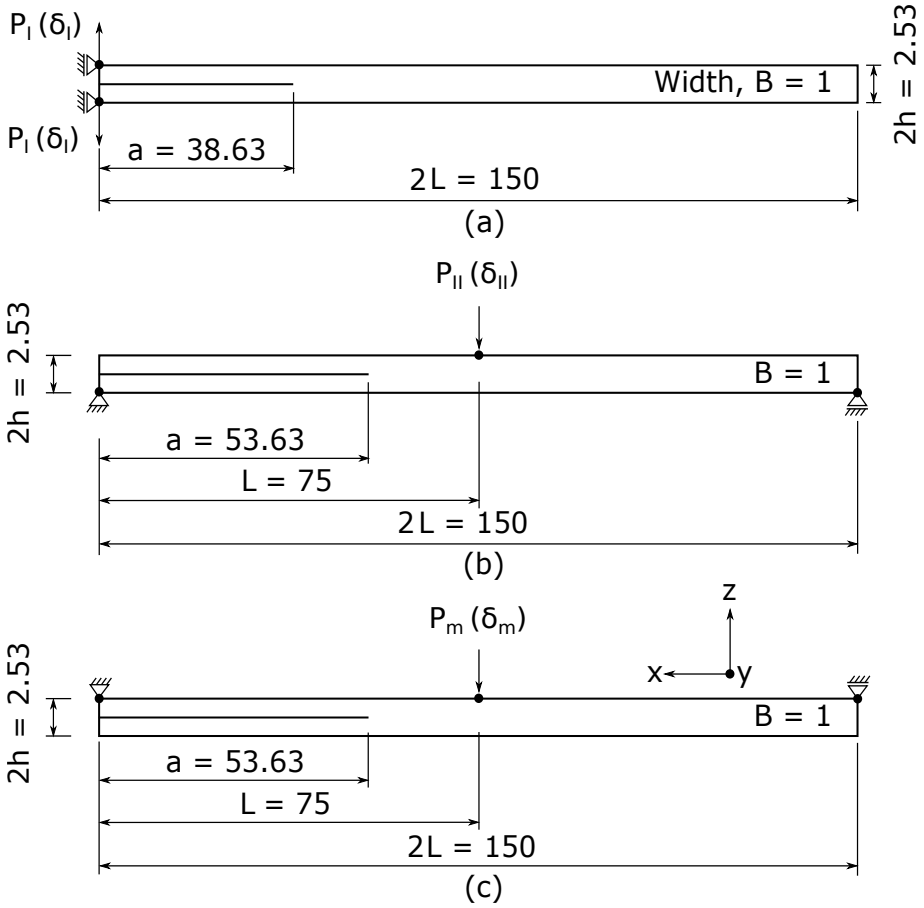

Figure 3.2: The overall dimensions (in mm), boundary conditions, and loading scenario used in (a) the DCB, (b) the ENF, and (c) the SLB simulations

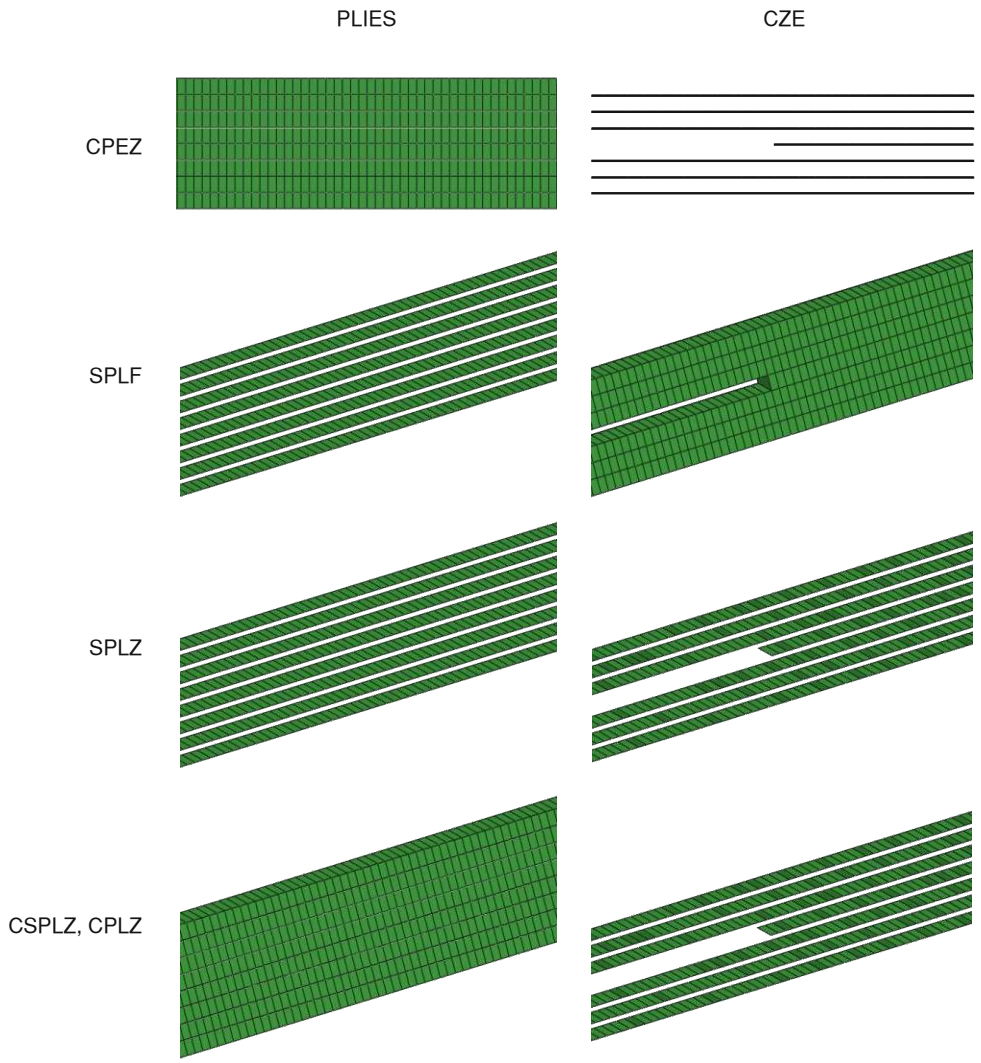

Figure 3.3: The mesh visualization of the plies and CZEs around the initial delamination for different ply-level models.

3.3.2 Material properties

The properties of the plies in Table 3.1 are obtained from [42, 93]. Damage initiation of the CZEs is expected to occur when a quadratic interaction function with nominal stress ratios reaches a value of one [33]. The constitutive response of the CZEs is defined using the Abaqus built-in bi-linear traction separation law [33]. Damage initiation of the CZEs is predicted by employing a quadratic nominal stress criterion defined by,

Table 3.1: Ply properties of homogenized carbon/epoxy 2×2 twill weave composite material which E, G, and ν being Young's modulus, shear modulus, and Poisson's ratio, respectively.

from [42]	*from [93]
$E_x = E_y = 56589.32$ (N/mm^2)	$E_z = 10066$ (N/mm^2)
$G_{xy} = G_{xz} = G_{yz} = 4185.86$ (N/mm^2)	
$\nu_{xy} = 0.045$	$\nu_{xz} = \nu_{yz} = 0.33$

* only apply to CPLZ and CPEZ

$$\left\{\frac{\langle t_n \rangle}{t_n^0}\right\}^2 + \left\{\frac{t_s}{t_s^0}\right\}^2 \geq 1 \tag{3.1}$$

where, t_i are the normal, n, and shear, s, component of the traction vector and t_i^0 are the corresponding interlaminar strengths. Delamination damage starts when the result of this equation is larger than or equal to one. Damage evolution is modeled based on the critical energy release rates in combination with a linear softening law. The Benzeggagh and Kenane (BK) criterion is used to treat the mixed mode behavior [17]. The BK law model gives the critical energy release rate as in Equation 2.16. In this study, the mixed mode parameter, $\eta = 1.75$ is selected [25]. The interface properties in Table 3.2 define the initial stiffnesses, K, together with inter-laminar strengths, t [28] and the critical energy release rates, $\mathcal{G}_{iC}$ [46].

Table 3.2: The interface properties defining the initial stiffness together with damage initiation [28] and propagation parameters [46]

Mode I	Mode II
$K_n = 10^5$ (N/mm^3)	$K_s = 10^5$ (N/mm^3)
$t_n^0 = 60$ (N/mm^2)	$t_s^0 = 79.289$ (N/mm^2)
$\mathcal{G}_{IC} = 0.9$ (N/mm)	$\mathcal{G}_{IIC} = 2.0$ (N/mm)

3.3.3 Contact modeling

The contact constraints within the ENF and SLB simulation are enforced using the surface-to-surface contact algorithm of Abaqus/Standard, which utilizes a frictionless contact definition to prevent inter-ply penetration in regions of delamination. A hard contact penalty algorithm is also applied which the penalty stiffness value is 42.5 % less than the representative underlying element stiffness. Additionally, viscous regularization with a 10^{-4} s relaxation time and adaptive automatic stabilization are utilized to improve the convergence of the simulations. The default value of 2.0×10^{-4} is chosen for the dissipated energy fraction, and the accuracy tolerance of 0.05 is utilized for the automatic damping algorithm [33].

3.4 Results and discussion

The following results are solely obtained by means of numerical simulations. All simulations are conducted using a standard PC workstation with eight 2.35 – 3.35 GHz CPUs. The load-displacement curve, the delamination area at the maximum load and maximum displacement, and the mode-mixity of each individual model are evaluated. Finally, the computation time of each individual model is accessed.

3.4.1 Load-Displacement Curve

Figure 3.4 - 3.6 illustrates the load-displacement predictions of the DCB, ENF, and SLB simulations, respectively. In general, the load-displacement curves of all simulation setups correspond very well with the CBT results. The predicted pre-peak stiffness and the maximum load of the SPLF for the DCB simulations are slightly higher than for the other models. The higher stiffness is mainly generated by the finite thickness of the CZEs and the high stiffness assigned to the CZEs. The CSPLZ is the only one having a different delamination behavior for the ENF load-displacement results. After the maximum load is reached, the delamination does not propagate immediately. The maximum load, on the

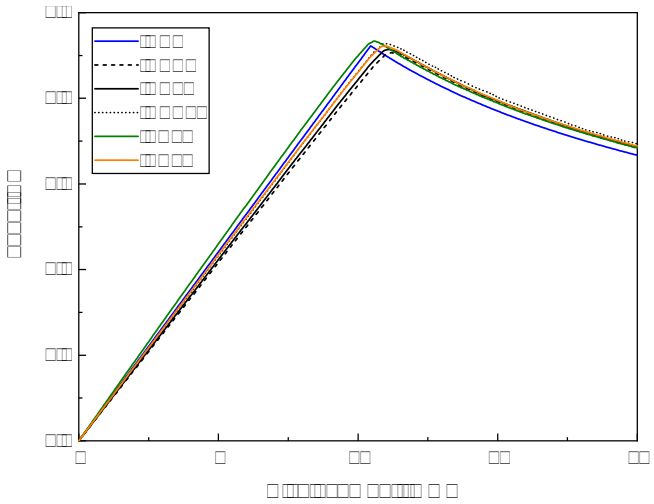

Figure 3.4: Load-displacement curve of DCB simulations for different ply-level models.

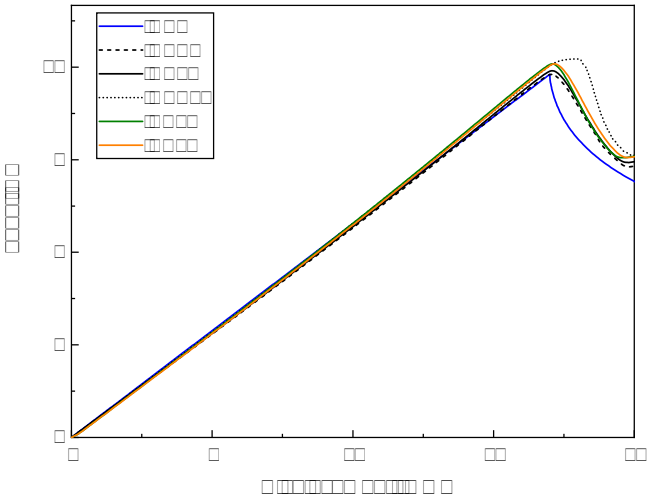

Figure 3.5: Load-displacement curve of ENF simulations for different ply-level models.

other hand, is comparable to the other models. For the SLB simulations result, all models can accurately predict the delamination behavior in laminated composites under mixed mode loading conditions. The load decreases when the delamination starts to propagate and then increases when the displacement reaches 17.5 mm. This increase in load occurs when the delamination reaches the load point. The delamination beyond the load point propagates more slowly and is dominated by mode II delamination.

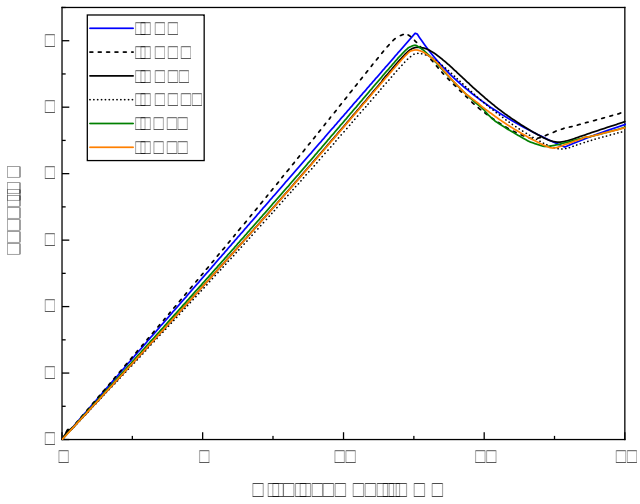

Figure 3.6: Load-displacement curve of SLB simulations for different ply-level models.

3.4.2 Delamination Area and Computation Time

Figure 3.7 presents the process zones and delamination areas of different ply-level models which is represented by the stiffness degradation (SDEG) distribution on the CZEs in front of the initial delamination. Figure 3.7(a) presents the process zones at the maximum load, just before the delamination begins to propagate. To ensure the accuracy of the modeling of delamination propagation, the process zone near the delamination tip must be well resolved. Falk et al. [39] demonstrated that four to ten elements inside the process zones are adequate to predict the propagation of delamination. The number of elements in the process zones for the proposed ply-level models ranges between seven and nine elements. Figure 3.7(b) shows the process zones at the maximum displacement as well as the delamination areas (shown in light grey regions). The light grey elements represent the fully damaged of CZEs that reach an SDEG value of 0.9999. Figure 3.7(c) highlights the SDEG of the SPLF model at maximum load and maximum displacement along the x-axis.

The delamination areas of all models for the DCB, ENF, and SLB simulations exhibit very good agreement with the results for the entire delamination process. The state at the end of the loading event is reported in Table 3.3. The SPLF predicts a slightly larger delamination area than the other configurations in the context of DCB simulations. As

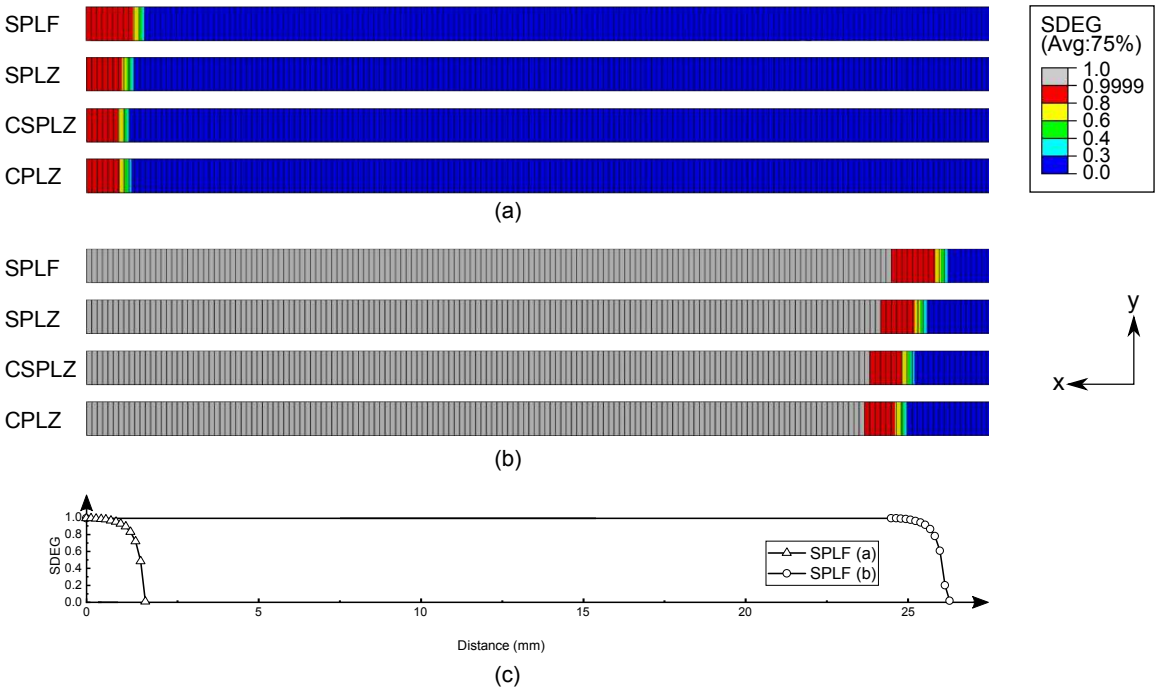

Figure 3.7: Process zones and delamination areas of the SLB simulations at (a) the maximum load and (b) the end of the loading event. (c) shows the SDEG of the SPLF model at (a) and at (b) along x-direction.

Table 3.3: The delamination area (mm^2) of DCB, ENF, and SLB simulations for different ply-level models at the maximum displacement of 20 mm.

Ply-Level Models	DCB	ENF	SLB
CBT	15.38	20.10	22.95
CPEZ	14.21	20.10	24.38
SPLF	15.47	20.10	23.90
SPLZ	14.68	20.10	23.59
CSPLZ	14.68	20.74	23.43
CPLZ	14.37	20.10	23.11

illustrated in Figure 3.4, the pre-peak stiffness of the SPLF model is slightly higher than other models, but delamination begins to propagate at a smaller applied displacement. This causes the differences in the delamination area. Differently, the SPLF and SPLZ models are remarkably similar to those of the CPLZ reference model in the ENF and SLB simulations.

Table 3.4: The computation time (s) of DCB, ENF, and SLB simulations for different ply-level models when the maximum displacement reaches 20 mm.

Ply-Level Models	DCB	ENF	SLB
CBT	-	-	-
CPEZ	425	509	1209
SPLF	636	599	1812
SPLZ	739	943	2803
CSPLZ	1172	1658	3046
CPLZ	1015	988	4337

In terms of computational time, the model employing 3D continuum elements takes substantially longer to compute than the shell element based ply-level models, as listed in Table 3.4. This phenomenon shows that the shell element-based ply-level models' system of equations is solved more efficiently than the continuum one. The computation time of the SPLZ model is slightly larger than those of the SPLF model although it uses the same conventional shell elements. This is due to the various coupling strategies used between the plies and CZE, as stated in Section 3.2. The results show that the SPLF model can be very beneficial in terms of computation time when applied to large-scale laminated composite components. Even better than for the DCB case, the SPLF model for the ENF case provides a very good trade off between reliable results and computational economics with a computation time of roughly 10 minutes. The SPLF model has a computation time that is 36% lower than that of the SPLZ model. Again, the SPLF model remains the best one when compared to other models for SLB case. Furthermore, it is noted that one continuum element per ply thickness is considered to have lower accuracy compared to a shell element.

3.4.3 Mode-Mixity

Figure 3.8 shows the mode-mixity during delamination propagation from the initial delamination tip to the load point which is collected at the centroid of the element at the maximum displacement. The mode-mixity at the early transition phase is suddenly increased. This phenomenon occurs until 2 mm distance when the process zone is completely formed (see

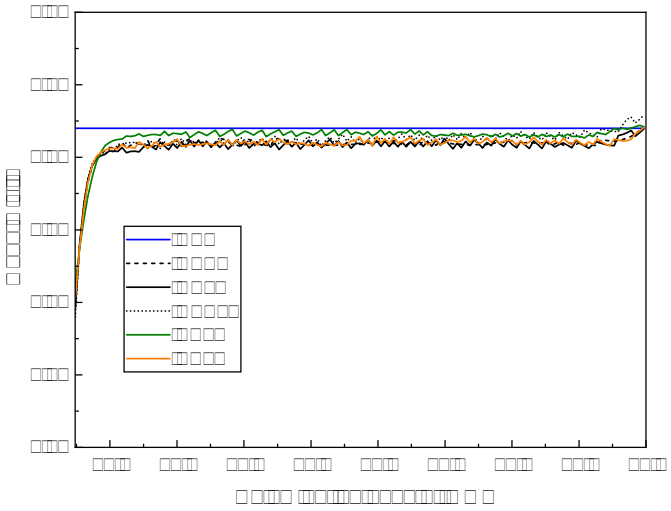

Figure 3.8: The mode-mixity during delamination propagation of the SLB simulations set-up.

Figure 3.7(a)). Afterward, the mode-mixity tends to be constant until the delamination reaches the load point. Generally, the mode-mixity of all ply-level based models are similar and provide close agreement with corrected beam theory results of 0.42. It should be highlighted that the mode-mixity value at around 0.42 shows that the SLB tests lead to mixed mode evolution in the interface.

3.5 Summary

A simulation technique based on cohesive zone elements is presented for evaluating progressive delamination in multilayered laminated composites by means of the Finite Element Method. Four different 3D and one 2D ply-level modeling strategies are examined and compared in terms of delamination behavior such as load-displacement curves, delamination area, computation time, and mode-mixity during delamination propagation. Mode I, mode II, and mixed mode delamination are investigated using a double cantilever beam, end notch flexure, and single leg bending set-ups, respectively. All proposed models produce reliable findings when compared to analytical results used as references. The results show that the ply-level approach based on shell elements in combination with finite thickness co-

hesive zone elements is the most favorable one in terms of the accuracy of the result as well as computational efficiency. The model can also accurately predict mixed mode behavior.

Chapter 4

Transverse shear behavior

4.1 Introduction

To get the basic understanding and comparison between ply-level models such as shell-based ply level in combination with the finite geometrical thickness of CZE (SPLF), continuum shell-based ply level connected to zero geometrical thickness CZE (CSPLZ), and continuum ply level connected to zero geometrical thickness CZE (CPLZ) models, extended research is carried out in the contexts of deformation, transverse shear stress, and normal bending stress. Analytical solutions and two-dimensional (2D) continuum plain strain model (CPE) without CZE are mainly calculated as reference results. One strip layered isotropic material with plane strain condition is introduced for all configurations to investigate the transverse shear and deformation behavior and provide high computational efficiency. The strip model was chosen in order to simplify the laminate geometry which usually has two large dimensions compared to their thickness. In the present study, a strip model of the beam is utilized under distributed loading as shown in Figure 4.1.

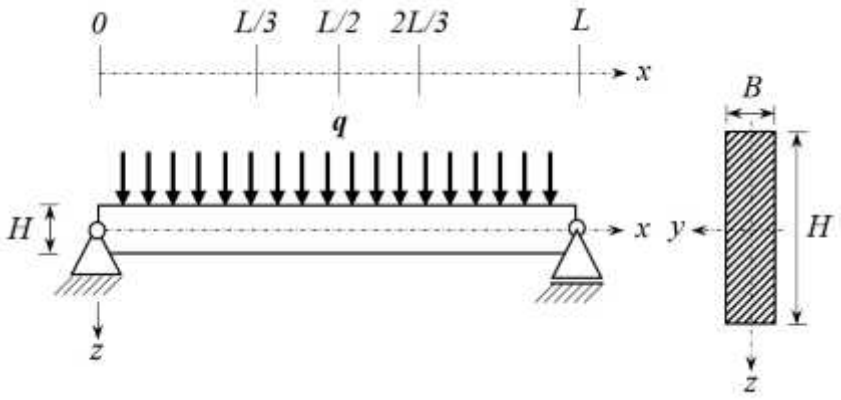

Figure 4.1: Geometry, boundary, and loading conditions for the strip model of beam.

4.2 Analytical solutions

Two analytical solutions are used as reference solutions i.e. Euler-Bernoulli and Timoshenko beam solutions. For simplification, the analytical solution is denoted by AN while Euler-Bernoulli and Timoshenko beam solutions are denoted by EB and T, respectively. Four parameters including deflection in the z-direction, transverse shear stress along the neutral axis, transverse shear stress at $x = L/3$ and $x = 2L/3$ along the z-direction, and normal bending stress at $x = L/3$ and $x = 2L/3$ along the z-direction of the beam are investigated by using these beam solutions. The deflection in the z-direction, δ_z is calculated by using Equation (4.1) and (4.2) for Euler-Bernoulli and Timoshenko solutions, respectively.

$$\delta_z = \frac{qx}{24\hat{E}I}(L^3 - 2Lx^2 + x^3) \tag{4.1}$$

$$\delta_z = \frac{qx^4}{24\hat{E}I} - \frac{qLx^3}{12\hat{E}I} + \frac{qL^3x}{24\hat{E}I} - \frac{qx^2}{2\kappa AG} + \frac{qLx}{2\kappa AG} \tag{4.2}$$

Where plane strain Young's moduli $\hat{E} = \dfrac{E}{1-\nu^2}$, shear coefficient $\kappa = \dfrac{10(1+\nu)}{12+11\nu}$ [29], and shear modulus $G = \dfrac{E}{2(1-\nu)}$. The transverse shear stress is only calculated by using the Timoshenko theory since the Euler-Bernoulli solution does not consider the shear deforma-

tion. The shear load $V_{(x)}$ is initially calculated along the neutral axis by using Equation (4.3). Moreover, the shear load is substituted to Equation (4.4) to obtain the transverse shear stress along the neutral axis.

$$V_{(x)} = q(\frac{L}{2} - x) \tag{4.3}$$

$$\tau_{(x,z)} = \frac{V_{(x)}Q_{(z)}}{IB_{(z)}} \tag{4.4}$$

Where $Q_{(z)}$ is the first moment of area, I is the area moment of area, and $B_{(z)}$ is section width. Since the transverse shear stress is defined in the neutral axis, it's mainly affected by shear load $V_{(x)}$ because $Q_{(z)}$, I, and $B_{(z)}$ remained constant. By using Equation (4.4), the transverse shear stress at $x = L/3$ and $x = 2L/3$ along z-direction can also be calculated. In this case, the value of transverse shear stress is mainly affected by the first moment of area $Q_{(z)}$. Moreover, the normal bending stress also calculated along the z-direction. To obtain the results, the bending moment should be defined first by using Equation (4.5) and then substitute to Equation (4.6).

$$M_{(x)} = \frac{qx}{2}(L - x) \tag{4.5}$$

$$\sigma_{(x,z)} = \frac{M_{(x)}z}{I} \tag{4.6}$$

Since the bending moment value at $x = L/3$ and $x = 2L/3$ are the same and I remains constant, so, the bending normal stress at two points is the same either.

4.3 Numerical procedures

All FEM simulations are conducted using Abaqus/Standard 2020 [33] where an implicit solution scheme is applied which is limited to the elastic response of the model. Three

different ply-level based modeling including SPLF, CPLZ, and CSPLZ are utilized by implementing a coupling technique between one interface and the adjacent plies as described in Section 3.2. To recall, the beam's cross-section of SPLF is discretized with the layers which are represented by their mid-planes. The number of layers is purposely made odd to ensure that the neutral axis of bending is exactly in the layer at the center of the laminate. Cohesive zone elements (CZEs) are utilized as interfaces between shell layers to obtain a transverse shear prediction. The CZEs share their nodes with the corresponding shell elements as illustrated in Figure 4.2. In this respect, the geometrical thickness of the CZEs is equal to the thickness of a single shell layer ($t_c = t_p$). Differently, the CPLZ and CSPLZ is discretized with the layers explicitly which are connected to zero thickness CZEs as shown in Figure 4.3. A two-dimensional continuum model is also performed as the reference result. The element type of 4-node continuum plane strain (CPE) with fully integration is used in this model within an element number of 600. In the CPE model, the CZEs are not employed.

The boundary condition, geometry, and loading scenario of the strip model of beam is presented in Figure 4.1. The boundary conditions are applied in the neutral axis of bending to mimic the conditions of the corresponding analytical problem. Differently, the boundary condition of the CSPLZ and CPLZ models are applied for the whole nodes at $x = 0$ and $x = \mathrm{L}$. Since the model is only one strip, additional boundary conditions are applied to

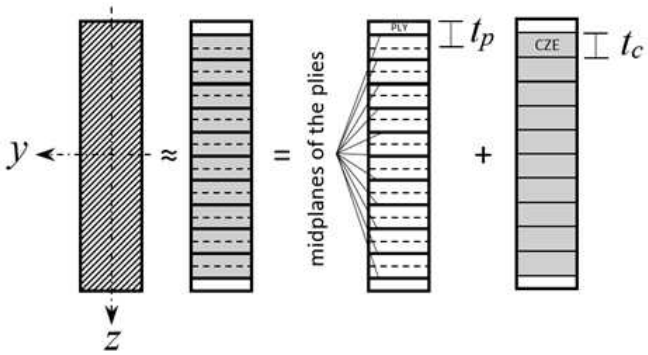

Figure 4.2: Representation of the rectangular cross of the beam by a combination of standard shell layer and cohesive zone element (CZE) in between.

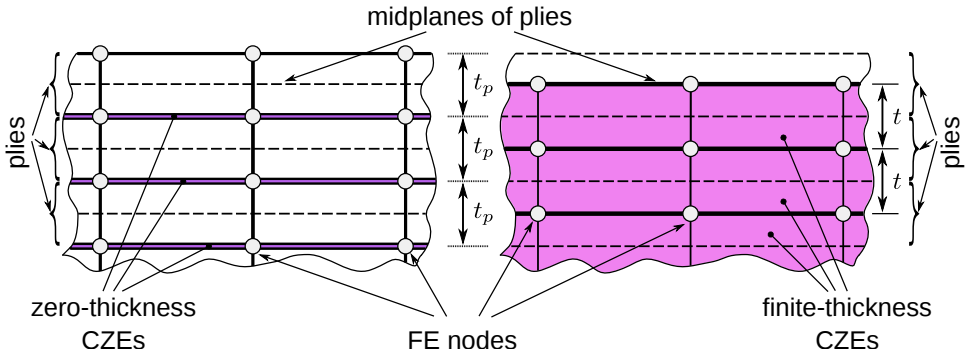

Figure 4.3: Finite-thickness and zero-thickness CZEs representations of the ply-level models.

implement the plane strain conditions that applied for all nodes of the models of $u_y = \theta_x = \theta_z = 0$. The beam is simply supported and subjected to a distributed surface load $q = 25$ N/mm. In this study, eleven numbers of layers are used where each layer has a thickness of 5 mm. Generally, the rectangular beam are employed which the cross-section dimensions are $H = 55$ mm and $B = 5$ mm with a length $L = 300$ mm.

The material behavior of the rectangular beam is defined as isotropic and linear elastic with Young's modulus $E = 70{,}000$ MPa, Poisson's ratio $\nu = 0.33$, and shear modulus $G = 26{,}315.79$ MPa. Two different elastic properties of CZEs is defined to investigate the influence of the CZEs on the simulated structural behavior. The first, the CZEs are defined as infinitely stiffed material with K_{n}=K_{s}=K_{t}=10^{11} MPa. In the second configuration, the CZEs are defined as infinitely stiffed $K_{\mathrm{n}} = 10^{11}$ MPa with a combination of K_{s}=K_{t}=G to study the influence of the out-of-plane properties of the CZEs on the predicted transverse shear response of the structure. Both configurations name as PLY LEVEL BASED MODEL-EB and PLY LEVEL BASED MODEL-T, respectively.

4.4 Results and discussion

4.4.1 SPLF model

Figure 4.4 presents the deflection in the z-direction of the SPLF models compared with results obtained from analytical solutions and a CPE Finite Element model by implementing plane strain conditions. Focus on the analytical solutions, the maximum deflections of Euler-Bernoulli and Timoshenko solutions are -0.4842 mm and -0.5299 mm, respectively. The Timoshenko solution is more compliant than the Euler-Bernoulli solution due to the shear deformation effects. The deflection in z-direction of the 2D continuum model is close to the Timoshenko solution. This phenomenon shows that shear deformation has already considered in continuum models. Figure 4.4 also represents the deflection results of the SPLF models compared with reference results obtained with analytical solutions and a CPE model. In respect to the deflection in the z-direction, the SPLF-EB has a very good agreement with analytical Euler-Bernoulli solutions while the SPLF-T has a very good agreement with analytical Timoshenko solutions.

Figure 4.5 illustrates that the analytical transverse shear stress result is linearly distributed from $x = 0$ to $x = L$. It can be seen that in terms of transverse shear stress distribution

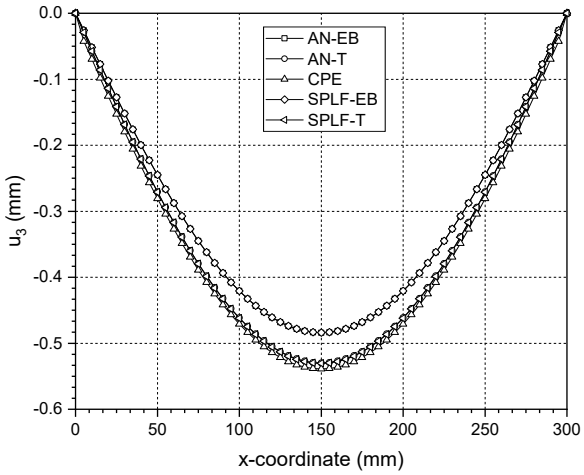

Figure 4.4: Deflection in z-direction of the SPLF models compared to the reference solutions.

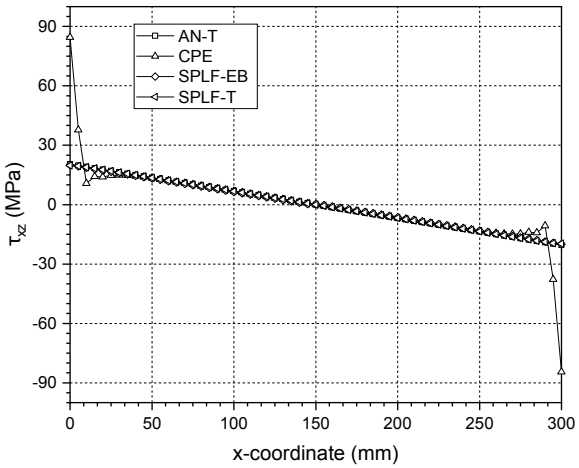

Figure 4.5: Transverse shear stress distribution along the neutal axis of the SPLF models compared to the reference solutions.

along the neutral axis, the SPLF model provides a very good agreement with the reference solutions either. However, a deviation near supports can be observed in CPE model.

Figures 4.6 and 4.7 illustrates the transverse shear stress and normal bending stress result of the SPLF models in z-direction is distributed at $x = L/3$ and $x = 2L/3$, respectively. Again, both transverse shear stress and bending normal stress provides a very good agreement with the reference solutions. It can be summarized that the transverse shear stress in SPLF

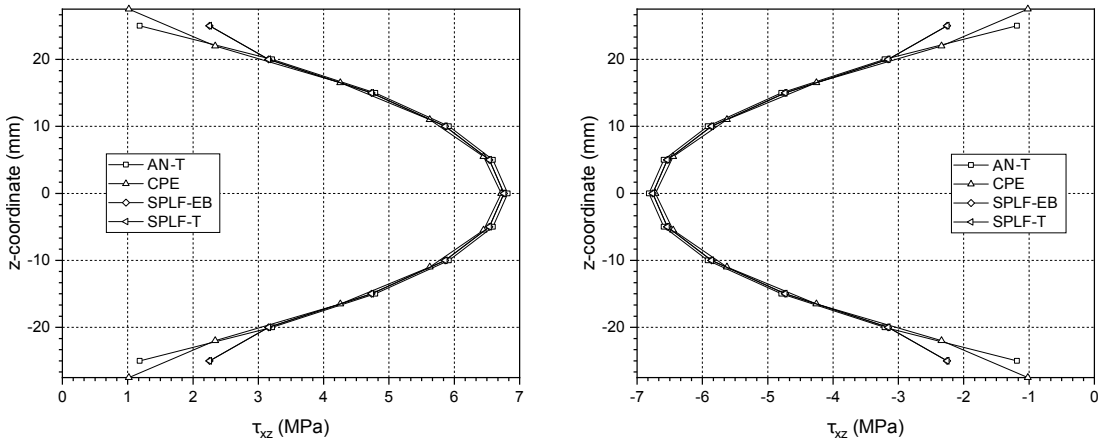

Figure 4.6: Transverse shear stress distribution of the SPLF models in z-direction at (a) $x = L/3$ and (b) $x = 2L/3$ compared to the reference solutions.

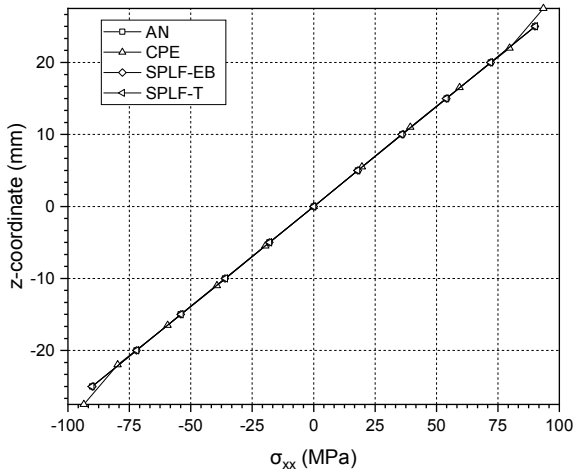

Figure 4.7: Bending normal stress rdistribution in z-direction at $x = L/3$ and $x = 2L/3$ of the SPLF models compared to the reference solutions.

models is mainly transferred by the CZEs. The stiffness properties of the CZEs have a strong influence on the deflections and the transverse shear stresses.

4.4.2 Ply-level based comparison

Figure 4.8 shows the deflection in z-direction of SPLF compare to CSPLZ and CPLZ models along the neutral axis. It is clearly seen that the deflection of CSPLZ-EB and CPLZ-EB

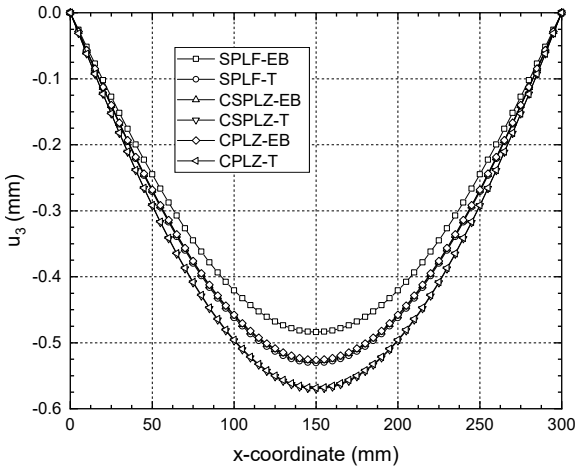

Figure 4.8: Deflection results comparison between SPLF, CSPLZ, and CPLZ models for different CZEs stiffness definition.

is in good agreement with SPLF-T. In other words, the shear deformation has already considered in CSPLZ-EB and CPLZ-EB models. Moreover, CSPLZ-T and CPLZ-T are physically not correct because they are more compliant than the reference results and seem to have double shear deformation.

Figure 4.9 presents the transverse shear stress results of the SPLF models compared with CSPLZ and CPLZ models. It can be seen that the transverse shear stress is correctly captured for all models. All of the transverse shear stress values are captured in CZE nodes since finite element analysis (FEA) does not consider the transverse shear stress in SPLF and CSPLZ. Additionally, the different geometrical thickness of CZEs does not affect the transverse shear stress for all models.

Transverse shear stress results of the SPLF models compared with CSPLZ and CPLZ models at $x = L/3$ and $x = 2L/3$ are shown in Figure 4.10. The transverse shear stress of the CSPLZ and CPLZ models are in very good agreement with the transverse shear stress of the SPLF model. It can be summarized that the transverse shear stress is mainly transferred by the CZEs with two different geometrical thicknesses.

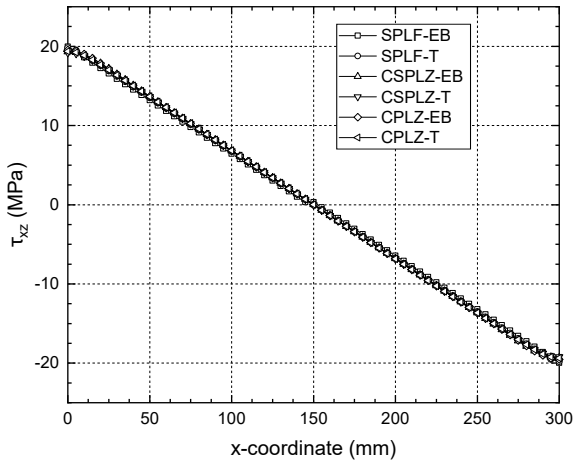

Figure 4.9: Transverse shear stress results of the SPLF models compared with CSPLZ and CPLZ models by implementing plane strain conditions.

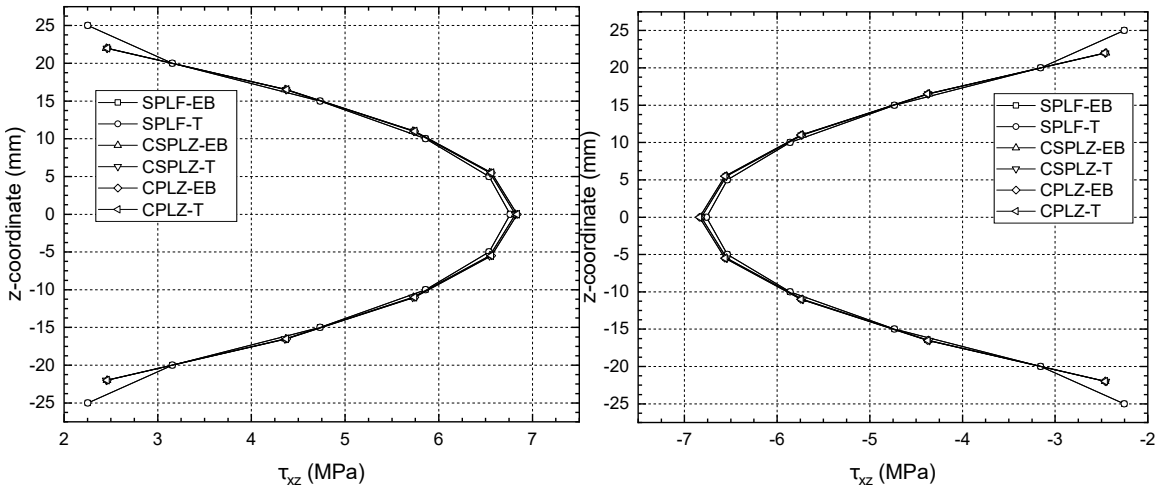

Figure 4.10: Transverse shear stress results of the SPL models compared with CSPL and CPL models by implementing plane strain conditions at (a) $x = L/3$ and (b) $x = 2L/3$

4.4.3 Modification of out-of-plane shear modulus

Recall from the analysis of Figure 4.8, it is explained that the plies of CPLZ and CSPLZ have been considered the shear deformation behavior. Therefore, further investigation is required on the effect of shear modulus on the deflection of the beam. In this case, the plies will be defined as orthotropic elastic where the Equation (4.7) is performed [33]. Within Equation (4.7), modification of out-of-plane shear modulus G_{xz} and G_{yz} can be carried out to investigate the shear deformation behavior while the CZEs properties are the same as the previous definition. The modification is done by multiplying the out-of-plane shear modulus G_{xz} and G_{yz} by factor of five and 10^1 to 10^{11}.

$$\begin{Bmatrix} \varepsilon_{\mathrm{x}} \\ \varepsilon_{\mathrm{y}} \\ \varepsilon_{\mathrm{z}} \\ \gamma_{\mathrm{xy}} \\ \gamma_{\mathrm{xz}} \\ \gamma_{\mathrm{yz}} \end{Bmatrix} = \begin{bmatrix} \frac{1}{E_{\mathrm{x}}} & \frac{-\nu_{\mathrm{yx}}}{E_{\mathrm{y}}} & \frac{-\nu_{\mathrm{zx}}}{E_{\mathrm{z}}} & 0 & 0 & 0 \\ \frac{-\nu_{\mathrm{xy}}}{E_{\mathrm{x}}} & \frac{1}{E_{\mathrm{y}}} & \frac{-\nu_{\mathrm{zy}}}{E_{\mathrm{z}}} & 0 & 0 & 0 \\ \frac{-\nu_{\mathrm{xz}}}{E_{\mathrm{x}}} & \frac{-\nu_{\mathrm{yz}}}{E_{\mathrm{y}}} & \frac{1}{E_{\mathrm{z}}} & 0 & 0 & 0 \\ 0 & 0 & 0 & \frac{1}{G_{\mathrm{xy}}} & 0 & 0 \\ 0 & 0 & 0 & 0 & \frac{1}{G_{\mathrm{xz}}} & 0 \\ 0 & 0 & 0 & 0 & 0 & \frac{1}{G_{\mathrm{yz}}} \end{bmatrix} \begin{Bmatrix} \sigma_{\mathrm{x}} \\ \sigma_{\mathrm{y}} \\ \sigma_{\mathrm{z}} \\ \tau_{\mathrm{xy}} \\ \tau_{\mathrm{xz}} \\ \tau_{\mathrm{yz}} \end{Bmatrix} \tag{4.7}$$

Figure 4.11 illustrates the maximum deflection in z-direction comparison between SPLF, CSPLZ, and CPLZ by implementing the out-of-plane shear modulus modification. It can be seen that the maximum deflection of SPLF is not affected by modifying the G_{xz} and G_{yz}. This phenomenon occurs due to the shell element thickness is not geometrically defined. For the CSPLZ model, the maximum deflection is reduced by increasing G_{xz} and G_{yz} until a hundred times of G_{xy} and remained constant if G_{xz} and G_{yz} increased more than that. It means that with G_{xz} and G_{yz} is hundred times G_{xy} can be categorized as infinitely stiff material for continuum shell element. Different from SPLF and CSPLZ, the maximum deflection of the CPLZ model will lead to zero deflection. This phenomenon occurs due to

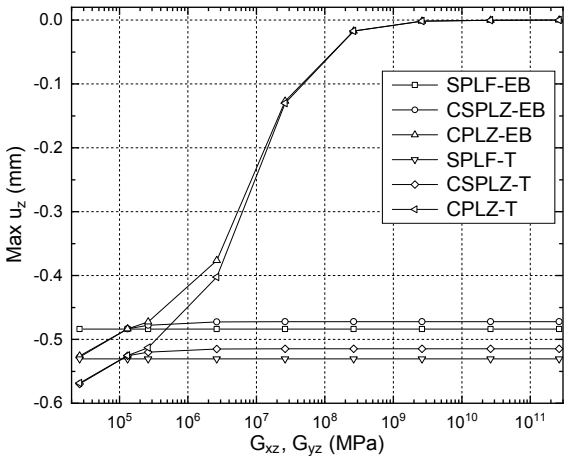

Figure 4.11: Maximum deflection in z-direction comparison between SPLF, CSPLZ, and CPLZ models for various $G_{\mathrm{xz}} = G_{\mathrm{yz}}$ by implementing orthotropic elasticity definition and plane strain conditions.

shear locking that exists in the element of the plies. However, as mentioned in the previous section, the maximum deflection of CSPLZ and CPLZ models will be close to the SPLF results if the G_{xz} and G_{yz} are increased by a factor of five or equal to t_p. It means that even though the shear flexibility of the CPLZ and CSPLZ have already considered but the modification of the G_{xz} and G_{yz} can be utilized to reduce their shear flexibility.

4.5 Summary

In this chapter, a study of transverse shear behavior of homogeneous plane strain isotropic beam is done for different ply-level based modeling strategy. From numerical predictions, it can be conclude that the SPLF model provides a very good agreement to the analytical solutions and two dimensional plane strain model in terms of deflection, transverse shear stress, and normal bending stress. The shear deformation has already considered in CSPLZ and CPLZ models. Consequently, the reduction of out-of plane stiffness of cohesive zone element will lead to physically not correct model because they are more compliant than the reference results and seem to have double shear deformation. Finally, the modification of $G_{xz} = G_{yz}$ by implementing the orthotropic elasticity of CSPLZ and CPLZ models can be used to mimic the reference solutions.

Chapter 5

Low Velocity Impact in Laminated Composites

5.1 Introduction

Laminated composites are increasingly being used in the aircraft industry due to their outstanding mechanical characteristics such as high stiffness and strength to weight ratios which are important characteristics for lightweight design [4]. Furthermore, these materials have good fatigue performance, high corrosion resistivity, and are easily formed during manufacturing processes. Despite that, laminated composites are susceptible to impact damage due to the weak transverse load-carrying capacity [83]. Impact loading conditions on laminated composites can cause complex damage such as matrix cracking, fiber breakage, plasticity-like effects, and delamination [10, 40, 85, 86]. These damages have to be considered during design and maintenance of composite aircraft structures [84, 91, 106]. There, investigating the damage mechanisms of laminated composites under impact loading conditions is an important consideration in order to increase the impact resistance and the residual strength after impact of laminated composite structures.

The focus of this chapter is on the investigation of the failure and delamination behavior in laminated composites under LVI and CAI by performing a ply-level modeling strategy

based on conventional shell elements in combination with finite geometrical thickness of cohesive zone element (CZE) since it has been found efficient in [4]. Both LVI and CAI are simulated by using commercial FEM code Abaqus/Explicit 2020 (*Dassault Systèmes Simulia Corp., Providence, RI, USA*). Single and double LVI simulations are carried out on laminated composite plates. Three different impact distances between two impact positions are compared. For the LVI event, the impact energy is kept so low that the damage is dominated by delamination and no matrix cracking or fiber breaking occurs. CAI simulation is applied for all these impacted laminated composite plates, along with the unimpacted laminated composite plate to investigate the failure behavior and residual compressive strength of the laminated composites. The LVI and CAI simulations are done under ideal conditions and following ASTM standards D7136/D7136M and D7137/D7137M [8, 9]. The impact response, energy dissipation, and delamination area is examined. Furthermore, the structural integrity of the laminated composites is also examined in terms of stiffness degradation and compressive residual strength values. Finally, computation times are measured and compared with previous studies.

5.2 Modeling strategy

The modeling strategy is adopted from [4], performing the ply-level modeling based on conventional shell element together with finite geometrical thickness of CZE by the means of Finite Element Method (FEM). The CZEs share the nodes of the adjacent shell elements which are positioned at the corresponding midplanes of plies as shown in Figure 5.1. As a result, the thickness of the CZE is the same as the thickness of the corresponding plies. It has to be emphasized that despite their finite geometrical thickness, the CZEs mimic the mechanical behavior of a zero geometrical thickness interface because a traction-separation based constitutive law is applied [86].

Individual constitutive laws for plies and interfaces are employed to account for the appropriate damage and failure mechanisms such as intra- and inter-ply, respectively. Intra-ply damage and failure of the plies are accounted for tensile and compressive fiber damage

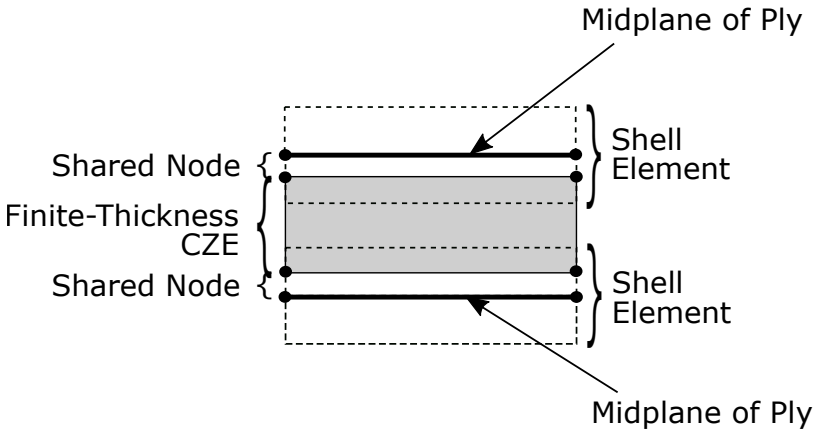

Figure 5.1: Exploded view of the coupling strategy between finite thickness of cohesive zone element and the adjacent shell elements [4].

as well as matrix cracking by an energy based continuum damage mechanics approach of the Hashin damage criterion [49]. Moreover, the damage is modeled under shear loading in order to replicate the matrix dominated shear response of the ply. It has to be noted that intra-ply damage and failure are mainly considered during CAI analysis since no matrix cracking or fiber breaking occurs during the LVI event due to the low impact energy. Inter-ply failure such as delamination is accounted for by cohesive zone elements using a bilinear traction-separation based constitutive law, cf. [25]. Damage initiation of the CZEs is predicted by employing a quadratic nominal stress criterion. Damage evolution is evaluated by using critical energy release rates in combination with a linear softening law. The Benzeggagh and Kenane (BK) criterion is used to treat the mixed mode behavior [17]. When the stiffness degradation of a CZE reaches a value of one at all integration points, it is considered as fully damaged and will be deleted for numerical reasons. Despite the fact that damage and failure mechanisms are taken into account in this investigation, the impact energy is kept as low as possible so that ply damage does not occur during the LVI event. Additionally, a contact definition between the plies needs to be employed to avoid overclosures in delamination zones [33] in which CZEs are deleted due to impact. This additional contact is enforced using the Abaqus/Explicit general contact by scaling the surface thickness of the plies by a factor of 0.8 which are utilized within the contact calculation.

5.3 Numerical procedures

The described modeling strategy is implemented to investigate the damage mechanism and failure behavior of the laminated composite under LVI and CAI events by using FEM package Abaqus/Explicit. The explicit time integration approach is used to examine the highly nonlinear impact response of the laminated composite plates. A schematic illustration of the modeled setup is presented in Figure 5.2 comprising (a) ply arrangement, (b) mesh visualization, (c) single LVI set up, (d) double LVI set up, and (e) CAI set up. Details will be provided in the following subsection.

5.3.1 Geometrical discretization

Figure 5.2(a) shows a sketch of the ply arrangement in the thickness direction. The laminate is modeled by applying the ply-level based modeling as described above. The laminates are composed of eight plies modeled by shell elements. The seven associated interfaces are modeled with finite thickness cohesive zone elements. Figure 5.2(b) shows the mesh visualization of the laminated composites as well as the spherical impactor. The ply element is a 4-nodal, linearly interpolated, and fully integrated conventional shell element. The integration in the thickness direction takes place via three integration points according to the Simpson rule. The normal direction of all shell layers points in the positive z-direction.

Laminated composites with the size of 150 mm $\times$ 100 mm are utilized according to ASTM standards. The LVI model uses an element size of 0.625 mm x 0.625 mm with an assigned thickness per ply of 0.5 mm. The element edges run parallel to the edges of the specimen panel. The plate area represented in gray regions in Figure 5.2(c-e) is equipped with an element size of 1.25 mm x 1.25 mm modeled with constant shell thickness. Since the cohesive zone elements use the same nodes and thus have the same element size. The mesh size of the impactor is about 0.5 mm x 0.5 mm on the spherical surface. Additionally, the volume of the sphere is filled with volume elements including eight-node brick and six-node wedge elements. Generally, the model consists of 561,435 elements with a total of 255,370 nodes and 1,448,580 degrees of freedom (DOF).

The impactor is modeled as quasi-rigid body since the impactor can be approximated as a rigid body in comparison to the laminates [70]. In terms of impactor facet, a sharp shape generally leads to an increased number of fiber defects and large penetration. On the other hand, a flat shape causes higher momentum transfer to the laminated composite and thus causes large-scale delamination. With respect to the size of the impactor, small foreign

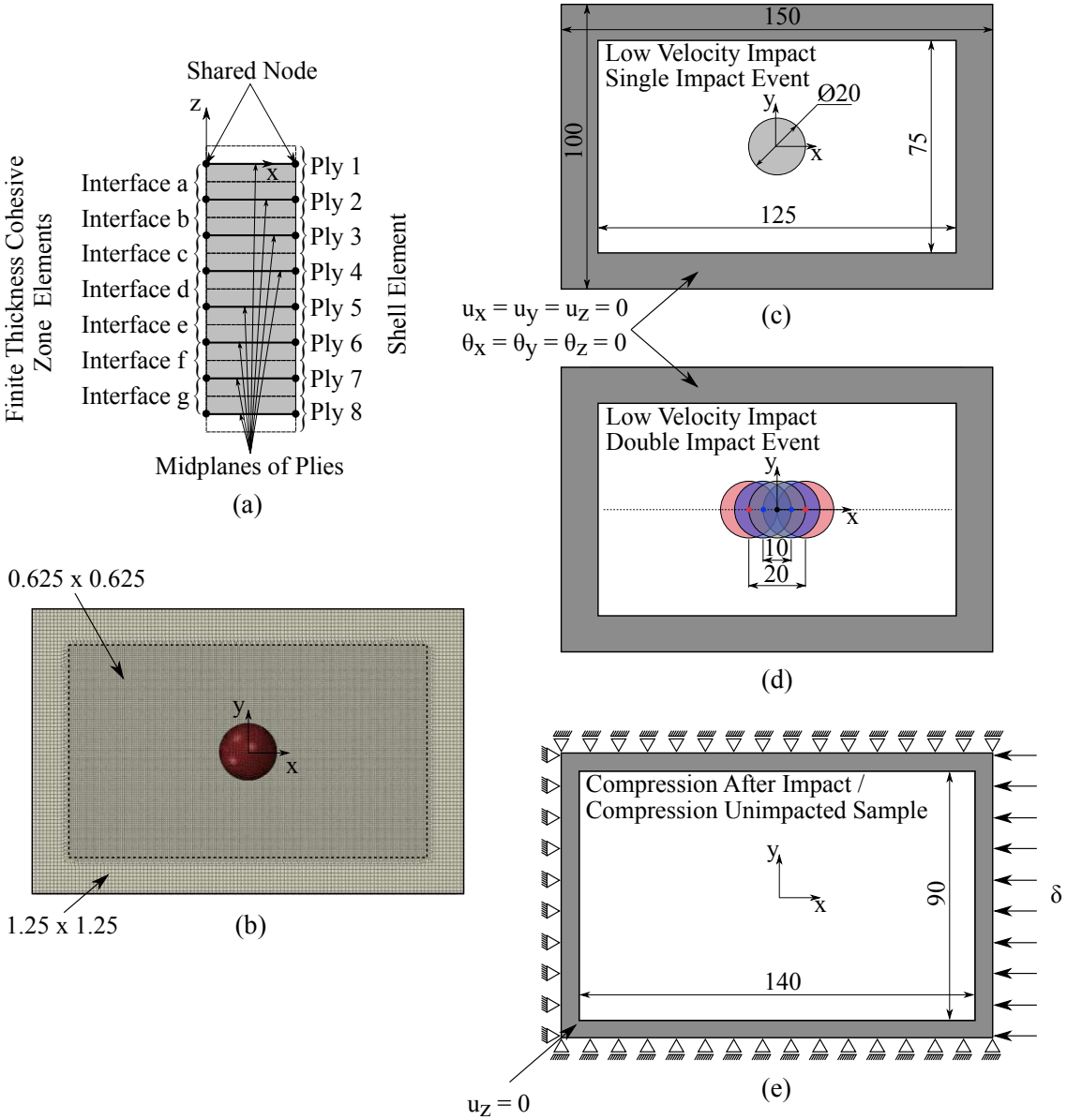

Figure 5.2: A schematic illustration of the modeled setup (dimensions in mm) including (a) ply arrangement, (b) mesh visualization, (c) single LVI set up, (d) double LVI set up, and (e) CAI set up

bodies induce localized damage and a high penetration depth, large foreign bodies cause deformation of the entire structure and, as a result, cause greater interface damage [1, 65]. With these two factors, a spherical impactor with a 20 mm diameter is chosen.

5.3.2 Boundary conditions

For the LVI simulation, a domain with a size of 125 mm × 75 mm × 4 mm is set as the impact site which is shown in the white region in Figure 5.2(c). At the grey region, all translational and rotational DOFs are fixed. This is a simplification of the jig in the experimental set up to mimic a fixed clamping on the circumference of the plate. The impactor movement is fixed for all DOFs except for translational movement along the z-direction. The load introduction to the laminate is modeled by defining contact between the impactor and the top surfaces of the top ply. It has to be noted, that frictionless behavior is assumed for every contact definition. The impact loading is performed with an initial velocity of 4 m/s and a mass of 0.25 kg. Consequently, the impact energy of 2 J is completely determined for all configurations. At the end of the simulation, there are still a few nodes directly at the impact point in a slight swinging motion as a vibration effect of the impact loading. For this reason, all node velocities are set to zero at the beginning of the second LVI simulation and/or CAI simulation. At this time, the first impactor is already in an upward motion and, therefore, has no influence on the subsequent second LVI and/or CAI simulations. Moreover, three different positions of the double impact event including 0 mm, ± 10 mm, and ± 20 mm from the center of the laminates can be seen in Figure 5.2(d).

For CAI simulation, new boundary conditions are now defined as illustrated in Figure 5.2(e). At the top and bottom of the plate, the displacements in the z-direction are fixed within a range of 5 mm on the circumference of the plate to mimic anti buckling guides. At the two edges of the long side of the plate, the displacement of all nodes of the individual layers in the y-direction and at the left edge in the x-direction are also fixed. Occurring frictional effects and contact conditions in the plate guides are not taken into account. The

displacement of 5 mm takes place at the right edge of the test plate with a displacement rate of 83.33 mm/s. For this purpose, all nodes of the individual layers are connected to a reference point via kinematic coupling constraint. The individual points thus carry out the same movement as the reference point. The two translational DOFs in y- and z-direction as well as all rotational DOFs of the reference point are fixed. Additionally, to ensure the stable time increment in the CAI model, a constant mass scaling factor of 10^4 is applied to the entire model.

5.3.3 Material properties

The total mass of the laminate is distributed between the plies and interfaces, where the mass density assigned to the top and bottom plies is 1.04 kg/m^3, the mass density assigned to the inner plies is 0.52 kg/m^3, and the mass density assigned to the cohesive zone element is 0.32 kg/m^3. Since the top and bottom plies are only connected to one interface, their

Table 5.1: Material properties of plies describing the elastic behavior, the longitudinal strength (X), transverse strength (Y), and the fracture toughness along fiber direction (x,y) for both tension and compression as well as transverse and in-plane shear strengths, S_{xy} and S_{xz}, respectively.

Properties			**Values**
Elastic properties	E_x	(GPa)	103.56
	$E_y = E_z$	(GPa)	10.066
	$\nu_{xy} = \nu_{xz}$		0.33
	ν_{yz}		0.2857
	$G_{xy} = G_{xz} = G_{yz}$	(GPa)	4.2058
Strength	X^+	(MPa)	1541.5
	X^-	(MPa)	1172.9
	Y^+	(MPa)	62.742
	Y^-	(MPa)	242.83
	$S_{xy} = S_{xz}$	(MPa)	115.83
Fracture toughness	$\mathcal{G}_{IC}^+$	(N/mm)	89.8
	$\mathcal{G}_{IC}^-$	(N/mm)	78.3
	$\mathcal{G}_{IIC}^+$	(N/mm)	0.2
	$\mathcal{G}_{IIC}^-$	(N/mm)	0.8

mass density is two times higher than the inner plies so that the mass of each individual ply is equally distributed. However, since Abaqus/Explicit uses lumped mass matrices, the nodal masses remain unchanged and the dynamic behavior of the laminate is retained [86]. The material properties defining the constitutive behavior of the plies are given in Table 5.1. Four different modes that characterize composite material damage are generally fiber breaking under tension, fiber buckling and kinking under compression, matrix cracking under tension and shear loads, and crushing of matrix under compression and shear [6]. However, in Abaqus, the damage initiation criteria for fiber reinforced composites are based on Hashin's theory which considers four different damage initiation mechanisms such as fiber tension, fiber compression, matrix tension, and matrix compression [49]. These material properties are taken from the work of Springer [93]

Table 5.2 lists the properties of the interface. To all cohesive zone elements, the same initial stiffness is assigned in normal, shear, and transverse direction of K_{n}, K_{s}, and K_{t} independent to the geometrical thickness. The inter-laminar strengths, t_{n}, t_{s}, and t_{t} are taken from [93]. The critical energy release rates, $\mathcal{G}_{\mathrm{I}}$, $\mathcal{G}_{\mathrm{II}}$, and $\mathcal{G}_{\mathrm{III}}$ are taken from values published in [46]. Additionally, for the impactor, the mass density of 59.7 kg/m^3 is defined to obtain a total impactor mass of 0.25 kg.

Table 5.2: The interface properties represented by cohesive zone element.

Property			**Values**
Elastic properties	$K_{\mathrm{n}} = K_{\mathrm{s}} = K_{\mathrm{t}}$	(N/mm^3)	1.0x10^6
Strength	t_{n}	(MPa)	60
	$t_{\mathrm{s}} = t_{\mathrm{t}}$	(MPa)	79.289
Fracture toughness	$\mathcal{G}_{\mathrm{I}}$	(N/mm)	0.133
	$\mathcal{G}_{\mathrm{II}} = \mathcal{G}_{\mathrm{III}}$	(N/mm)	0.46

5.4 Results and Discussion

The following results are solely obtained by means of numerical simulations. All simulations are carried out using a cluster computer system of eight standard PC workstations. Each PC workstation provides 6 CPUs and thus in total, 48 CPUs are employed at 3.3 GHz.

5.4.1 Low velocity impact

Figure 5.3 shows the impactor response including displacement, velocity magnitude, and contact force, as well as the displacement at the impact point of the top layer on the lami-

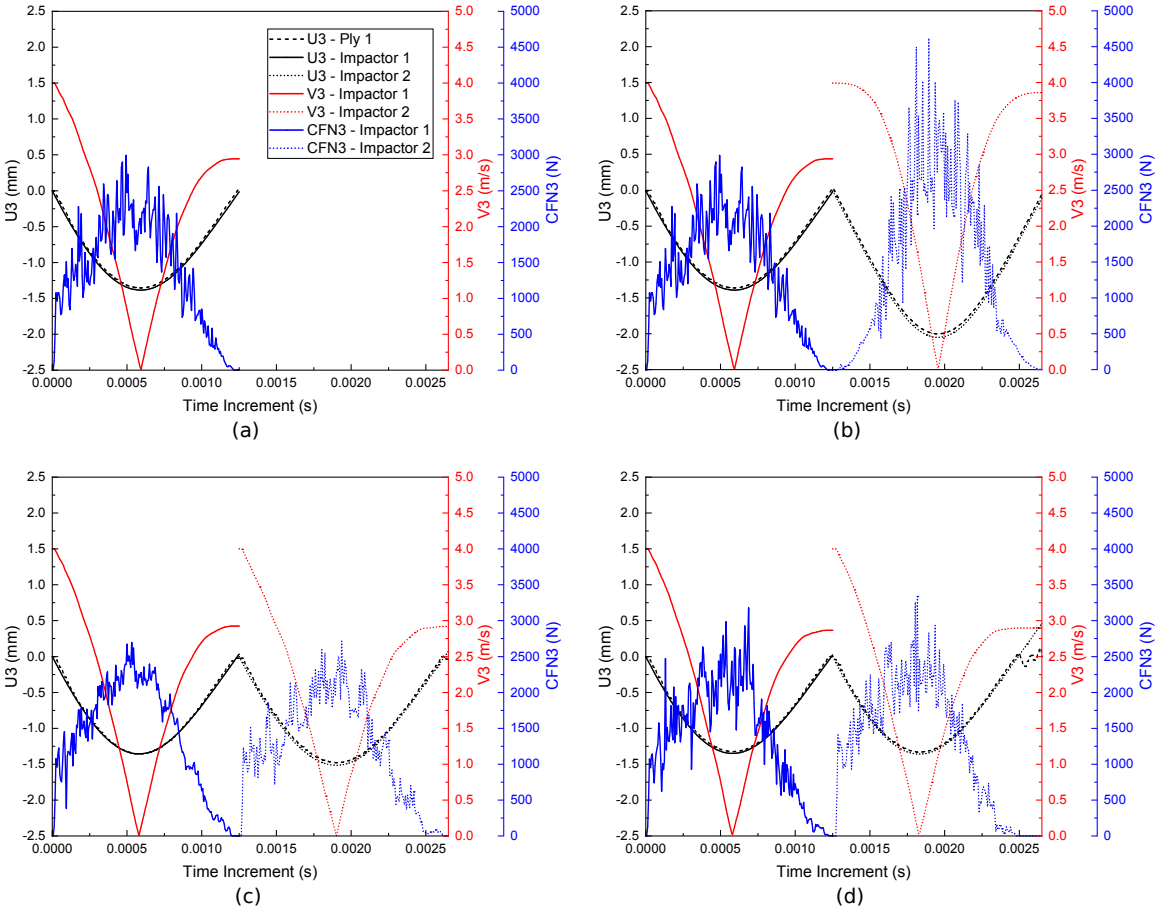

Figure 5.3: The impactor response including displacement (U3), velocity magnitude (V3), and contact force (CFN3), as well as the displacement at the impact point of the ply 1 (top layer) on the laminated composites for (a) single, (b) double with impactor distance of 0 mm, (c) 10 mm, and (d) 20 mm of LVI events.

nated composites for single and double 0 mm, 10 mm, and 20 mm of LVI events. The left and right curves represent the first impactor and second impactor, respectively. The black lines present the displacement of ply 1 (top layer), the first impactor, and the second impactor at the impact point shown as a dashed line, solid line, and dotted line, respectively. For the first LVI event, the top layer and the first impactor displacement are identical from the beginning until the impactor bounces back completely. This phenomenon demonstrates that no ply damage has occurred, implying that the ply stiffness does not significantly change while the delamination dominates the damage in laminated composites. In general, this phenomenon also occurs in the second LVI event. However, a slight fluctuation occurs in the double 20 mm case when the impactor is completely bounced back from the laminate. This fluctuation mainly occurs due to the vibration of the laminates after impact. Furthermore, the maximum displacement generated by the second impact event is significantly higher than the first impact event for the double 0 mm case because of the reduction in transverse shear stiffness due to delamination by the first impact. Additionally, the delamination due to the second impact is started to propagate when the displacement of the second impactor is higher than the maximum displacement of the first impactor.

The velocity magnitude of the first and second impactors is presented by the red lines, as shown in Figure 5.3. When the impactor collides with the laminate, its velocity drops until it approaches zero, which represents the lowest point or maximum displacement of the impactor. At this point, the kinetic energy of the impactor is zero, but the recoverable strain energy of the laminates is at its maximum. As a result, the recoverable strain energy will be transferred back to the impactor, causing it to rebound. When the impactor bounces back, its velocity increases again. In terms of impact velocity, the second impactor for double 0 mm exhibits a different pattern. Even after colliding with the laminates, the impactor velocity is not reduced directly for a short period of time. This is due to the effect of deleted CZE and scaling the surface thickness of the plies by a factor of 0.8. This phenomenon does not occur in double 10 mm and 20 mm cases since the delamination has not been established in front of the second impact point.

The blue lines in Figure 5.3 show the contact force between the impactor and the top layer of the laminate. In contrast to the impactor velocity, the contact force gradually increases until it reaches the delamination initiation threshold, at which point it begins to fluctuate due to delamination propagation. Furthermore, the contact force increases until the impactor reaches its maximum displacement and returns to zero when the impactor bounces back completely. The first impactor for double 10 mm and 20 mm exhibits a slightly different contact force pattern compared to the single impact event. This is due to the position of the impactor which is not exactly at the center of the laminates. Additionally, the second impactor for double 0 mm presents a high contact force compared to the first impactor. The loss of transverse shear stiffness of the laminates due to the first impact will increase the maximum displacement of the second impact. This corresponds to the increasing contact force between the impactor and the top layer of laminates.

Figure 5.4 shows the energy-time curves for the first and second impact event. Figure 5.4(a) depicts the energy-time curves of the single impact event, as well as the energy response of the first impact event for all configurations of the double impact event. The energy-time curves for the second impact event of the double 0 mm and 10 mm are illustrated in Figures 5.4(b) and 5.4(c), respectively. Because the delamination caused by the second impact is independent of the delamination caused by the first impact, the energy-time curves for the second impact event for the double 20 mm are not shown in this work. In other words, the energy analysis of the second impact event is identical to the first one. Figure 5.4(a) shows that the kinetic energy of the impactor is converted to the internal energy or total strain energy which will be divided into recoverable strain energy and damage dissipation energy [87]. The kinetic energy becomes zero when the impactor reaches the maximum displacement. The laminated composite then transfers back the recoverable strain energy to the impactor, causing the impactor to bounce back and leaves the laminates in a swing motion. However, the change of the boundary condition as mentioned in 5.3.2 will make the swing motion stop.

Figure 5.4(b) demonstrates that for double 0 mm, the values of the damage dissipation energy for the second impact are much less than the first impact. This phenomenon occurs

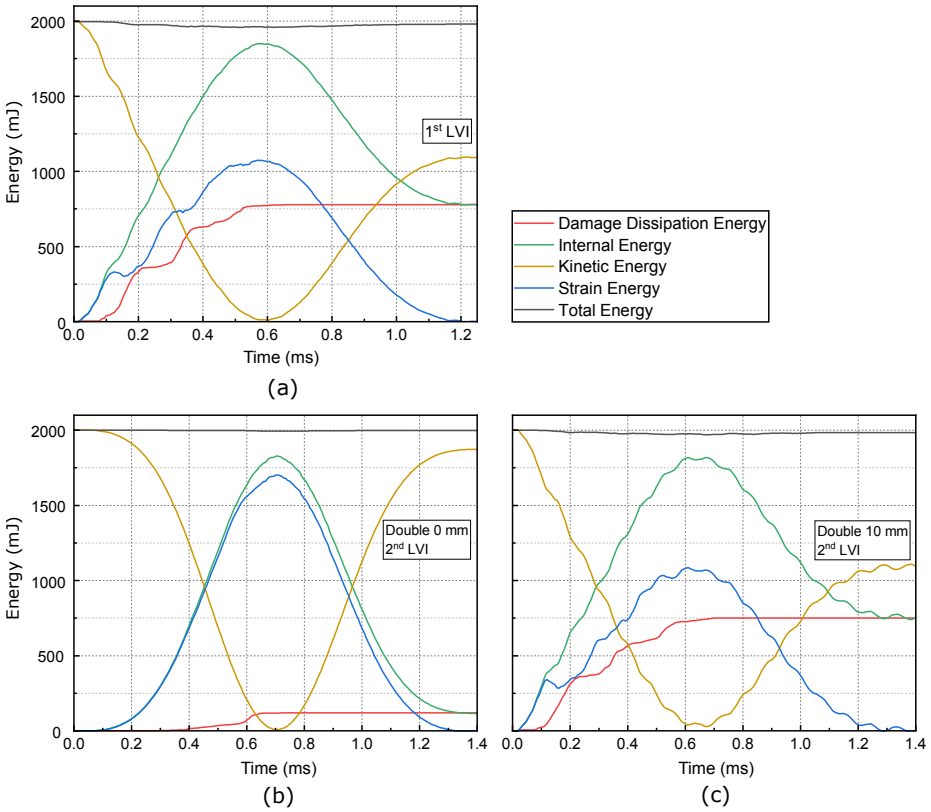

Figure 5.4: Energy-time curves for the (a) first and (b) second impact events of the double 0 mm, as well as (c) the second impact event of the double 10 mm.

due to the delamination that has already been established in the laminate. Consequently, the delamination propagation is began when the displacement of the second impactor is higher than the maximum displacement of the first impactor. In contrast, the recoverable strain energy of the second impactor when it bounces back will be higher than the first impactor. Figure 5.4(c) depicts how the kinetic, internal, and strain energies fluctuate during the second impact event. The fluctuation is caused by the interaction between the delamination generated by the first impact event and the delamination initiation as well as propagation during the second impact loading. Since Abaqus/Explicit is utilized, the total energy should remain constant during the impact event. However, the total energy in these configurations reduces slightly. This reduction can occur since element deletion is activated in the CZEs in case of fully damage.

The delamination damage state is represented by the stiffness degradation (SDEG) of the CZEs. When the SDEG of a CZE is equal to one, it is indicated that the CZE is fully damaged and is deleted in the simulation. The SDEG of the interface a of the laminate for all configurations is presented in Figure 5.5. Figure 5.5 shows that the delamination area due to the first impact has almost the same shape, but after the second impact, the shape of the delamination area is different. This difference occurs when the delaminations due to the first and second impacts interfere, interact, and do not interact with each other as shown in the cases of double 0 mm, double 10 mm, and double 20 mm, respectively. These delamination interference mechanisms are consistent with the experimental findings of Liao et al. [57].

The delamination area generated by the first and second impact event at every interface is illustrated in Figure 5.6. The delamination area on the double 10 mm and double 20 mm after the first impact event differs slightly from that of the single and the Double 0 mm. This phenomenon is caused by the fact that the impactor position of double 10 mm and double 20 mm cases is not at the center of the laminate. Overall, the delamination area after the first impact has a conical type damage from interface a to interface g, which conforms to the concept of delamination damage in a laminated composite structure under LVI [6, 23]. The delamination area at double 0 mm after the second impact event is increased slightly, while the delamination area at all interfaces remains similar. In comparison to other

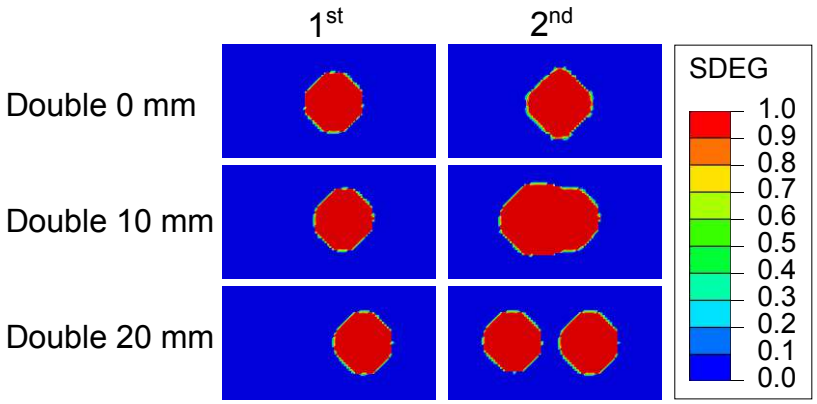

Figure 5.5: The stiffness degradation of the interface a of the laminate for the first and second impact events for all configurations.

configurations, the delamination area of double 10 mm after the second impact event is the largest. This phenomenon occurs because the delamination propagation during the second impact event interacts with the established delamination. Consequently, the established delamination is triggered to propagate. Furthermore, the delamination area of double 20 mm after the second impact event is about two times after the first impact event. It is due to the fact that delamination is not interacting with each other as shown in Figure 5.5.

5.4.2 Compression after Impact

Compression tests are simulated for all impacted samples along with the unimpacted sample (CUS) to determine the compressive strength of the laminated composites, as illustrated in Figure 5.7. It is observed that the compressive strength of the unimpacted sample is reduced by approximately 50% when the CAI is applied. For the single impact, the compressive strength is reduced from 634 MPa to 357 MPa. For double 0 mm, double 10 mm, and double 20 mm, the compressive strength is reduced from 634 MPa to 344 MPa, 311 MPa, and 338

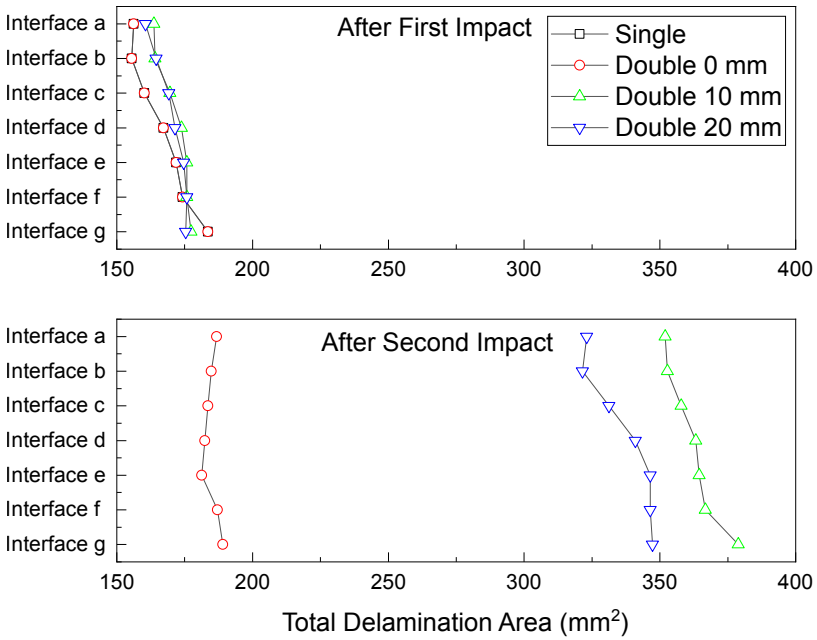

Figure 5.6: Delamination area after the first and the second impact events at every interface for all configurations.

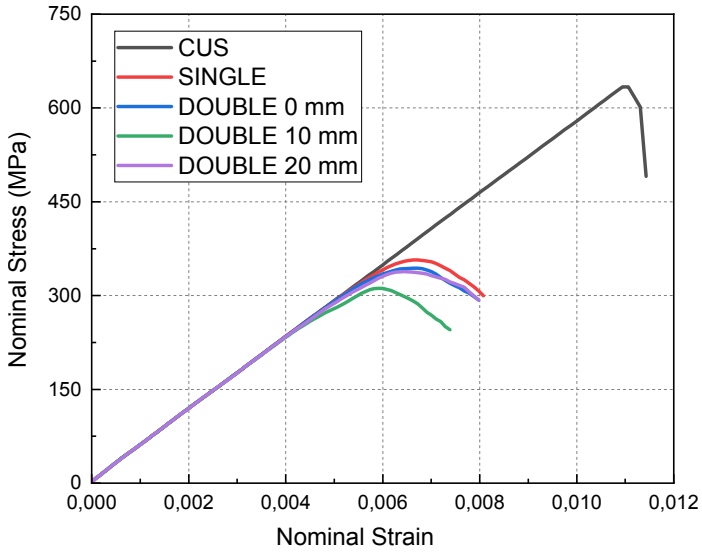

Figure 5.7: Predictions of the compressive strength of all impacted laminated composite plates along with the unimpacted laminated composite plate.

MPa, respectively. The compressive strength of the laminates is significantly affected by the delamination area for the studied configurations.

Figure 5.8 presents the stiffness degradation distribution of the CZEs where the fully damage CZEs are deleted (white regions at the center of the laminate). Figure 5.8 also shows that

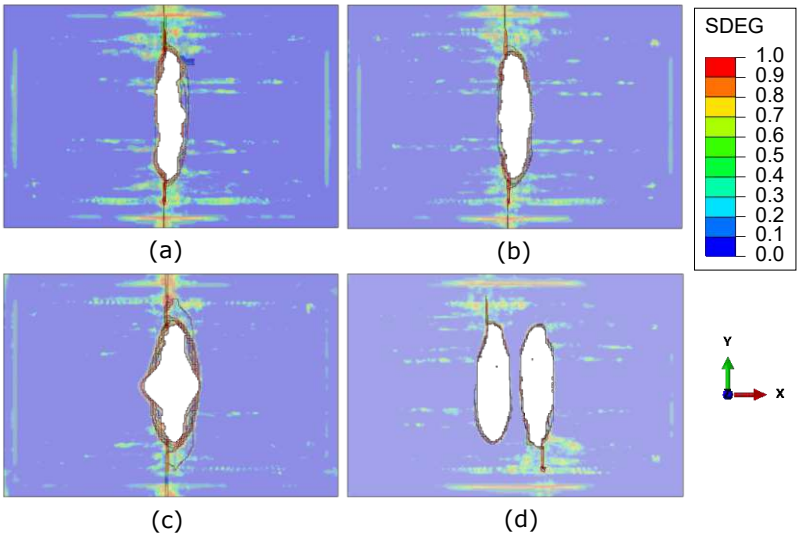

Figure 5.8: The stiffness degradation of the CZEs after compression load of (a) single, (b) double 0 mm, (c) double 10 mm, and (d) double 20 mm at the interface a

Table 5.3: Computational time comparison of LVI and CAI simulations.

	Element Number	DOFs	CPU Number	CPU Time (hrs) LVI	CAI	Total
Present study	561,435	1,448,580	48	1	2.5	3.5
Gonzalez et al.[45]	-	-	24	-	-	288
Lin and Wass[58]	-	1,431,852	72	3.4	2.7	6.1
Lopes et al.[62]	-	-	32	108	-	108
Zhang et al.[110]	180,000	-	48	-	-	9

all configurations exhibit the same failure mode, namely crack propagation through the impacted location, delamination propagation, and specimen crushing. Hence, the impact indentation causes a stress concentration effect in the specimens. This behavior is consistent with the studies of Anuse et al. [6].

As brief information about the efficiency of the conventional shell based ply-level modeling strategy in combination with finite thickness CZEs, a single LVI and CAI and its comparison with the previous study are summarized in Table 5.3. Table 5.3 lists that the present study configuration by implementing ply-based modeling strategy has the lowest computational time. However, generally, computation time is dependent on several factors including impact energy, size of the model, and element size.

5.5 Summary

The mechanical response, damage mechanisms, and compressive strength of laminated composites are comprehensively studied by performing single and double low velocity impact and compression after impact by the means of the Finite Element Method. From the numerical predictions, it can be concluded that different numbers of impact events as well as the impact position will lead to different delamination behavior, especially, if the delaminations interact with each other. Moreover, the low velocity impact loading reduces the compressive strength of the laminated composites by approximately 50% for all configurations. Finally, the use of ply-level modeling based on shell elements in combination with finite geometrical

thickness of cohesive zone elements for predicting the impact response and the compressive strength of laminated composite structures provide high computational efficiency.

Chapter 6

Fatigue After Impact

6.1 Introduction

Laminated composite structures made of fiber reinforced polymers (FRP) have become more and more important over the past two decades due to their great potential in weight saving. They are widely used in various applications where high specific strength and high specific stiffness are required, such as aircraft structures, sports equipment, and maritime transportation. However, the potential of FRP has not been fully exploited yet since their damage mechanism and failure behavior such as matrix cracking, fiber breakage, plasticity-like effects, and delamination [86] are not yet completely understood, especially when it comes to geometrically complex parts such as L-shape composite laminates.

Delamination is one of the major failure mechanisms that can significantly change the structural stiffness and the load carrying capacity of laminated composites [20, 43] and it can be considerably worse if cyclic loading condition is applied. Delamination usually occurs internally between two plies in laminated composites so that damage is barely visible to the naked eye on the composite surface. Hence, this damage is difficult to detect and repair during service. In this regard, the investigation of delamination growth in the laminated composite is an important study to determine the damage tolerance of the structure. In engineering applications, delamination can be caused by normal and shear tractions acting

on the interface, which are caused by transverse loading, ply-drop-off, free edge effect, or local load introduction [109]. Additionally, delamination can also be initiated by an external load such as low velocity impact during manufacturing, normal operation, maintenance, and/or other stages of their life cycle.

A numerical approach by means of the Finite Element Method (FEM) has been extensively developed for predicting the delamination onset and propagation behavior in the laminated composite. The use of numerical methods can be very beneficial for simulating delamination behavior under various loading conditions and at various length scales [4, 28]. Several techniques for predicting the delamination growth have been successfully developed based on Linear Elastic Fracture Mechanics (LEFM), such as crack tip elements [34], J-integral [73, 78], the Virtual Crack Extension Technique [50], and the Virtual Crack Closure Technique (VCCT) [55, 75, 81]. A numerically efficient semi-analytical approach has been introduced by Wimmer and Pettermann [108] for the prediction of delamination growth and its stability. Furthermore, a Cohesive Zone Model (CZM) has been proposed in the studies of Dugdale [38] and Barenblatt [15] in which nonlinear interface behavior is taken into account. Based on this idea, Cohesive Zone Elements (CZE) have been developed within the framework of FEM to simulate the delamination of laminated components [59, 86, 103], debonding [67], and crack propagation [51].

Damage models of the cohesive zone element are special of interest if the laminates are subjected to cyclic loading conditions. Bak et al. [12] divided the cohesive damage models for cyclic loading into two categories including the hysteresis loop damage and the envelope displacement damage models as illustrated in Figure 6.1(a) and 6.1(b), respectively. The hysteresis loop damage model is defined by modeling the entire cyclic variation of the applied displacement to determine the damage per cycle, while the envelope displacement damage model only considers the maximum displacement of the cycle [12]. Generally, the hysteresis loop damage model is typically used in low cycle fatigue applications, whereas the envelope displacement damage model is used in high cycle fatigue problems [56, 94].

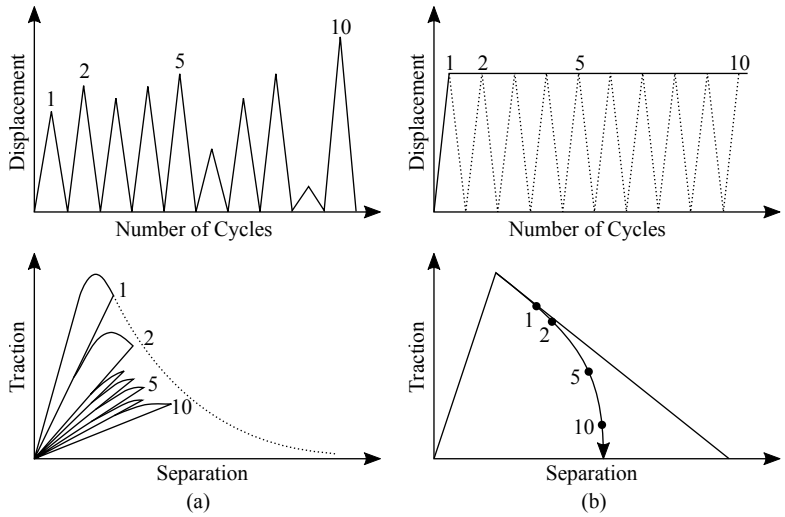

Figure 6.1: Schematic representation of the traction-separation evolution during cyclic loading. (a) hysteresis loop damage model with varying displacement amplitude, (b) envelope displacement damage model with a fixed displacement amplitude (modified from [12]).

The focus of this study is on the investigation of the delamination behavior of unidirectional (UD) L-shape composite laminates under low velocity impact followed by static and cyclic loading conditions by using the commercial FEM package Abaqus 2020 (*Dassault Systèmes Simulia Corp., Providence, RI, USA*). A ply-level modeling strategy based on conventional shell elements in combination with the finite geometrical thickness of CZE is utilized since it has been found efficient in [4, 86]. The low velocity impact is applied on the sharply curved geometry of L-shape laminates to obtain the delamination distribution. An explicit simulation scheme is used to mimic the highly nonlinear dynamic impact response of the laminates. Since the impact energy is really low, the damage of the plies is not taken into account during the impact simulation. Furthermore, the delamination distribution due to impact is then utilized as the initial condition for static and cyclic loading scenarios. By using an implicit simulation scheme, four different configurations are studied by combining positions and directions of the displacement to examine the maximum static load bearing capacity of the laminates. Moreover, cyclic loading conditions are applied to investigate the fatigue life of the L-shape laminates by utilizing the envelop damage model. In cyclic loading conditions, a user material (UMAT) is implemented into the FEM package ABAQUS to

include a fatigue constitutive model for cohesive elements. The delamination behavior due to low velocity impact, static, and cyclic loading conditions are evaluated in terms of the delamination area, load-displacement curves, delamination propagation, and fatigue life of the L-shape composite laminates.

6.2 Cohesive damage model

In the present study, the cohesive damage model is modeled by using a bi-linear traction–separation law (TSL) as shown in Figure 2.9. Within the elastic range, the normal and shear traction components are assumed to be uncoupled. It has to be noted that the selection of the cohesive damage model is based on the simulation scheme and loading scenario. For impact loading scenarios, damage initiation is predicted according to a quadratic nominal stress criterion [33]. Damage evolution is modeled based on the critical energy release rates in combination with a linear softening law. The Benzeggagh and Kenane (BK) criterion is used to treat the mixed mode behavior [17]. Once the damage variable reaches a value of 0.9999 at all integration points of a CZE, it is considered fully damaged.

The cohesive damage model for static and cyclic loading build upon the formulation from the work of Turon et al. [97, 98, 101] the work of Bak et al. [13] that has already mentioned in Chapter 2. A Paris law like approach based on the non–local measurement of the energy release rate [13] and the measurement of the cohesive area [101] is implemented to account for the delamination propagation for cyclic loads in which the envelope damage model is utilized. This approach is based on a relationship between the evolution of the damage variable and the crack growth rate which is defined in Equation (2.37). A cycle jump technique based on the work of Van Paepegem and Degrieck [71] is utilized because a cycle by cycle simulation would require high computation time, especially for high cycle fatigue problems. It should be noted that the accuracy of the results will depend on the number of skippable cycles. If the number of skippable cycles is increased, the simulation time will be lower, but the accuracy of the results will be decreased. Finally, the total damage of the CZE can be defined as

$$d_{tot} = d_{ini} + d_{stat} + d_{cyc} \tag{6.1}$$

where d_{ini} is the initial damage due to impact loading, d_{stat} is damage created by the quasi-static loads and d_{cyc} is the damage due to cyclic loads. It has to be noted that the d_{cyc} can be calculated if the number of cycles is more than one and d_{stat} is lower than one.

6.3 Numerical procedures

6.3.1 L-shape composite laminates

The overall dimensions of the L-shape composite laminate are presented in Figure 6.2. The L-shape laminate is 3 mm thick and 1 mm width, with two side lengths of 10 mm, and the inner radius at the curved geometry of the L-shape laminate is 5 mm. The laminate is composed of 8 plies and modeled by implementing the ply-level based modeling strategy. The CZEs share the nodes of the adjacent plies which are positioned at the corresponding midplanes of plies. Consequently, the thickness of the CZE is the same as the thickness of the corresponding shell elements where each ply is 0.375 mm thick. It has to be noted that despite their finite geometrical thickness, the CZEs mimic the mechanical behavior of a zero geometrical thickness since an uncoupled traction-separation based constitutive law is applied [86]. Furthermore, the average element size at the curved geometry is 0.16 mm.

The material and interface properties are summarized in Table 6.1. The elastic properties are represented as Young's modulus, E, shear modulus, G, and Poisson's ratio, ν for all planes and directions. The same initial stiffness is assigned to all cohesive zone elements in normal, shear, and transverse direction of K_n, K_s, and K_t, respectively, independent to the geometrical thickness. The interface strengths and the critical strain energy values in opening and shear modes are denoted by t_{iC} and $\mathcal{G}_{iC}$ (i = I, II), respectively. The fatigue properties are represented by Paris law constants, C and m, and the interface fatigue threshold, $\mathcal{G}_{ith}$ (i = I, II). Additionally, The mass density of the laminates is distributed

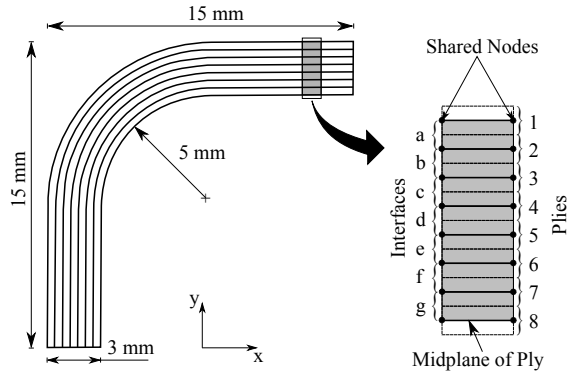

Figure 6.2: The overall dimensions and the coupling technique between the finite thickness of cohesive zone element as interface and the adjacent plies of the L-shape laminated composites.

between the plies and interfaces, where the mass density assigned to the plies is 0.52 kg/m^3, and the mass density assigned to the cohesive zone element is 0.32 kg/m^3 [93].

Table 6.1: Elastic, interface, and fatigue properties for a HTA/6376C (UD) carbon fiber/epoxy material [7, 18, 47, 94]. The interface fatigue thresholds are taken from [101].

Elastic Properties					
E_x	$E_y = E_z$	$G_{xy} = G_{xz}$	G_{yz}	$\nu_{xy} = \nu_{xz}$	ν_{yz}
120 GPa	10.5 GPa	5.25 GPa	3.48 GPa	0.3	0.51
Interface Properties					
$K_n = K_s = K_t$	t_{IC}	t_{IIC}	$\mathcal{G}_{IC}$	$\mathcal{G}_{IIC}$	η
$10^5 \frac{N}{mm^3}$	30 MPa	60 MPa	0.26 $\frac{N}{mm}$	1.002 $\frac{N}{mm}$	2.73
Fatigue Properties					
C_I	C_{II}	C_m	m_I		
$2.21 \cdot 10^{-3} \frac{mm}{cycle}$	$1.22 \cdot 10^{-1} \frac{mm}{cycle}$	$6.09 \cdot 10^{5} \frac{mm}{cycle}$	5.09		
m_{II}	m_m	$\mathcal{G}_{Ith}$	$\mathcal{G}_{IIth}$		
4.38	5.48	0.06 $\frac{N}{mm}$	0.10 $\frac{N}{mm}$		

6.3.2 Loading scenarios

Three different loading scenarios are sequentially implemented including impact, quasi static, and cyclic loads as illustrated in Figure 6.3. Figure 6.3(a) presents the impact loading configuration where the L-shape laminates are fixed on all edges. The impactor is modeled as a quasi rigid body since the impactor can be approximated as a rigid body in comparison to the laminates [70]. A cylindrical impactor with a diameter and width of 30 and 1.2 mm, respectively, are chosen. Even though the impactor is assumed as a rigid body material, the mass density of 224.23 kg/m^3 is defined to obtain a total moving mass of 0.2 kg. Furthermore, the impactor velocity of 1.75 m/s is applied in the present study. It has to be noted that only inter-laminar damage is considered in this configuration.

Figure 6.3(b) shows the quasi static loading configuration where the impact damage has been established in the L-shape laminates. The L-shape model is rotated counterclockwise by 45°, so that the displacement load can be easily determined. Since the delamination of the L-shape laminate due to impact is most likely to be asymmetrical between the upper and

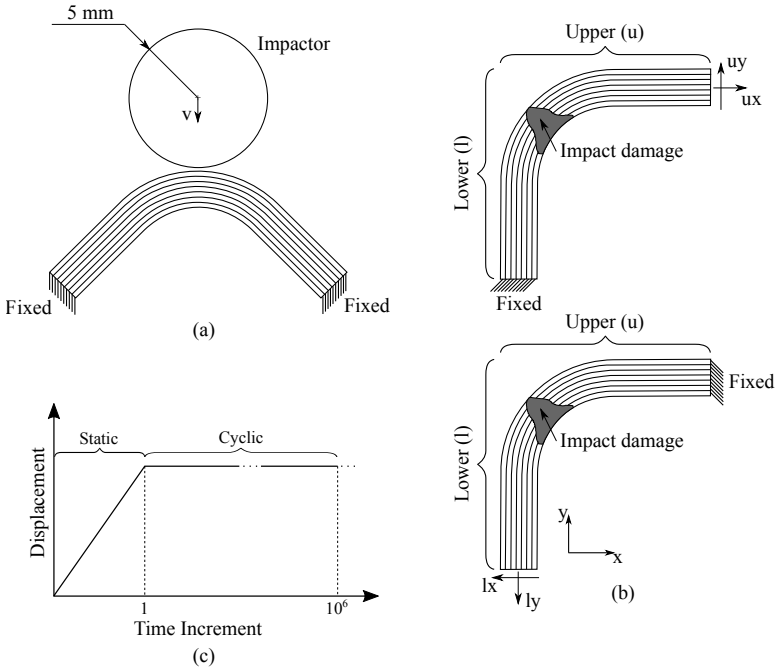

Figure 6.3: Three different loading scenarios including (a) impact, (b) quasi static, and (c) cyclic loads.

lower arms, the loading scenario on the upper and lower arms is implemented by applying displacement in the x and y directions. When the displacement on the upper arm is applied, the lower edge will be fixed, and vice versa. For the displacement loading purpose, all nodes of the individual layers at the edge are connected to a reference point via kinematic coupling constraint. The individual points thus carry out the exact same movement as the reference point. For simplification, the upper displacements are denoted by ux and uy while the lower displacements are denoted by lx and ly. Furthermore, all configurations will be named as "DISPLACEMENT LOADING POSITION AND DIRECTION_ARM POSITION_NUMBER OF INTERFACE". For instance, ux_u_c represents displacement loading at the upper edge in x-direction, at upper arm delamination, and at the third interface from the top layer as shown in Figure 6.2.

Figure 6.3(c) illustrates the enveloped displacement load that will be used for cyclic loading scenarios. In this case, all of quasi static simulation set-ups are utilized. However, the maximum displacement for cyclic load is set where the maximum load bearing capacity of the L-shape laminates has not yet been reached and the delamination has not yet propagated. The maximum displacement of 0.7 mm is used in the present study for all displacement configurations.

6.3.3 User Material

A commercial software package Abaqus is a powerful tool based on FEM to analyze a wide range of structural problems. Abaqus also provides the option of adding user subroutines to adapt the analysis to specific needs. In this study, the User material (UMAT) subroutine is implemented into the FEM package ABAQUS to account for a fatigue constitutive model for cohesive elements described in Section 6.2. A UMAT routine is called at each integration point in every iteration of the analysis. The inputs of a UMAT routine are the stresses and strains at the start of the iteration and the strain increments. The material properties are defined before the start of the analysis and will not change over the course of the analysis. The output of the routine is the stress increments and the tangent stiffness tensor. These

outputs are used by Abaqus to compute the inputs for the next iteration. The UMAT subroutine to implement the constitutive model under quasi-static and cyclic loadings (see Appendix A) is modified from the work of Eva Smeets [92] and written according to the flowchart presented in Figure 6.4. The modification is used to account the mixed mode loading conditions of the L-shape laminated composites in accordance with Equations (2.38) and (2.39).

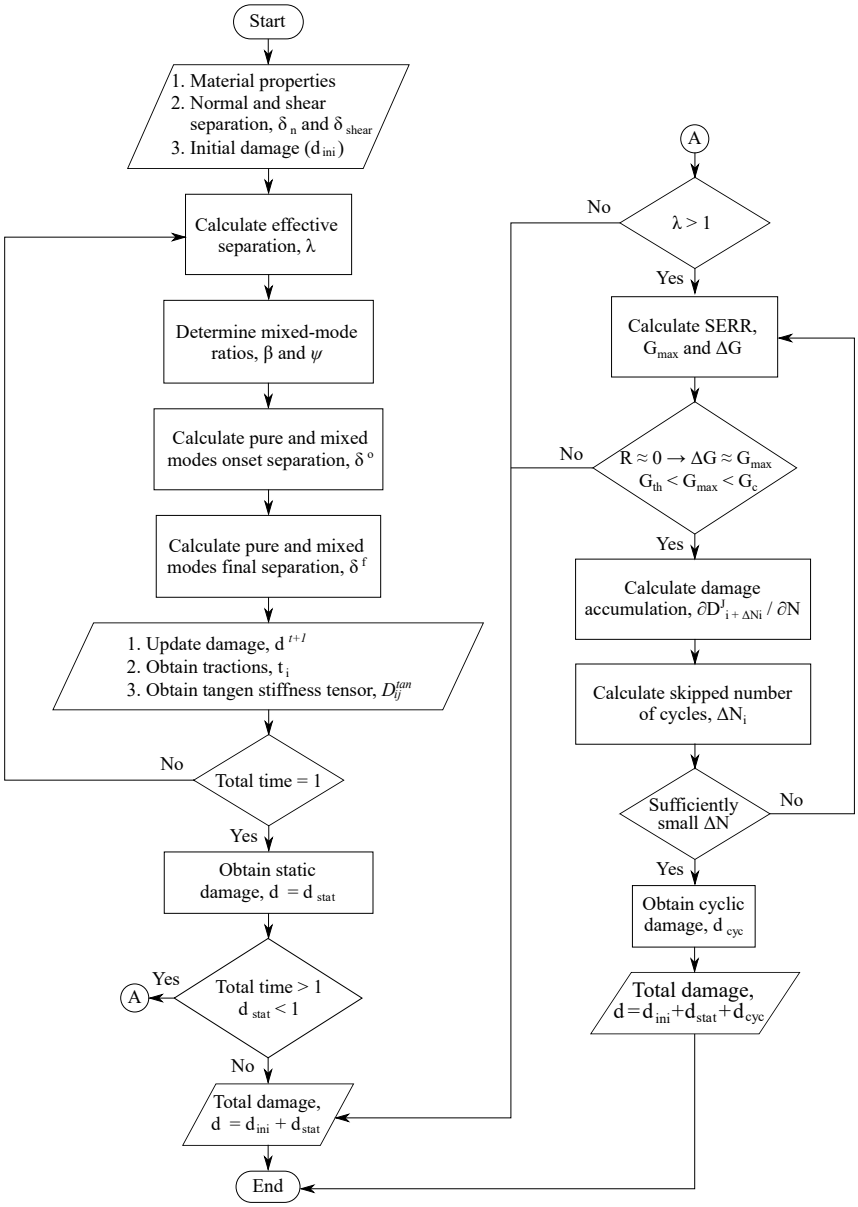

Figure 6.4: Flowchart of the UMAT routine for static and cyclic loading.

6.4 Results and Discussion

The following results are solely obtained by means of numerical simulations. All simulations are carried out using a standard PC workstation with eight CPUs at 2.35 – 3.35 GHz. Three different load cases are sequentially explained including impact loading, quasi static loading, and cyclic loading.

6.4.1 Impact loading

Figure 6.5 shows (a) the displacement of the curve tip of the top layer in y-direction, the reaction force, and the damage dissipation energy during low velocity impact event as well as (b) stiffness degradation (SDEG) of the CZEs of the L-shape laminates after low velocity impact event. Figure 6.5(a) shows that the displacement of the top layer in y-direction is smoothly changed during the impact event. This phenomenon demonstrates that there is no ply damage in laminated composites. Moreover, after the time increment of 0.00045, a swing motion appears due to the impactor has been completely bounced back. Figure 6.5(a) also shows that the reaction force of the laminates is suddenly dropped at the same time with the increase of damage dissipation energy. This indicates that delamination has been established in the L-shape laminates. Figure 6.5(b) illustrates the SDEG of the L-shape laminates due to impact loading. The SDEG distribution of the CZEs can be divided into

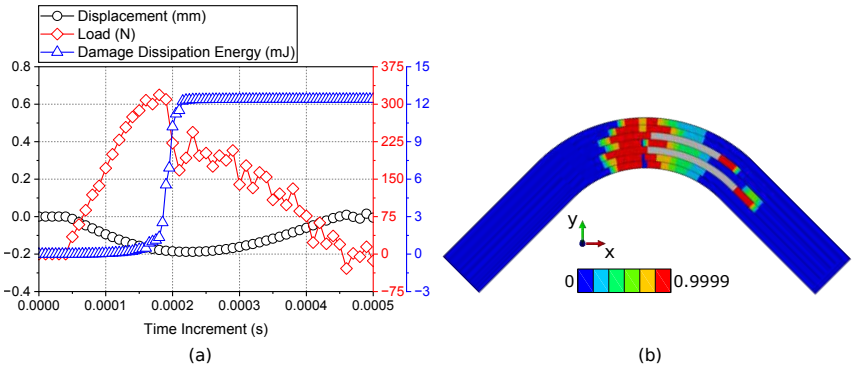

Figure 6.5: (a) The displacement of the top layer in y-direction, the reaction force, and the damage dissipation energy over the time increment as well as (b) stiffness degradation (SDEG) of the CZEs of the L-shape laminates.

three categories i.e. undamaged, partially damaged, and fully damaged as represented by dark blue color, dark light to red colors, and grey color, respectively. Fully damaged CZEs which possess a stiffness degradation value of 0.9999 is represented as delamination. All of the SDEG distribution will be utilized as the initial damage of the L-shape laminates under quasi static and cyclic loadings. Moreover, it can be seen that the delamination occurs only at the interface-c and interface-e (see Figure 6.2) and shows unsymmetrical delamination in the L-shape laminates. This unsymmetrical delamination occurs together with the perturbation of the L-shape laminate during the impact event. This perturbation can be observed in the displacement of the top layer in the x-direction as shown in Figure 6.6. Figure 6.6 shows that there are 4 stages of the impact event. Firstly, the impactor does not collide with laminates and there is no perturbation at the top layer of laminate. Secondly, the impactor collides with the laminate but delamination has not yet occurred. In this stage, a small perturbation in positive x appears along with the movement of the impactor. The perturbation is then suddenly increased in the third stage when delamination occurs. The perturbation tends to be positive x since the perturbation tends to be positive x at the second stage. This will affect the unsymmetrical delamination in L-shaped laminates. If the perturbation is in positive x, the delamination occurs in the positive x region, and vice versa. The perturbation then drops to zero which indicates that the impactor has bounced back completely. Finally, the swing motion also occurs in the x-direction.

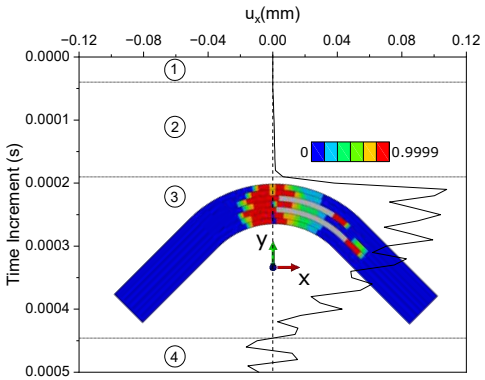

Figure 6.6: The displacement of the top layer in x-direction for different stage of low velocity impact event

6.4.2 Quasi static loading

Figure 6.7 shows the load-displacement curve of unimpacted and impacted L-shape laminates under various quasi static loading configurations. The displacement loading configurations are divided into parallel (ux and ly) and perpendicular (uy and lx) to the arm of the L-shape laminates. For the parallel category, the load bearing capacity of the laminates is reduced to ±60 N and ±48 N due to displacement loading of ux and ly, respectively. Furthermore, the stiffness of the laminates due to ly is more compliant than ux implies the ly is more critical. It has to be noted that the maximum load bearing capacity of the unimpacted L-shape laminates is approximately 120 N. However, an unstable equilibrium delamination growth takes place due to snap back behavior [109]. For the perpendicular category, the maximum load bearing capacity and the stiffness of the laminates are significantly lower than the parallel displacement loading. The maximum load bearing capacity of the laminates is reduced by approximately 85 % compared to the unimpacted laminates. With this respect, the maximum displacement load of 0.7 mm is used for cyclic loading conditions.

Figure 6.8 illustrates the development of the stiffness degradation under quasi-static loading in which the initial delamination due to impact is at the center. For ux, lx, and ly displacement loadings, delamination propagation only occurs at the interface-e. Whereas, for uy

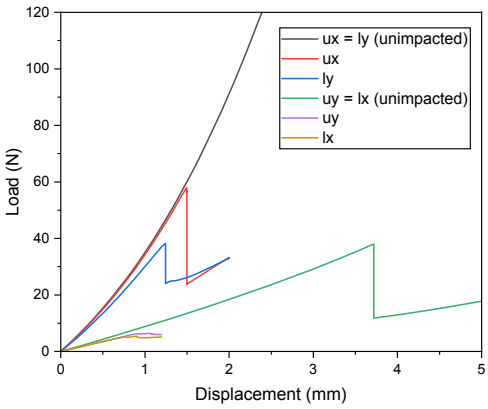

Figure 6.7: The load-displacement curve of unimpacted and impacted L-shape laminates under various quasi static loading configurations.

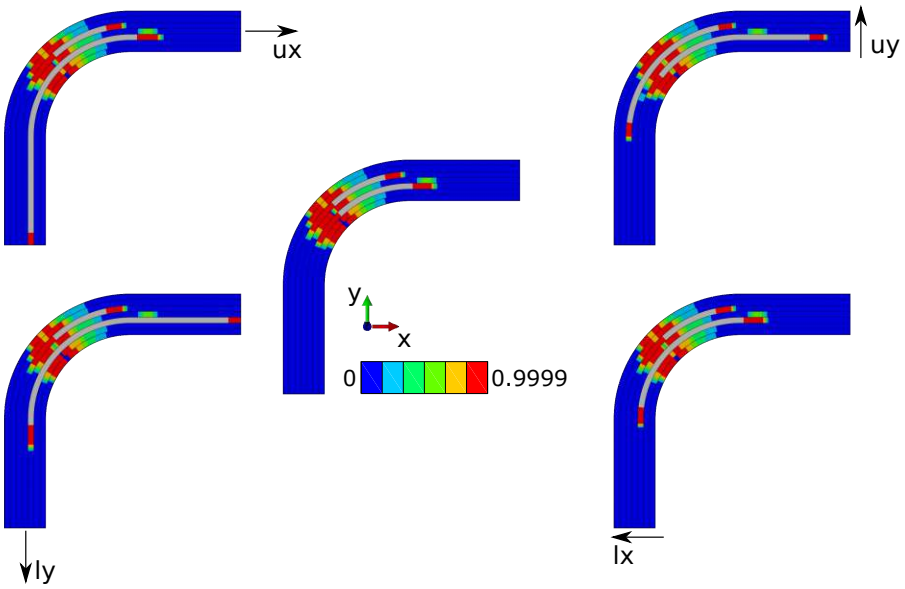

Figure 6.8: The development of the stiffness degradation under various quasi-static loading in which the initial delamination due to impact is at the center.

displacement loading provides delamination propagation at both interface-c and interface-e. Moreover, for both ux and ly displacement loading, the delamination propagation pattern is the same which occurs at the arm opposite to the loading arm and towards the support. This is mainly due to the dominance of the shear mode on the opposite arm.

6.4.3 Cyclic loading

Figures 6.9 and 6.10 present fatigue delamination growth rate and mode-mixity of the cyclic loading simulations under displacement loading configurations which are parallel and perpendicular to the arm of the impacted L-shape laminates, respectively. The nonlinearity of the fatigue delamination growth rate and mode-mixity demonstrate that the implementation of the dependency of the parameters C and m on the mode ratio works. Figure 6.9 is more focused on the displacement load which is parallel to the loading arm. Consequently, the laminates are dominated in shear mode. This phenomenon corresponds to the mode-mixity that is shown in Figure 6.9(a) and 6.9(b) which is close to 1. Consequently, the fatigue delamination growth rate is accelerated. This behavior is consistent with the

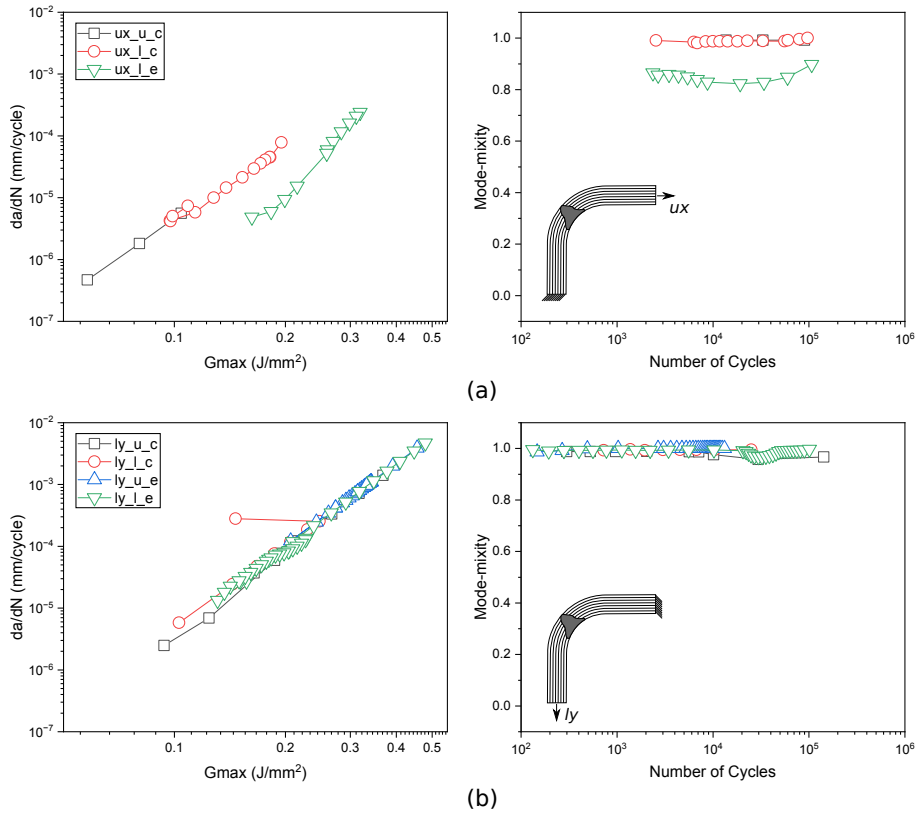

Figure 6.9: Fatigue delamination growth rate and mode-mixity of the cyclic loading simulations under parallel displacement loading configurations i.e. (a) ux and (b) ly.

studies of Springer et al. [94]. Figure 6.9 is specific to the perpendicular displacement load. Figure 6.10(a) shows that the mode-mixity is ranging from 0.2-0.6 under uy while under 0.2 if lx is applied. In other words, the laminates are in the domination of opening mode. As a result, the fatigue delamination growth rate is low.

Figure 6.11 illustrates the development of the stiffness degradation under cyclic loading in which the initial delamination due to impact is at the center. Under ly displacement loading, the L-shape laminates encounter the largest delamination area that is established due to cyclic loading. This is shown that if shear mode occurs, the growth rate of fatigue delamination will be high compared to opening mode.

The development of the delamination area over the number of cycles is illustrated in Figure 6.12. Figure 6.12(a) presents the delamination development of the laminates under ux

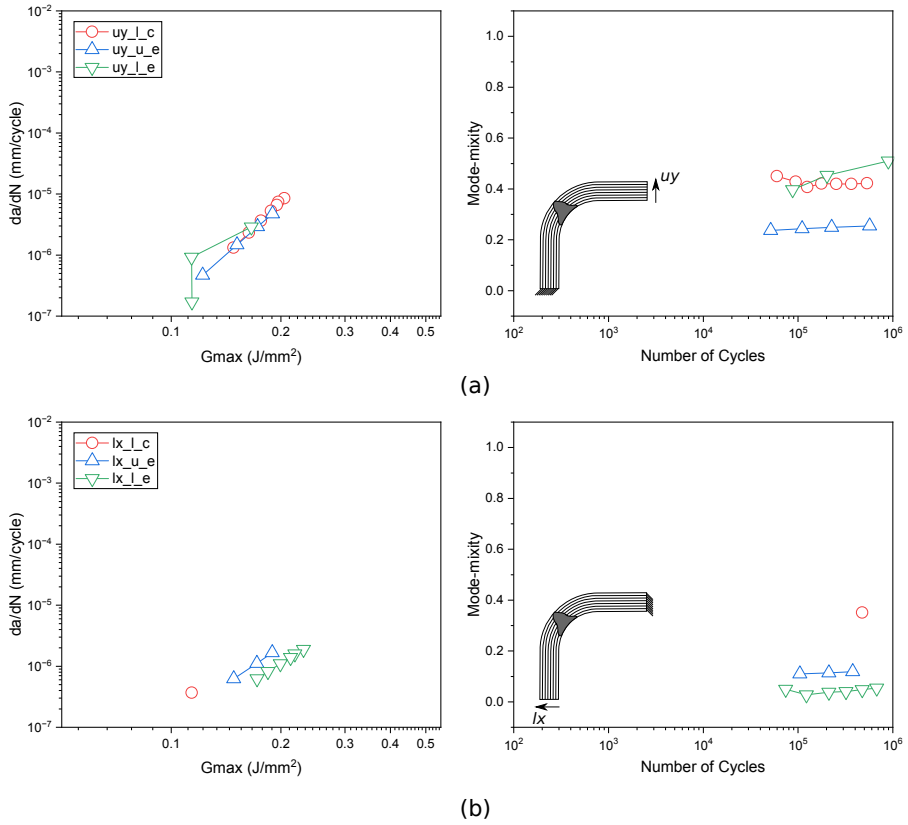

Figure 6.10: Fatigue delamination growth rate and mode-mixity of the cyclic loading simulations under perpendicular displacement loading configurations i.e. (a) uy and (b) lx.

displacement load. The delamination starts to propagate at the lower arm after 2,000 cycles and stops at 100,000 cycles. The delamination also propagates at the interface c of the upper arm after 10,000 cycles. This phenomenon has occurred because the initial delamination is parallel to the given displacement loading. On the contrary, when the initial delamination is perpendicular to the given displacement loading the acceleration of the delamination propagation is much faster as shown in Figure 6.12(b). The delamination at interface c and e propagates in all directions before 1,000 cycles. The total development delamination area at interface e reaches the largest delamination area of 11.5 mm^2 and reaches the support at the upper arm. Meanwhile, the total delamination area at interface c is about 2.5 mm^2. As a result, ly become the most critical loading conditions for L-shape laminates. Additionally, sudden change of the delamination development also occurs at interface e at

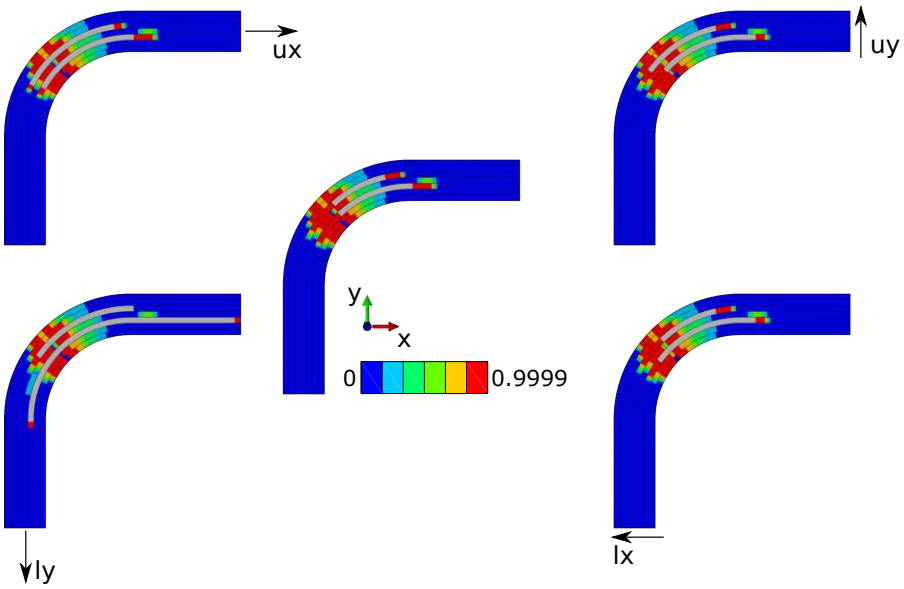

Figure 6.11: The development of the stiffness degradation under cyclic loading which the initial delamination due to impact is at the center.

the upper arm. This phenomenon is caused by the stiffness reduction in the laminates since the large delamination area has been established which will accelerate the delamination propagation. Differently, the sudden change in delamination development at interface e at the lower arm appears when the delamination reaches the support at the upper arm. Revisiting Figure 6.7, the given displacement load of 0.7 mm will lead to a reaction force of approximately 20 N and 5 N for parallel and perpendicular conditions, respectively. This condition will also affect the acceleration of delamination propagation. Figures 6.12(c) and 6.12(d) demonstrate the delamination development when the perpendicular displacement load is applied to the L-shape laminates. Both configurations provide a similar pattern. The delaminations start to propagate at 80,000 cycles and stop at a large number of cycles and dominate in the lower arm region. The total development delamination is about 2.5 mm^2 in each configuration.

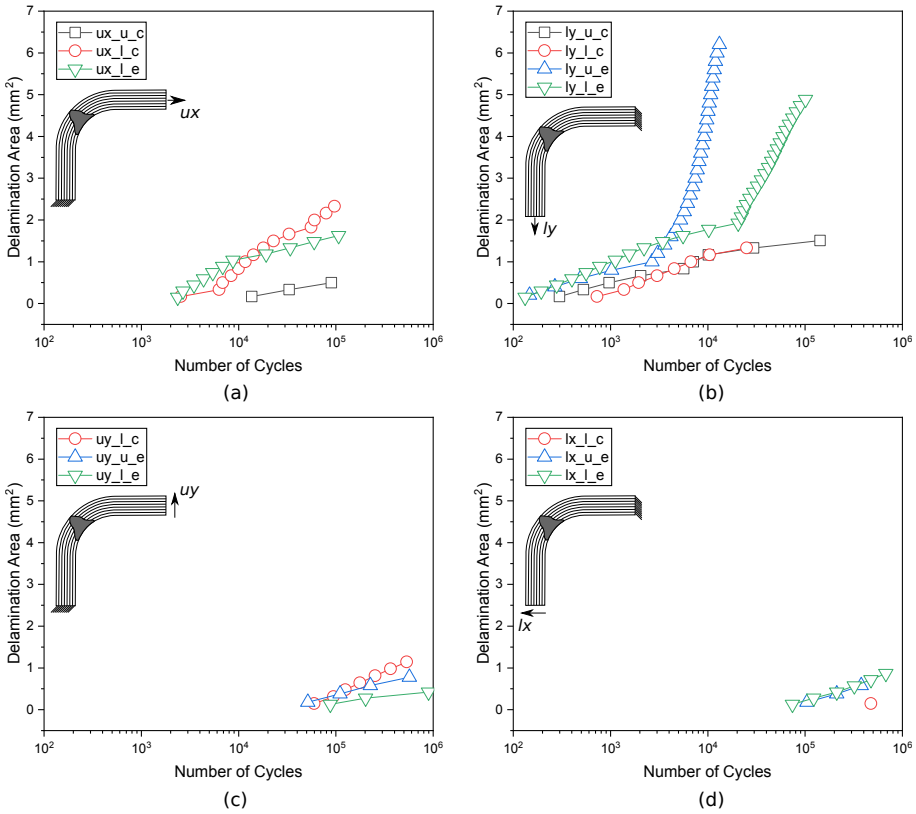

Figure 6.12: Development of the delamination area over the number of cycles for different displacement loading configurations i.e (a) ux, (b) ly, (c) uy, and (d) lx.

6.5 Summary

The fatigue after impact analysis of L-shape composite laminates is comprehensively studied by means of the Finite Element Method. From the numerical predictions, the structural integrity of the laminates can be significantly reduced due to impact loading at the geometrical complex parts. Moreover, the mode-mixity at the delamination tip will lead to different fatigue delamination growth rates. Consequently, the acceleration of the development of the delamination area is influenced. Finally, the implementation of the user material subroutine into the Abaqus package provides an advanced prediction tool to incorporate fatigue constitutive models for finite geometric thicknesses of cohesive zone elements, especially, when damage has formed at interfaces such as delaminations.

Chapter 7

Summary

Within the present work, ply-level based modeling strategies are utilized for predicting delamination behavior in laminated composites under various loading conditions and simulation schemes, by means of advanced methods within the framework of the FEM. Five different loading scenarios such as pure and mixed mode loading conditions, low velocity impact (LVI), compression after impact (CAI), and fatigue after impact (FAI) are applied to laminated composite, resulting in delamination. Meanwhile, three different simulation schemes are implemented in terms of implicit, explicit as well as combination between implicit and explicit.

For the case of pure and mixed mode loading conditions, an investigation and comparison study of four different 3D and one 2D ply-level modeling strategies are done in terms of delamination behavior such as load-displacement curves, delamination area, computation time, and mode-mixity during delamination propagation. Generally, all configurations provide a very good agreement when compared to analytical results used as reference which is based on corrected beam theory. However, the ply-level approach based on shell elements in combination with finite thickness cohesive zone elements exhibits very good performance in terms of accuracy of the result as well as computational efficiency. Consequently, the implementation of this strategy can be particularly useful for predicting delamination behavior in complex and large-scale laminated composite structures. Additionally, a comparison study

of transverse shear behavior of homogeneous plane strain isotropic beams is also conducted for different ply-level based modeling strategies. Again, the ply-level approach based on shell elements in combination with finite thickness cohesive zone elements provides a very good agreement to the analytical solutions based on Euler-Bernoulli and Timoshenko beam theories in terms of deflection, transverse shear stress, and normal bending stress.

Due to its high computational efficiency, the use of a ply-level approach based on shell elements combined with cohesive zone elements of finite thickness is the best choice for impact loading conditions in laminated composites. In this study, single and double low velocity impacts as well as compression after impact are applied to laminated composites to investigate the mechanical response, damage mechanism, and compressive strength. From the numerical prediction, it can be seen that different numbers of impact events as well as impact positions will cause different delamination behaviors. The distance between two impact positions provides different delamination interference mechanisms which are consistent with previous experimental findings. These differences will lead to different energy dissipation and delamination area of the laminates. Moreover, the compressive strength of the laminates after impact loading reduces by approximately 50% for the present study configuration. Generally, the implementation of a ply-level based modeling provides high computational efficiency for predicting the impact response and the compressive strength of laminated composite structures compared to the previous research.

The investigation of delamination behavior of L-shape composite laminate as one of the geometrically complex aircraft parts is comprehensively studied. Three different loading conditions are sequentially implemented including impact, static, and cyclic loads. Low-velocity impact is applied to obtain the delamination distribution by using an explicit simulation scheme. The delamination distribution due to impact is then used as the initial condition for static and cyclic loading conditions. Using the implicit simulation scheme, four different configurations are performed by combining the displacement position and direction to examine the maximum load capacity of the laminate. In addition, cyclic loading conditions are performed to investigate the fatigue life of the L-shape laminate where the user material (UMAT) is implemented into the ABAQUS FEM package to include a fatigue constitutive

model for the cohesive elements. The results showed that multi-layered delamination is initiated due to low velocity impact. The maximum load, delamination propagation acceleration, and mode-mixity are mainly affected by the delamination distribution as well as the loading configuration. In addition, the mode-mixity at the delamination tip will cause different growth rates of fatigue delamination. As a result, the accelerated development of the delamination area will be affected. Finally, the implementation of the user material subroutine into the Abaqus package provides an advanced prediction tool to incorporate fatigue constitutive models for finite geometric thicknesses of cohesive zone elements, especially, when damage has formed at interfaces such as delaminations.

Appendix A

User Material Subroutine

The User Material (UMAT) subroutine is implemented into the FEM package ABAQUS to account for a fatigue constitutive model for cohesive elements described in Section 6.2. It has to be noted that the framework of this subroutine is mainly taken from the work of Eva Smeets [92] which can be accesed via `https://repository.tudelft.nl/islandora/object/uuid:ac18b7c8-8769-4c21-837c-edde62a4b3da/datastream/OBJ/download`.

```
c
c UMAT FOR COHESIVE ZONE ELEMENT UNDER STATIC AND FATIGUE LOADING
c ===================================================================
c
c COPYRIGHT (C) 2023, VIENNA UNIVERSITY OF TECHNOLOGY (TU WIEN), AUSTRIA.
c THE CODE IS DISTRIBUTED UNDER A BSD LICENSE.

c AUTHOR            : KHAIRUL ANAM
c EMAIL             : anam@ilsb.tuwien.ac.at
c NOTE THAT, THE FRAMEWORK OF THIS CODE ARE MAINLY TAKEN FROM THE WORK OF
c EVA SMEETS (https://repository.tudelft.nl/islandora/object/uuid:ac18b7c8
c -8769-4c21-837c-edde62a4b3da/datastream/OBJ/download)
c ACKNOWLEDGEMENT   : EVA SMEETS (E.T.B.Smeets@tudelft.nl)

      SUBROUTINE UMAT(STRESS,STATEV,DDSDDE,SSE,SPD,SCD,
```

```
     1 RPL,DDSDDT,DRPLDE,DRPLDT,
     2 STRAN,DSTRAN,TIME,DTIME,TEMP,DTEMP,PREDEF,DPRED,CMNAME,
     3 NDI,NSHR,NTENS,NSTATV,PROPS,NPROPS,COORDS,DROT,PNEWDT,
     4 CELENT,DFGRD0,DFGRD1,NOEL,NPT,LAYER,KSPT,JSTEP,KINC)
C
      INCLUDE 'ABA_PARAM.INC'
C
      CHARACTER*80 CMNAME, CPNAME
      DIMENSION STRESS(NTENS),STATEV(NSTATV),
     1 DDSDDE(NTENS,NTENS),DDSDDT(NTENS),DRPLDE(NTENS),
     2 STRAN(NTENS),DSTRAN(NTENS),TIME(2),PREDEF(1),DPRED(1),
     3 PROPS(NPROPS),COORDS(3),DROT(3,3),DFGRD0(3,3),DFGRD1(3,3),
     4 JSTEP(4)
C
      DIMENSION CFULL(NTENS,NTENS), DELTAE(NTENS)
      DOUBLE PRECISION KK, TN, TS, TT, G1C, G2C, G3C, ETA, G1TH
      DOUBLE PRECISION RATIO, C1, M1, C2, M2, CM, MM, E3, DMG_MAX
      DOUBLE PRECISION E11, E22, G12, V21, DMG_OLD, TAU_OLD, DELTA_OLD
      DOUBLE PRECISION G_MAX_OLD, DDDN_OLD, DELTAN, DELTAS, DELTAT
      DOUBLE PRECISION DELTAN_MAX, DELTA_SHEAR, DELTA0_N, DELTA0_SHEAR
      DOUBLE PRECISION DELTA0, DELTAC_N, DELTAC_SHEAR, DELTAF, DELTAG
      DOUBLE PRECISION DMG, TAU, DELTA, G_MAX, DADN, DDDN, BETA
      DOUBLE PRECISION PSI, ACZ, KSH, KP, DMG_STAT, DMG_FAT, CP, MP
      DOUBLE PRECISION CF1, CF2, CF3, CF4, CF5, CF6, CF7, Q
      DOUBLE PRECISION RT, RT_OLD, E_I, E_II, E_M, G_C, TAU_MC
      DOUBLE PRECISION LAMBDA, SERR
      COMMON KFLAG
C
      PARAMETER(ZERO=0.D0, ONE=1.D0, TWO=2.D0, THREE=3.D0, TEN=10.D0)
C
      KK          = PROPS(1)
      TN          = PROPS(2)
      TS          = PROPS(3)
      TT          = PROPS(4)
      G1C         = PROPS(5)
      G2C         = PROPS(6)
```

```
52        G3C         = PROPS(7)
53        ETA         = PROPS(8)
54        G1TH        = PROPS(9)
55        RATIO       = PROPS(10)
56        C1          = PROPS(11)
57        M1          = PROPS(12)
58        C2          = PROPS(13)
59        M2          = PROPS(14)
60        CM          = PROPS(15)
61        MM          = PROPS(16)
62        E3          = PROPS(17)
63        DMG_MAX     = PROPS(18)
64        E11         = PROPS(19)
65        E22         = PROPS(20)
66        G12         = PROPS(21)
67        V21         = PROPS(22)
68  c
69        DMG_OLD     = STATEV(1)
70        TAU_OLD     = STATEV(2)
71        DELTA_OLD   = STATEV(3)
72        DELTAG_OLD  = STATEV(4)
73        DDDN_OLD    = STATEV(6)
74  c
75  c ------------------------- STATIC -------------------------
76  c
77        !DISPLACEMENT AT THE END
78        DO I = 1, NTENS
79           DELTAE(I) = STRAN(I) + DSTRAN(I)
80        END DO
81  c
82        !DISPLACEMENT INCREMENTS
83        DELTAN = DELTAE(1)
84        DELTAS = DELTAE(2)
85  c
86        !IF THE ANALYSIS IS IN 2D, DELTAT IS ZERO, IF IT IS 3D, DELTAT IS THE
     THIRD ELEMENT
```

```
87        IF (NTENS.EQ.TWO) THEN
88           DELTAS = ZERO
89        ELSE
90           DELTAT = DELTAE(3)
91        END IF
92  c
93        !EFFECTIVE SEPARATION
94        DELTA_SHEAR = SQRT(DELTAS**2 + DELTAT**2)
95        LAMBDA = SQRT(DELTAN**2 + DELTA_SHEAR**2)
96  c
97        !MIXED-MODE RATIO
98        BETA = DELTA_SHEAR/(MAX(DELTAN,ZERO) + DELTA_SHEAR)
99        KSH = G1C/G2C*(TS/TN)**2*KK
100 c
101       !MIXED-MODE RATIO WITH SHEAR PENALTY STIFFNESS
102       CF6 = KSH*DELTA_SHEAR**2 + KK*MAX(DELTAN,ZERO)**2
103       CF7 = KSH**2*DELTA_SHEAR**2 + KK**2*MAX(DELTAN,ZERO)**2
104       PSI=(KSH*DELTA_SHEAR**2)/CF6
105 c
106       !COEFICCIENT C FOR MIXED-MODE
107       CP=TEN**(LOG10(C1) + PSI*LOG10(CM) + (PSI**2)*LOG10(C2/(CM*C1)))
108 c
109       !COEFFICIENT M  FOR MIXED-MODE
110       MP = M1 + (MM*PSI) + ((M2-M1-MM)*(PSI**2))
111 c
112       !MIXED-MODE PENALTY STIFFNESS
113       KP = KK*(ONE - PSI) + KSH*PSI
114 c
115       !SEPARATION
116       DELTA = CF6/SQRT(CF7)
117 c
118       !PURE MODE ONSET SEPARATION
119       DELTA0_SHEAR = TS/KSH
120       DELTA0_N = TN/KK
121 c
122       !MIXED-MODE ONSET SEPARATION
```

```
      CF4 = (KSH*DELTA0_SHEAR**2 - KK*DELTA0_N**2)*(PSI**ETA)
      DELTA0 = SQRT((KK*DELTA0_N**2 + CF4)/(KP))
c
      !MIXED-MODE FINAL SEPARATION
      DELTAC_SHEAR = TWO*G2C/TS
      DELTAC_N = TWO*G1C/TN
      CF5 = (KSH*DELTA0_SHEAR*DELTAC_SHEAR - KK*DELTA0_N*DELTAC_N)
      DELTAF = (KK*DELTA0_N*DELTAC_N + CF5*(PSI**ETA))/(KP*DELTA0)
c
      !DAMAGE THRESHOLD
      RT_OLD = (DELTA0*DELTAF)/(DELTAF - DMG_OLD*(DELTAF - DELTA0))
      RT = MAX(RT_OLD,DELTA)
      IF(DELTA.GT.RT_OLD) THEN
         DMG_STAT =(DELTAF*(RT - DELTA0))/(RT*(DELTAF - DELTA0))
         DMG_STAT = MIN(DMG_STAT,ONE)
      ELSE
         DMG_STAT = DMG_OLD
      ENDIF
      TAU = DELTA*KP*(ONE - DMG_STAT)
c
      !MODIFICATION FOR MIXED-MODE PARAMETERS
      Q      = SQRT(TWO*(SQRT(E22/E11)-V21) + E22/G12)/TWO
      E_I    = E22/Q
      E_II   = E22/Q*SQRT(E11/E22)
      TAU_MC = SQRT(TN**2 + (TS**2 - TN**2)*(PSI**ETA))
      G_C    = G1C + (G2C - G1C)*(PSI**ETA)
      E_M    = E_I*(ONE - PSI) + E_II*PSI
c
c ------------------------ FATIGUE ------------------------
c
      IF(TIME(2).GT.ONE.AND.DMG_STAT.LT.ONE) THEN
         !CALCULATE DMG WITH OLD DDDN
         DMG_FAT = DDDN_OLD*DTIME
         DMG = DMG_STAT + DMG_FAT
         DMG = MIN(DMG,ONE)
         !COMPUTE NEW DDDN
```

```
159         !SERR
160         IF(DELTA.GT.ZERO) THEN
161            COEFF1 =(DELTAF - (DELTAF - DELTA)**2/(DELTAF - DELTA0))
162            IF(DMG_FAT.EQ.ZERO) THEN
163               G_MAX = DELTA0*KB/TWO*COEFF1
164            ELSE
165               TAU = DELTA*KB*(ONE - DMG)
166               G_MAX = DELTAG_OLD + (TAU + TAU_OLD)*(DELTA - DELTA_OLD)/TWO
167            END IF
168            DELTAG = G_MAX*(ONE - RATIO**2)
169            !CRACK GROWTH RATE
170            IF (DELTAG.GT.ZERO.AND.DELTAG.LT.G_C) THEN
171          IF(KFLAG.EQ.0) THEN
172          DADN = CP*(DELTAG)**MP
173            !AREA OF COHESIVE ZONE
174            ACZ = 0.1D0*(E_M*DELTAG)/((TAU_MC)**2)
175            !DAMAGE VARIABLE AS A FUNCTION OF CYCLES
176            CF2 = DELTAF*DELTA0*ACZ
177            CF3 = ONE - DMG
178            DDDN=DADN*(DELTAF*CF3 + DMG*DELTA0)**2/(CF2)
179            !MAX NUMBER OF CYCLES
180            DELTAN_MAX = DMG_MAX /DDDN
181            !CHECK FOR MAX NUMBER OF CYCLES
182            IF(DTIME.GT.DELTAN_MAX) THEN
183               PNEWDT = 0.8*DELTAN_MAX / DTIME
184            END IF
185            !CHECK G_TH IF ELEMENT HAS JUST FAILED
186            IF((DMG.EQ.ONE).AND.(DMG_OLD.LT.ONE)) THEN
187                IF(DELTAG.LT.G1TH) THEN
188                   KFLAG = 1
189                ELSE
190                   KFLAG = 0
191                END IF
192            END IF
193            ELSE
194               DDDN = ZERO
```

```
195               END IF
196               END IF
197            END IF
198         ELSE
199            DMG = DMG_STAT
200         ENDIF
201   C
202         !FULL STIFFNESS MATRIX
203         DO I = 1, NTENS
204            DO J = 1, NTENS
205               CFULL(I,J)=ZERO
206            END DO
207         END DO
208   C
209         IF (DELTAN.GE.ZERO) THEN
210            CFULL (1,1) = KK*(ONE - DMG)
211         ELSE
212            CFULL (1,1) = KK
213         END IF
214            CFULL (2,2) = KSH*(ONE - DMG)
215         !CFULL (3,3) ONLY EXISTS IN 3D
216         IF (NTENS.EQ.THREE) THEN
217            CFULL (3,3) = KSH*(ONE - DMG)
218         END IF
219   C
220         !STRESS CALCULATION
221         DO I = 1, NTENS
222            STRESS(I)=ZERO
223            DO J = 1, NTENS
224               STRESS(I) = STRESS(I)+ CFULL(I,J)*DELTAE(J)
225            END DO
226         END DO
227   C
228         !TANGENT STIFFNESS MATRIX
229         DO I = 1, NTENS
230            DO J = 1, NTENS
```

```
231               DDSDDE(I,J)=ZERO
232            END DO
233         END DO
234 C
235         IF (DELTA.GT.RT_OLD.AND.DELTA.LT.DELTAF) THEN
236            CF1 = ((DELTAF*DELTA0)/((DELTAF - DELTA0)*DELTA**3))
237            IF (DELTAN.GE.ZERO) THEN
238               DDSDDE(1,1) = CFULL(1,1) - KK*CF1*DELTAN**2
239            ELSE
240               DDSDDE(1,1) = KK
241            END IF
242               DDSDDE(2,2) = CFULL(2,2) - KSH*CF1*DELTAS**2
243               DDSDDE(3,3) = CFULL(3,3) - KSH*CF1*DELTAT**2
244               DDSDDE(1,2) = -KK*CF1*DELTAS*DELTAN
245               DDSDDE(2,1) = -KSH*CF1*DELTAS*DELTAN
246            IF (NTENS.EQ.THREE) THEN
247               DDSDDE(1,3) = -KK*CF1*DELTAT*DELTAN
248               DDSDDE(3,1) = -KSH*CF1*DELTAT*DELTAN
249               DDSDDE(2,3) = -KSH*CF1*DELTAS*DELTAT
250               DDSDDE(3,2) = DDSDDE(2,3)
251            END IF
252         ELSE
253            DDSDDE(1,1) = CFULL(1,1)
254            DDSDDE(2,2) = CFULL(2,2)
255            IF (NTENS.EQ.THREE) THEN
256               DDSDDE(3,3) = CFULL(3,3)
257            END IF
258         END IF
259 C
260         STATEV(1)    = DMG
261         STATEV(2)    = TAU
262         STATEV(3)    = DELTA
263         STATEV(4)    = DELTAG
264         STATEV(5)    = DADN
265         STATEV(6)    = DDDN
266         STATEV(7)    = BETA
```

```
267         STATEV(8)    = PSI
268         STATEV(9)    = ACZ
269         STATEV(10)   = KSH
270   c
271   c ELEMENT DELETION ONLY WORK IF INITIAL DMG IS NOT APPLIED
272   c
273         !ELEMENT DELETION
274         IF (STATEV(1).GE.1) THEN
275            IF (STATEV(11).NE.0) THEN
276               STATEV(11) = 0
277            END IF
278         END IF
279   c
280         RETURN
281         END
```

Bibliography

[1] S. Abrate. Impact on laminated composite materials. *Applied Mechanics Review*, 44: 155–190, 1991.

[2] H. Albertsen, J. Ivens, P. Peters, M. Wevers, and I. Verpoest. Interlaminar fracture toughness of CFRP influenced by fiber surface treatment, part I. experimental results. *Composites Science and Technology*, 54:133–145, 1995.

[3] G. Alfano. On the influence of the shape of the interface law on the application of cohesive-zone models. *Composites Science and Technology*, 66(6):723–730, 2006.

[4] K. Anam, M. Todt, and H. E. Pettermann. Computationally efficient modeling of delamination behavior in laminated composites. 8^{th} *ECCOMAS Thematic Conference on the Mechanical Response of Composites: COMPOSITES 2021*,, Editor: M. Fagerström and G. Catalanotti, Chalmers University of Technology:1–12, 2021.

[5] J. J. Andrew, V. Arumugam, K. Saravanakumar, H. N. Dhakal, and C. Santulli. Compression after impact strength of repaired GFRP composite laminates under repeated impact loading. *Composite Structures*, 133:911–920, 2015.

[6] V. S. Anuse, K. Shankar, R. Velmurugan, and S. K. Ha. Compression-after-impact analysis of carbon fiber reinforced composite laminate with different ply orientation sequences. *International Journal of Impact Engineering*, Journal Pre-proof:104277, 2022.

[7] L. Asp, A. Sjögren, and E. S. Greenhalgh. Delamination growth and thresholds in a carbon/epoxy composite under fatigue loading. *Journal of Composites Technology and Research*, 23 (2):55–68, 2001.

[8] ASTM Standard. D7137/D7137M standard test method for compressive residual strength properties of damaged polymer matrix composite plates. *ASTM International*, pages 1–16, 2012.

[9] ASTM Standard. D7136/D7136M standard test method for measuring the damage resistance of a fiber-reinforced polymer matrix composite to a drop-weight impact event. *ASTM International*, pages 1–16, 2012.

[10] F. Aymerich, F. Dore, and P. Priolo. Simulation of multiple delaminations in impacted cross-ply laminates using a finite element model based on cohesive interface elements. *Composites Science and Technology*, 69:1699–1709, 2009.

[11] H. S. Bae, M. S. Kang, K. S. Woo, I. G. Kim, and K. H. In. Test and analysis of modes I, II, and mixed-mode I/II delamination for carbon/epoxy composite laminates. *International Journal of Aeronautical and Space Sciences*, 20:636–652, 2019.

[12] B. L. V. Bak, C. Sarrado, A. Turon, and J. Costa. Delamination under fatigue loads in composite laminates: A review on the observed phenomenology and computational methods. *Applied Mechanics Reviews*, 66 (6):060803, 2014.

[13] B. L. V. Bak, A. Turon, E. Lindgaard, and E. Lund. A simulation method for high–cycle fatigue–driven delamination using a cohesive zone model. *International Journal for Numerical Methods in Engineering*, 106 (3):163–191, 2016.

[14] E. Barbero, P. Lonetti, and K. Sikkil. Finite element continuum damage modeling of plain weave reinforced composites. *Composites Part B: Engineering*, 37(2-3):137–147, 2006.

[15] G. Barenblatt. The mathematical theory of equilibrium cracks in brittle fracture. *Advances in Applied Mechanics*, 7:55–129, 1962.

[16] L. Bazli and M. Bazli. A review on the mechanical properties of synthetic and natural fiber-reinforced polymer composites and their application in the transportation industry. *Journal of Composites and Compounds*, 3:262 – 274, 2021.

[17] M. L. Benzeggagh and M. Kenane. Measurement of mixed-mode delamination fracture toughness of unidirectional glass/epoxy composites with mixed-mode bending apparatus. *Composite Science and Technology*, 56:439–449, 1968.

[18] N. Blanco, E. K. Gamstedt, L. E. Asp, and J. Costa. Mixed-mode delamination growth in carbon–fibre composite laminates under cyclic loading. *International Journal of Solids and Structures*, 41:4219–4235, 2004.

[19] R. Bogenfeld, J. Kreikemeier, and T. Wille. Review and benchmark study on the analysis of low-velocity impact on composite laminates. *Engineering Failure Analysis*, 86:72–99, 2018.

[20] V. V. Bolotin. Delaminations in composite structures: its origin, buckling, growth and stability. *Composites: Part B*, 27B:129–145, 1996.

[21] V. V. Bolotin. Mechanics of delaminations in laminate composite structures. *Mechanics of Composite Materials*, 37:367–380, 2001.

[22] R. Borg, L. Nilsson, and K. Simonsson. Simulating DCB, ENF and MMB experiments using shell elements and a cohesive zone model. *Composites Science and Technology*, 64:269–278, 2004.

[23] C. Bouvet, S. Rivallant, and J. J. Barrau. Low velocity impact modeling in composite laminates capturing permanent indentation. *Composites Science and Technology*, 72: 1977–1988, 2012.

[24] G. T. Camacho and M. Ortiz. Computational modeling of impact damage in brittle materials. *International Journal of Solids and Structures*, 33:2899–2938, 1996.

[25] P. P. Camanho, C. G. Davila, and M. F. D. Moura. Numerical simulation of mixed-mode progressive delamination in composite materials. *Journal of Composite Materials*, 37:1415–1438, 2003.

[26] W. J. Cantwell and J. Morton. The impact resistance of composite materials — a review. *Composites*, 22(5):347–362, 1991.

[27] L. Carlsson, J. Gillespie, and R. Pipies. On the analysis and design of the end notched flexure (ENF) specimen for mode II testing. *Journal of Composite Materials*, 20:594–604, 1986.

[28] T. Ceglar, M. Schwab, and H. E. Pettermann. DCB and ENF multi-scale simulations. 6^{th} *ECCOMAS Thematic Conference on the Mechanical Response of Composites: COMPOSITES 2017,*, Editor: J. J. C. Remmers and A. Turon, TU Eindhoven:13–23, 2017.

[29] G. R. Cowper. The shear coefficient in timoshenko's beam theory. *Journal of Applied Mechanic*, 33:335 – 340, 1966.

[30] A. S. Crasto and R. Y. Kim. Hygrothermal influence on the free-edge delamination of composites under compressive loading. *Composite Materials: Fatigue and Fracture 6, Philadelphia*, Editor: E. A. Armanios:381–393, 1997.

[31] W. Cui and M. R. Wisnom. A combined stress-based and fracture-mechanics-based model for predicting delamination in composites. *Composites*, 24:467—-474, 1993.

[32] Z. Dang, J. Cao, A. Pagani, and C. Zhang. Fracture toughness determination and mechanism for mode-I interlaminar failure of 3D-printed carbon-kevlar composites. *Composites Communications*, 39:101532, 2023.

[33] *Abaqus Analysis User's Guide*. Dassault Systemes Simulia Corp., Providence, RI, USA, 2020. Release 2020.

[34] B. D. Davidson, H. Hu, and R. A. Schapery. An analytical crack-tip element for layered elastic structures. *Journal of Applied Mechanics*, 62:294–305, 1995.

[35] G. Davies and X. Zhang. Impact damage prediction in carbon composite structures. *International Journal of Impact Engineering*, 16(1):149–170, 1995.

[36] G. A. O. Davies, D. Hitchings, and J. Ankersen. Predicting delamination and debonding in modern aerospace composite structures. *Composites Science and Technology*, 66(6):846–854, 2006.

[37] P. Davies, P. Casari, and L. Carlsson. Influence of fibre volume fraction on mode ii interlaminar fracture toughness of glass/epoxy using the 4enf specimen. *Composites Science Technology*, 65:295–300, 2005.

[38] D. Dugdale. Yielding of steel sheets containing slits. *Journal of the Mechanics and Physics of Solids*, 8:100–104, 1960.

[39] M. L. Falk, A. Needleman, and J. R. Rice. A critical evaluation of cohesive zone models of dynamic fracture. *Journal de Physique IV, Proceedings*, 11:543–550, 2001.

[40] D. Feng and F. Aymerich. Modeling and simulation of damage and failure in large composite components subjected to impact loads. *Composite Structures*, 108:161–171, 2014.

[41] J. Gager and H. E. Pettermann. Numerical homogenization of textile composites based on shell element discretization. *Composites Science and Technology*, 72:806–812, 2012.

[42] J. Gager and H. E. Pettermann. FEM modeling of multilayered textile composites based on shell elements. *Composites Part B: Engineering*, 77:46–51, 2015.

[43] A. C. Garg. Delamination – a damage mode in composite structures. *Engineering Fracture Mechanics*, 29:557–584, 1988.

[44] P. H. Geubelle and J. Baylor. Impact-induced delamination of laminated composites: a 2d simulation. *Composites Part B Engineering*, 29:589–602, 1998.

[45] E. González, P. Maimí, P. Camanho, A. Turon, and J. Mayugo. Simulation of drop-weight impact and compression after impact tests on composite laminates. *Composite Structures*, 94:3364–3378, 2012.

[46] H. Hadavinia and H. Ghasemnejad. Effects of mode-I and mode-II interlaminar fracture toughness on the energy absorption of CFRP twill/weave composite box sections. *Composite Structures*, 89:303–314, 2009.

[47] P. W. Harper and S. R. Hallett. Cohesive zone length in numerical simulations of composite delamination. *Engineering Fracture Mechanics*, 75:4774–4792, 2008.

[48] S. Hashemi, A. Kinloch, and J. Williams. The analysis of interlaminar fracture in uniaxial fibre-polymer composites. *Proceedings of the Royal Society of London*, 427: 173–199, 1990.

[49] Z. Hashin. Failure criteria for unidirectional fiber composites. *Journal of Applied Mechanics*, 47:329–334, 1980.

[50] T. K. Hellen. On the method of the virtual crack closure extension. *International Journal of Numerical Methods in Engineering*, 9:187–207, 1975.

[51] A. Hillerborg, M. Modéer, and P. E. Petersson. Analysis of crack formation and crack growth in concrete by means of fracture mechanics and finite elements. *Cement and Concrete Research*, 6:773–781, 1976.

[52] G. R. Irwin. Encyclopedia of physics. *Fracture*, VI:551–590, 1958.

[53] S. P. Joshi and C. T. Sun. Impact induced fracture in a laminated composite. *Journal of Composite Materials*, 19(1):51–66, 1985.

[54] A. J. Kinloch, Y. Wang, J. G. Williams, and P. Yayla. The use of doubler reinforcement in delamination toughness testing. *Composites Science and Technology*, 47:225–237, 1993.

[55] R. Krueger. Virtual crack closure technique: history, approach, and applications. *Applied Mechanics Reviews*, 57:109–143, 2004.

[56] B. Landry and G. LaPlante. Modeling delamination growth in composites under fatigue loadings of varying amplitudes. *Composites Part B: Engineering*, 43 (2): 533–541, 2012.

[57] B. B. Liao, P. D. Wang, J. Y. Zheng, X. F. Cao, Y. Li, Q. J. Ma, R. Tao, and D. N. Fang. Effect of double impact positions on the low velocity impact behaviors and damage interference mechanism for composite laminates. *Composites Part A: Applied Science and Manufacturing*, 136:105964, 2020.

[58] S. Lin and A. M. Waas. Accelerating computational analyses of low velocity impact and compression after impact of laminated composite materials. *Composite Structures*, 260:113456, 2021.

[59] E. Lindgaard, B. L. V. Bak, J. A. Glud, J. Sjølund, and E. T. Christensen. A user programmed cohesive zone finite element for ansys mechanical. *Engineering Fracture Mechanics*, 180:229–239, 2017.

[60] Z. Ling, G. K. Ling, L. Y. Gang, T. X. Yu, and Z. Q. Weng. Experimental study on the dynamic behaviour of aluminium foam sandwich plates under single and repeated impacts at low temperature. *International Journal of Impact Engineering*, 114:123–132, 2018.

[61] D. Liu and L. E. Malvern. Matrix cracking in impacted glass/epoxy plates. *Journal of Composite Materials*, 21(7):594–609, 1987.

[62] C. S. Lopes, P. P. Camanho, Z. Gürdal, P. Maimí, and E. V. González. Low-velocity impact damage on dispersed stacking sequence laminates. Part II: Numerical simulations. *Composites Science and Technology*, 69(7):937–947, 2009.

[63] K. O. Low, M. Johar, A. N. Sung, M. N. M. Nasir, S. S. R. Koloor, M. Petrů, H. A. Israr, and K. J. Wong. Displacement rate effects on mixed-mode I/II delamination of laminated carbon/epoxy composites. *Polymer Testing*, 108:1–11, 2022.

[64] M. May and S. R. Hallett. A combined model for initiation and propagation of damage under fatigue loading for cohesive interface elements. *Composites Part A: Applied Science and Manufacturing*, 41(12):1787–1796, 2010.

[65] A. Mishra and N. K. Naik. Failure initiation in composite structures under low-velocity impact: Analytical studies. *Composite Structures*, 92:436–444, 2010.

[66] G. B. Murri. Effect of data reduction and fiber-bridging on mode I delamination characterization of unidirectional composites. *NF1676L-12684*, 2011.

[67] A. Needleman. A continuum model for void nucleation by inclusion debonding. *Journal of Applied Mechanics*, 54:525–531, 1987.

[68] R. Olsson. Mass criterion for wave controlled impact response of composite plates. *Composites Part A: Applied Science and Manufacturing*, 31:879–887, 2000.

[69] T. K. O'Brien, W. M. Johnston, and G. J. Toland. Mode II interlaminar fracture toughness and fatigue characterization of a graphite epoxy composite material. *NASA/TM-2010-216838*, 2010.

[70] N. V. Padaki and R. Alagirusamya. Low velocity impact behaviour of textile reinforced composites. *Indian Journal of Fibre and Textile Research*, 33:189–202, 2008.

[71] W. V. Paepegem and J. Degrieck. Fatigue degradation modelling of plain woven glass/epoxy composites. *Composites Part A: Applied Science and Manufacturing*, 32(10):1433–1441, 2001.

[72] N. J. Pagano and G. A. Schoeppner. Delamination of polymer matrix composites: problems and assessment. *Oxford (UK)*, Editor: A. Kelly; D. Zweben, 2000.

[73] A. J. Paris and P. C. Paris. Instantaneous evaluation of j and c. *International Journal of Fracture*, 38:R19–R21, 1988.

[74] P. Paris and F. Erdogan. A critical analysis of crack propagation laws. *Journal of Basic Engineering*, 85(4):528–533, 1963.

[75] I. S. Raju. Calculation of strain energy release rates with higher order and singular elements. *Engineering Fracture Mechanics*, 28:251—274, 1987.

[76] J. R. Reeder. 3D mixed-mode delamination fracture criteria - an experimentalist's perspective. *NASA/TM-2006-048260*, 2013.

[77] J. R. Reeder, K. Demarco, and K. S. Whitley. The use of double reinforcement in delamination toughness testing. *Composites Part A: Applied Science and Manufacturing*, 35:1337–1344, 2004.

[78] J. R. Rice. A path independent integral and the approximate analysis of strain concentration by notches and cracks. *Journal of Applied Mechanics*, 35:379–386, 1968.

[79] M. Richardson and M. Wisheart. Review of low-velocity impact properties of composite materials. *Composites Part A: Applied Science and Manufacturing*, 27(12): 1123–1131, 1996.

[80] P. Robinson and G. A. O. Davies. Impactor mass and specimen geometry effects in low velocity impact of laminated composites. *International Journal of Impact Engineering*, 12(2):189–207, 1992.

[81] E. F. Rybicki and M. F. Kanninen. A finite element calculation of stress intensity factors by a modified crack closure integral. *Engineering Fracture Mechanics*, 9:931—-938, 1997.

[82] M. N. Saleh, H. M. El-Dessouky, M. Saeedifar, S. T. Freitas, R. J. Scaife, and D. Zarouchas. Compression after multiple low velocity impacts of NCF, 2D and 3D woven composites. *Composites Part A: Applied Science and Manufacturing*, 125: 105576, 2019.

[83] A. Sasikumara, D. Triasa, J. Costa, N. Blanco, J. Orr, and P. Linde. Effect of ply thickness and ply level hybridization on the compression after impact strength of thin laminates. *Composites Part A: Applied Science and Manufacturing*, 121:232–243, 2019.

[84] G. A. Schoeppnera and S. Abrate. Delamination threshold loads for low velocity impact on composite laminates. *Composites Part A: Applied Science and Manufacturing*, 31:903–915, 2000.

[85] M. Schwab and H. E. Pettermann. Modeling and simulation of damage and failure in large composite components subjected to impact loads. *Composite Structures*, 158: 208–216, 2016.

[86] M. Schwab, M. Todt, M. Wolfahrt, and H. E. Pettermann. Failure mechanism based modeling of impact on fabric reinforced composite laminates based on shell elements. *Composites Science and Technology*, 128:131–137, 2016.

[87] E. Sevkat, B. Liaw, F. Delale, and B. B. Raju. Drop-weight impact of plain-woven hybrid glass–graphite/toughened epoxy composites. *Composites: Part A*, 40:1090—-1110, 2009.

[88] E. Sevkat, B. Liaw, F. Delale, and B. B. Raju. Effect of repeated impacts on the response of plain-woven hybrid composites. *Composites Part B: Engineering*, 41: 403–413, 2010.

[89] S. Z. H. Shah, S. Karuppanan, P. S. M. Megat-Yusoff, and Z. Sajid. Impact resistance and damage tolerance of fiber reinforced composites: a review. *Composite Structures*, 217:100–121, 2019.

[90] P. O. Sjöblom. On low-velocity impact testing of composite materials. *Journal of Composite Materials*, 22(1):30–52, 1988.

[91] A. Sjögren, A. Krasnikovs, and J. Varna. Experimental determination of elastic properties of impact damage in carbon fibre/epoxy laminates. *Composites Part A: Applied Science and Manufacturing*, 32:1237—-1242, 2001.

[92] E. Smeets. Development of a Fatigue Analysis Tool Using Cohesive Zone Modelling for Composite Specimens. *Master Thesis, TU Delf, Department of Aerospace Structures and Materials, Delf, Netherlands*, 2019.

[93] M. Springer. Nichtlineare Finite Elemente Simulation der Schädigungsmechanismen sowie der Resttragfähigkeit von Schlagbeanspruchten Kohlenstofffaser-Epoxidharz-Verbunden. *Master Thesis, TU Wien, Institute of Lightweight Design and Structural Biomechanics, Vienna, Austria*, 2014.

[94] M. Springer, A. Turon, and H. E. Pettermann. A thermo–mechanical cyclic cohesive zone model for variable amplitude loading and mixed–mode behavior. *International Journal of Solids and Structures*, 159:257–271, 2019.

[95] A. Szekrényes and J. Uj. Over-leg bending test for mixed-mode I/II interlaminar fracture in composite laminates. *International Journal of Damage Mechanics*, 16(1): 5–33, 2007.

[96] T. E. Tay and F. Shen. Analysis of delamination growth in laminated composites with consideration for residual thermal stress effects. *Journal of Composite Materials*, 36: 1299–1320, 2002.

[97] A. Turon, P. P. Camanho, J. Costa, and C. G. Dávila. An interface damage model for the simulation of delamination under variable-mode ratio in composite materials. *NASA/TM-2004-213277*, 2004.

[98] A. Turon, C. G. Dávila, P. P. Camanho, and J. Costa. An engineering solution for using coarse meshes in the simulation of delamination with cohesive zone models. *NASA/TM-2005-213547*, 2005.

[99] A. Turon, P. P. Camanho, J. Costa, and C. G. Dávila. A damage model for the simulation of delamination in advanced composites under variable-mode loading. *Mechanics of Materials*, 38(11):1072–1089, 2006.

[100] A. Turon, J. Costa, P. Camanho, and C. Dávila. Simulation of delamination in composites under high-cycle fatigue. *Composites Part A: Applied Science and Manufacturing*, 38(11):2270–2282, 2007.

[101] A. Turon, C. G. Davila, and P. P. Camanho. An engineering solution for mesh size effects in the simulation of delamination using cohesive zone model. *Engineering Fracture Mechanics*, 74:1665–1682, 2007.

[102] A. Turon, J. Costa, P. P. Camanho, and P. Maimí. Analytical and numerical investigation of the length of the cohesive zone in delaminated composite materials. *Springer Netherlands*, 2008.

[103] A. Turon, P. P. Camanho, J. Costa, and J. Renart. Accurate simulation of delamination growth under mixed-mode loading using cohesive elements: Definition of interlaminar strengths and elastic stiffness. *Composite Structures*, 92:1857–1864, 2010.

[104] A. Turon, E. V. González, C. Sarrado, G. Guillamet, and P. Maimí. Accurate simulation of delamination under mixed-mode loading using a cohesive model with a mode-dependent penalty stiffness. *Composite Structures*, 184:506–511, 2018.

[105] V. Tvergaard and J. W. Hutchinson. The relation between crack growth resistance and fracture process parameters in elastic–plastic solids. *Journal of the Mechanics and Physics of Solids*, 40:1377–1397, 1992.

[106] P. L. Vachon, V. Brailovski, and P. Terriault. Prediction of the propagation of impact-induced delamination in carbon/epoxy laminates. composite structure. *Composite Structures*, 95:227—-235, 2013.

[107] U. K. Vaidya. Impact response of laminated and sandwich composites. in: Abrate, S. (eds). *Impact Engineering of Composite Structures, Part of the CISM International Centre for Mechanical Sciences book series*, 526:97–191, 2011.

[108] G. Wimmer and H. E. Pettermann. A semi-analytical model for the simulation of delamination in laminated composites. *Composite Science and Technology*, 68:2332–2339, 2007.

[109] G. Wimmer, W. Kitzmüller, G. Pinter, T. Wettemann, and H. E. Pettermann. Computational and experimental investigation of delamination in l-shaped laminated composite components. *Engineering Fracture Mechanics*, 76(18):2810–2820, 2009.

[110] D. Zhang, X. Zheng, J. Zhou, and W. Zhang. Bridging the low-velocity impact energy versus impact damage and residual compression strength for composite laminates. *Journal of Reinforced Plastics and Composites*, 40:378–390, 2021.